Exploring the Microphysical and Environmental Controls on Orographic Precipitation in an Atmospheric River Environment

by

Annareli Morales

A dissertation submitted in partial fulfillment
of the requirements for the degree of
Doctor of Philosophy
(Atmospheric, Oceanic, and Space Sciences)
in the University of Michigan
2019

Doctoral Committee:

Professor Allison L. Steiner, Chair
Associate Professor Veronica Berrocal
Associate Professor Mark Flanner
Associate Professor Christiane Jablonowski
Dr. Hugh Morrison, National Center for Atmospheric Research
Dr. Derek J. Posselt, Jet Propulsion Laboratory

Annareli Morales

annareli@umich.edu

ORCID iD: 0000-0001-6863-258X

Dedication

This dissertation is dedicated to my late father, Francisco Morales.
A promise made; a promise kept.

Acknowledgements

The author thanks numerous colleagues for their helpful discussions, suggestions, and assistance throughout this research (in no particular order): George Bryan, Fei He, Ethan Gutmann, Kristen Rasmussen, Rosimar Rios-Berrios, Mimi Hughes, Rich Rotunno, Rebecca Haacker, Dale Durran, Chris Davis, and Marcello Miglietta. The work presented in this dissertation was funded by the University of Michigan Rackham Merit and Predoctoral Fellowships, the Advanced Study Program's Graduate Visitor Program at the National Center for Atmospheric Research (NCAR), and by NASA Interdisciplinary Science Grant NNX14AG68G. Thank you to NCAR and the Mesoscale and Microscale Meteorology lab for hosting me during the last two and a half years of my PhD.

I want to sincerely thank Derek Posselt for his continuous support and mentorship. I honestly could not have made it through my PhD without your kind words, patience, and positivity. I always looked forward to our weekly chats that helped with my various "freak outs". I want to thank Hugh Morrison for teaching me how to approach scientific research, helping me improve my writing, and mentoring me ever since I was a confused undergrad enchanted by the intricacies of microphysics.

Finally, I want to acknowledge my dear friends and family who helped keep me sane and laughing throughout this journey. Thank you all for listening to my tear-filled rants about grad school. Love you all! Ma, gracias por darme vida y por todos tus sacrificios para que pudiéramos tener oportunidades que tu no tuviste. Blake, thanks for embracing my silliness and reminding

me everything is going to be okay; I love you. Figg, thanks for bringing a smile to my face every day; meow meow meow.

Table of Contents

List of Tables

List of Figures

Abstract

Microphysical parameterizations (MPs) approximate the very small-scale behavior associated with cloud and precipitation processes and their feedbacks on the atmosphere, which cannot be directly resolved by numerical weather and climate prediction models. For numerical simplicity, many of the effects induced by ice crystal shape variability and growth processes are approximated through the use of tunable parameters within MPs. These parameter values have an inherent uncertainty due to limited observations and natural variability which is neglected in MPs. It is thus hypothesized that perturbations to these microphysical parameters may be a source of simulated orographic precipitation uncertainty. Phase changes associated with these microphysical processes can alter the thermodynamic profile and the dynamics of the system, resulting in effects on surface precipitation. This dissertation thus aims to explore the sensitivity of mountain-induced/enhanced (*orographic*) precipitation to perturbations in microphysical parameters, in conjunction with changes to upstream environmental conditions.

To test the hypothesis, an idealized modeling framework is applied using the Cloud Model 1 to simulate a moist, nearly neutral environment flowing over a bell-shaped mountain. The upstream environment is associated with a long, narrow corridor of strong water vapor transport found ahead of the cold front of an extra-tropical cyclone called an atmospheric river (AR). The orographic precipitation produced from ARs being forced upward my mountains provides a source of freshwater but can also lead to flooding upwind. Statistically robust methods including the Morris screening method and a Markov chain Monte Carlo algorithm are

applied to understand precipitation sensitivities, as well as to identify which parameter combinations could produce a specific spatial precipitation distribution. Results show that the most influential parameters to orographic precipitation are associated with the fallspeed of snow, collection of supercooled water by ice, collection of cloud droplets by rain, the speed of air flowing towards the mountain, the height of the freezing level, and the relative humidity of the upstream environment. In general, perturbations to microphysical parameters affect the location of peak precipitation, while the total amount of condensate available is more sensitive to environmental parameter perturbations. There is a strong spatial sensitivity to the influential parameters, as changes in freezing level can affect the location of dominant rain processes, i.e., microphysical parameter sensitivities can change for different environments. Although the upstream environment influences the available condensate that microphysical processes can act upon, both processes can result in changes to precipitation of similar magnitudes, especially over the upwind slope of the mountain. Complex relationships between environmental and microphysical parameters are found, demonstrating mitigating factors that can compensate for the effect of perturbing a specific parameter. For example, to yield a similar precipitation intensity and distribution, horizontal wind speed values would need to decrease if the fallspeed of snow is reduced.

The results presented herein highlight the complexity of orographic precipitation sensitivity to microphysics and environmental conditions, suggesting a small subset of parameters are responsible for most of the induced precipitation variability. Evaluation of parameter sensitivity is important for ensemble forecasting and data assimilation, as it is

generally not computationally feasible to perturb every parameter in the full set of physics parameterizations, thus the small subset of parameters found here could be applied. The results from this dissertation may help future field campaigns focus on observing key processes to better constrain parameter uncertainty and improve our understanding of orographic precipitation.

Chapter 1. Introduction

1.1 "Snow in the Mountains, Water in the Fountains"

Orographic precipitation describes precipitation that has been generated or modified through the interaction of moist flow with topography. Over 50% of the global mountain area provides an essential or supportive role for low-land freshwater resources, with some areas bearing "an essential hydropower potential" (Viviroli et al. 2007). Orographic precipitation supplies up to 50% of the total river discharge in humid regions and up to 90% of the total river discharge in arid regions (Viviroli and Weingartner 2004). Figure 1.1 emphasizes the hydrological importance of mountain ranges around the world, such as the Cascade and Sierra Nevada Mountains over the Western U.S., the Southern Andes in South America, and the Himalayas in Asia. At high elevations, accumulated snow stores freshwater during the winter months that then melts in the spring and early summer, feeding rivers, lakes, aquifers, and man-made reservoirs during the dry season (Mote et al. 2005). Over half of the world's population lives and works in regions which "rely heavily on mountain discharge", especially in developing nations (Viviroli et al. 2003). As our planet's climate continues to change from the effects of anthropogenic greenhouse gas emissions, water supplies may become limited as we struggle to provide for the growing global population, leading to local and national conflicts for water rights (Viviroli and Weingartner 2002). Additionally, heavy precipitation over mountains can trigger flooding, landslides, and avalanches that can lead to costly damage to local infrastructure and cause loss of life and property (Maddox et al. 1978; Caine 1980; Conway and Raymond 1993; Ralph et al. 2006; Neiman et al. 2008b; Leung and Quian 2009; Ralph et al. 2011; Gochis et al.

2015; White et al. 2019). Given the societal impacts, it is important we understand the processes that control orographic precipitation and improve their representation in numerical weather and climate prediction models. Local water resource and emergency managers and other stakeholders (e.g., recreation, tourism, agricultural, and energy industries) need to know the location, amount, and type of precipitation that will fall over their mountain regions, e.g., if most of the precipitation falls as rain on previously formed snowpack it can promote early snowmelt (Kim et al. 2013) and induce flooding downstream (White et al. 2019). Better quantification of forecast precipitation uncertainty will benefit hazard and water management and help us understand how these processes will be affected by a warming climate.

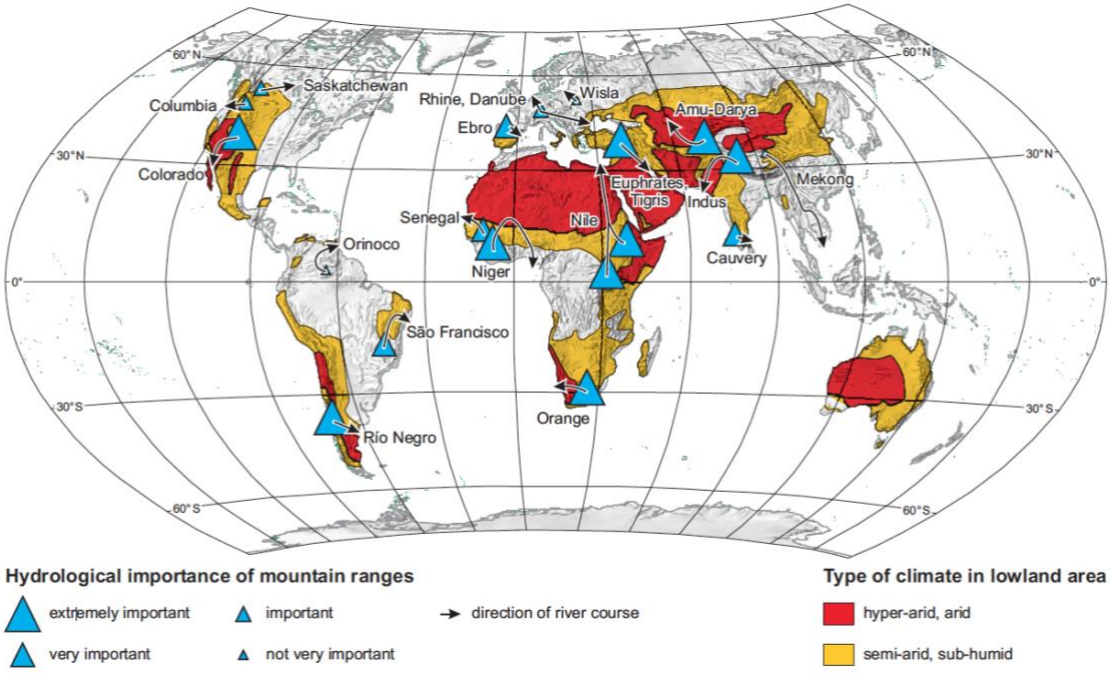

Figure 1.1 Hydrologic importance of mountain ranges worldwide (Fig. 4 from Viviroli and Weingartner 2004).

1.2 Physical Mechanisms Controlling Orographic Precipitation

Common terms used when discussing the location of precipitation over a mountain are *upwind* and *downwind*. Upwind describes the region of the mountain opposing the prevailing wind direction, while downwind is the region in the same direction as the prevailing wind direction (Figure 1.2). Typically, these two regions are located on either side of the maximum mountain height H_{mtn}. The slope of the terrain is calculated by the ratio of H_{mtn} and the mountain half-width A_{mtn}, which represents the width of the mountain where the elevation is 50% of H_{mtn}.

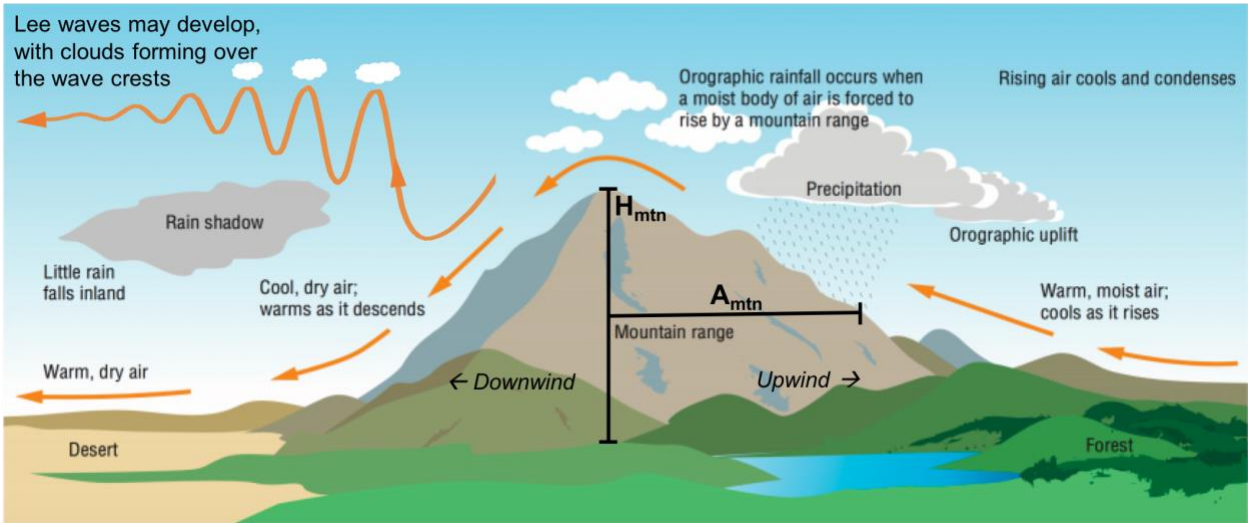

Figure 1.2 Orographic precipitation schematic adapted from Moran (2018). Annotations were added to include the possibility of lee waves, and illustrating other terms used within the text.

The physical mechanisms responsible for precipitation over mountains occur over different spatial scales. The air masses (e.g., continental polar) and large-scale storm systems (e.g., extra-tropical cyclones) that move over major mountain chains extend on the order of 1000 km, while the processes developing cloud droplets and hydrometeors (precipitating liquid or frozen water) and their interactions occur at the μm to mm scale. In general, mountains influence

precipitation through the vertical displacement (rising or descending motions) of air, which can be mechanically-forced as air is forced to rise over the upwind slope, or thermally-forced as the mountain slopes are diurnally-heated causing buoyant thermals (Houze 2012). Rising air will adiabatically expand and cool as the ambient pressure decreases with height (Wallace and Hobbs 2006). If the rising air parcel contains sufficient amounts of water vapor and experiences sufficient cooling with height, saturation can be achieved and phase changes between vapor and liquid or ice can occur (Wallace and Hobbs 2006; Figure 1.2). Once a cloud forms, ice crystals and cloud droplets can grow through various microphysical processes and with time grow large enough to overcome the updraft and fall out of the cloud (Figure 1.4). Depending on the particle size and conditions below cloud, hydrometeors may reach the surface. Descending air on the lee side of the mountain will warm adiabatically and become drier, leading to sub-saturated conditions that cause cloud water and rain evaporation (Figure 1.2). Downslope windstorms, trapped lee waves, vertically-propagating waves, and other turbulent flows (e.g., rotors, hydraulic jumps) can develop as the flow descends over the downwind slope (Durran 1990). These flows may result in cloud formations over lee waves, e.g., lenticular or cap clouds, or stratiform clouds that may transition to buoyantly-driven circulations and grow upscale into thunderstorms (Houze 2012). Over a long period of time, these general rising and descending flows can result in forests and a wetter climate upwind and a dry, desert climate over the "rain shadow" region on the lee side of the mountain (Figure 1.2).

Although mountains can generate lift that can result in precipitating clouds, mountains can also modify or enhance precipitation as pre-existing storm systems (e.g. extra-tropical

cyclones and hurricanes) travel over mountainous regions (Houze 2012). The "seeder-feeder" mechanism can result in enhanced precipitation as a pre-existing precipitating "seeder" cloud associated with the large-scale system moves over an orographically-generated low-level "feeder" cloud (Bergeron 1965; Robichaud and Austin 1988; Purdy et al. 2005). The precipitation produced by the seeder cloud falls through the feeder cloud and the hydrometeors can continue to grow as they collect cloud water traveling through the feeder cloud, resulting in enhanced precipitation rates over the upwind mountain slope (Houze 2012). The research presented in this dissertation focuses on orographic precipitation generated by mechanically-forced flow and producing peak precipitation rates over the upwind slope and/or mountain top.

Orographic precipitation can be characterized by a linear model developed by Smith (1979, 2006):

$$S(x,y) = \rho q_v \vec{U} \cdot \nabla H_{mtn}(x,y) \quad (1.1)$$

The rate at which condensed water is generated by ascent S is described by the air density ρ and specific humidity q_v at the Earth's surface and the vector product of the horizontal wind $\vec{U}$ (x and y-directions) and the terrain slope ∇H_{mtn}, assuming the air is saturated and moist neutral, and vertical velocities are independent of height (Smith 2006). This basic model illustrates the major environmental factors to upslope precipitation: horizontal wind speed (and direction), mountain slope (height and width), and moisture content. However, this model does not include the non-linear processes associated with the complex flow dynamics that can develop for different stability profiles and mountain shapes, and relationships between microphysical processes and

dynamics-thermodynamics, all resulting in a less than straight-forward characterization of orographic precipitation amount, location, and type.

1.2.1 Prevailing Wind Direction

Observed global precipitation patterns can be broadly explained by observing the prevailing wind direction relative to the mountain slopes, i.e., a wetter climate tends to exist on the upwind side of a mountain, while a drier climate exists within the "rain shadow" on the lee or downwind side of the mountain (Figure 1.2). For example, the Andes Mountains extend across seven countries near the western coast of South America with an average elevation of over 3.5 km (**Error! Reference source not found.**a). In subtropical South America (~20°S-30°S), the prevailing winds are from the east-northeast as the trade winds move over the Amazon rainforest and transport moist, warm air towards the Andes. This results in higher precipitation rates over northern Argentina on the eastern slopes and significantly less precipitation over the western slopes, which is where the Atacama Desert of northern Chile exists (**Error! Reference source not found.**b). Moving poleward along the Andes, the prevailing winds shift to westerlies, where extra-tropical storm systems make landfall on the western slopes in southern Chile leading to increased precipitation (Viale et al. 2018; **Error! Reference source not found.**b). The winter cyclones that make landfall over the Western Coast of the US can interact with coastal mountains and larger mountain chains, e.g., the Sierra Nevadas and Cascade Mountains, leading to enhanced rainfall upwind and significant snowfall over the mountain peaks (Pandey et al. 1999; Dettinger et al. 2004; Roe 2005; Minder et al. 2008; Lundquist et al. 2010). Within the

intermountain west, the Great Basin sits in the "rain shadow" of the Sierras where less precipitation falls (Daly et al. 2008) and the climate is arid.

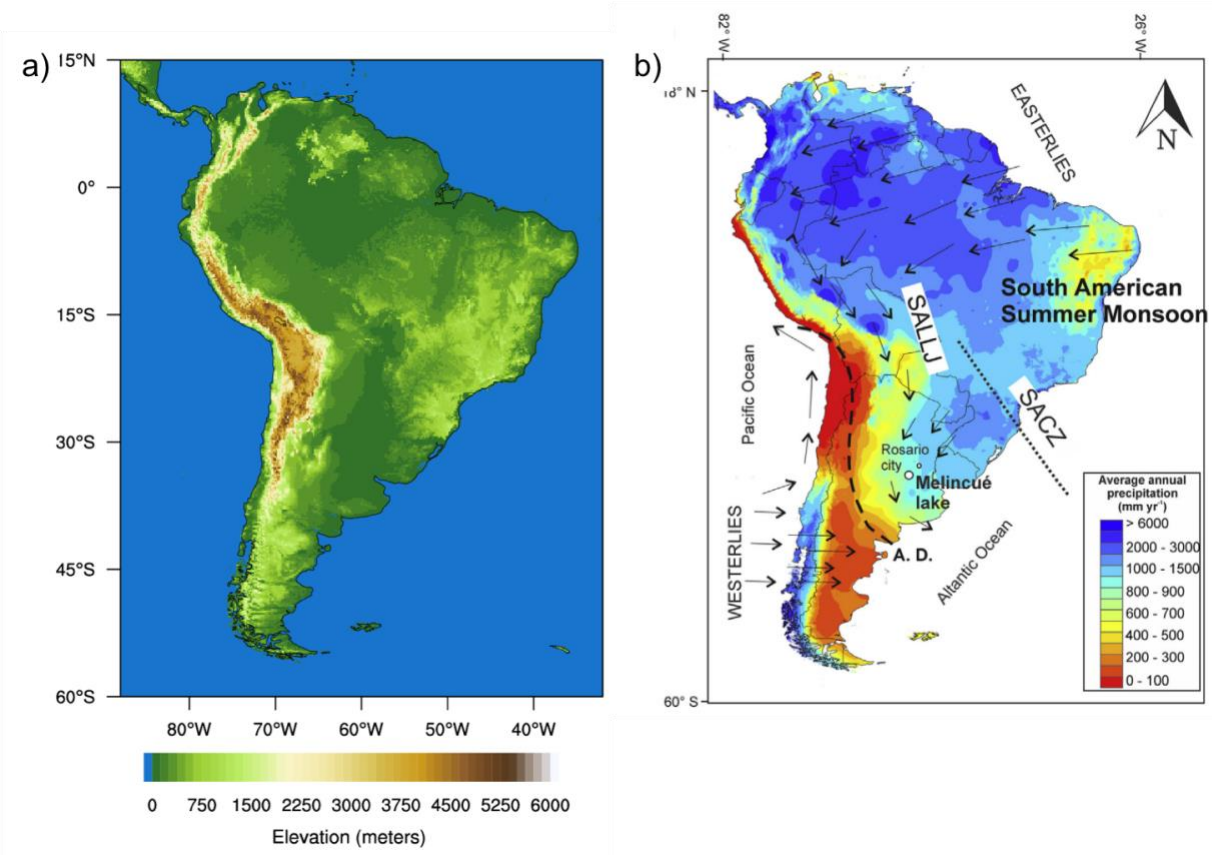

Figure 1.3 South American (a) topographical map, and (b) average annual precipitation with prevailing wind direction illustrated with black arrows (Figure 2a from Guerra et al. 2016).

This large-scale pattern has also been observed over the Himalayan Mountains (Lang and Barros 2004; Anders et al. 2006) and the New Zealand Alps (Wratt et al. 2000). Conversely, the European Alps experience air flow and storms coming from varying directions and thus do not exhibit a clear rain shadow effect (Frei and Schär, 1998). The general circulation patterns of the atmosphere, semi-permanent circulations (e.g., the North and South Pacific High), seasonal mid-latitude cyclones, and mesoscale wind patterns are all important to consider when determining if

moist air will be forced to rise by a mountain and result in cloud development, and possible precipitation.

1.2.2 Atmospheric Flow Dynamics

Broadly speaking, atmospheric flow that encounters a mountain can either flow over the mountain ridge, flow around the topography, or be blocked by the mountain, leading to deflection parallel to the mountain ridge or flow reversal (Houze 2012). To determine how the flow will respond to a mountain barrier, it is important to know the characteristics of the air mass moving over the mountain: horizontal wind speed, stability, low-level temperature, and water vapor content (Sawyer 1956; Smith 1979; Roe 2005; Smith 2006; Houze 2012). These environmental characteristics, in conjunction with the mountain geometry (height, slope, orientation with respect to the flow, terrain-features) can influence the resulting flow and location of precipitation maxima (Houze 2012). For example, a wide mountain (half-width $\geq$30 km) will provide more time for snow growth aloft compared to a narrower barrier (Colle and Zeng 2004b).

In general, buoyancy depends on the relative density of air forced upward compared to the density of the environmental air. Vertical (positive) acceleration occurs because the lifted air is less dense; in this case, temperature serves as a measure of density since it is assumed that pressure equalizes quickly between lifted air and the environment. Depending on the buoyancy or stability of the air, the flow can respond differently to encountering a mountain barrier. Depending on the stability of the air encountering a mountain, the flow can respond differently to the mountain barrier.

The stability of dry (unsaturated) air is quantified by the Brunt-Väisälä frequency N^2, which compares the actual rate of change of temperature with height of the environment (γ) to that of the theoretical dry adiabatic lapse rate (Γ_d):

$$N^2 = \frac{g}{T}(\gamma - \Gamma_d) \tag{1.2}$$

An unsaturated air parcel is considered stable for $N^2 > 0$, i.e., if a parcel is vertically-displaced by the mountain the upward motion will be countered by gravity (g) and the parcel will oscillate about some equilibrium level with frequency N. These waves can vertically propagate away from the mountain, become trapped in the low-levels and decay with height, lead to wave-breaking and rotors that generate turbulence, or generate severe downslope winds (Smith 1979; Durran 1990). If the vertical velocities associated with the lee gravity waves are substantial enough, condensation can occur and clouds can form far downwind, e.g., lenticular clouds. For $N^2 = 0$, the air parcel is said to have neutral stability, i.e., an air parcel has similar density as the ambient environment and no net force is applied on the parcel. This neutral flow will exert no resistance to vertical displacement by the mountain and will follow the terrain when forced to rise. In the case of $N^2 < 0$, any vertical displacement will lead to a vertical acceleration of the parcel. This case would result in dry convection, or vertical mixing: warm air parcels will rise from the unstable layer and cold air will sink from the stable layer above.

Equation 1.2 neglects the effects of moisture on the lapse rates, i.e., condensation releases latent heat, which can decrease the rate of cooling as a saturated parcel is forced to rise. The magnitude of the moist adiabatic lapse rate Γ_m is thus less than the dry adiabatic lapse rate. This results in conditional instabilities, where an air parcel is stable when dry and unstable when

saturated. For saturated air, the moist adiabatic lapse rate must be applied as well as the moist Brunt-Väisälä frequency N_m^2, described in the following equation from Durran and Klemp (1982):

$$N_m^2 = \frac{g}{T}\left(\frac{dT}{dz} + \Gamma_m\right)\left(1 + \frac{Lq_s}{RT}\right) - \frac{g}{1+q_w}\frac{dq_w}{dz}, \quad (1.3)$$

where q_w is the total water mixing ratio (sum of the saturation mixing ratio q_s and the liquid water mixing ratio), L is the latent heat of vaporization, and R is the ideal gas constant for dry air. This dissertation focuses on moist, nearly neutral flow, i.e., flow that is saturated and the moist Brunt-Vaisala frequency N_m^2 is approximately zero for the troposphere, as this type of flow commonly leads to heavy orographic precipitation during non-convective events (Miglietta and Rotunno 2005; Houze 2012). For example, a moist, nearly neutral event during the Olympic Mountains Experiment (OLYMPEX; Houze et al. 2017) produced precipitation rates on the order of 10 mm hr^{-1} and accumulated 24-hour precipitation of over 300 mm upwind of the mountain top (Zagrodnik et al. 2018).

For stable and neutral flow, the non-dimensional mountain Froude number Fr_m (Pierrehumbert and Wyman 1985; Lin and Wang 1996; Markowski and Richardson 2010) is commonly used to determine if flow will be blocked or unblocked when encountering a mountain of height (H_{mtn}) and mean horizontal wind speed ($\bar{U}$):

$$Fr_m = \frac{\bar{U}}{NH_{mtn}} \quad (1.4)$$

Fr_m compares the kinetic energy of the flow impinging on the barrier to the potential energy needed to overcome the barrier. An analogy used to determine blocking is that of a ball being

bowled towards a bell-shaped obstacle, where the weight of the ball represents N (or N_m), the height of the obstacle represents H_{mtn}, and the speed at which the ball is bowled is $\overline{U}$. To get the ball over the obstacle, a heavy ball would need to be moving very fast (higher wind speeds), the weight of the ball would need to be reduced (decreased static stability), or the height of the obstacle would need to be lowered. Similarly, if the mountain is too tall or the cross-barrier winds are too weak, stable flow can become stagnant behind the barrier. For an isolated barrier (e.g., Olympic Mountains) the blocked air will have to go around the barrier, which can induce convergence and cloud development on the lee (Roe 2005; Houze 2012). For a relatively long mountain ridge (e.g., the Himalayan Mountains), the blocked flow can be deflected parallel to the mountain ridge leading to "damming" and the formation of a barrier jet (Neiman et al. 2013), which can affect the spatial distribution of precipitation since ascent can occur farther upwind from the mountain crest over the stable air (Grossman and Durran 1984; Peterson et al. 1991; Roe 2005; Houze 2012).

The vertical velocity (w) that is induced for unblocked flow rising over the upwind slope of the mountain is proportional to the mean horizontal wind speed ($\overline{U}$) and the mountain slope (Smith 1979):

$$w \propto \overline{U} \frac{\Delta H_{mtn}}{\Delta x} \tag{1.5}$$

For a constant slope, this means that an increase in $\overline{U}$ will result in faster vertical velocities, which will directly affect condensation rates (Roe 2005). Observations have shown that near-surface wind speeds can be a good predictor for rain rates when the flow is unblocked (Neiman et al. 2002). A study performed by Tushaus et al. (2015) found that orographic precipitation

upwind decreases non-linearly with increasing half-width for a constant height due to a change in the upwind slope, i.e., as the half-width is increased forced ascent occurs over a wider region, but eventually the slope becomes shallow resulting in smaller vertical motion and weaker precipitation rates. Although mountain height and width can cause differences in precipitation amount and spatial distribution, this dissertation focuses on environmental and microphysical effects as we assume that the mountain geometry will remain constant during a given precipitation event. This specification implicitly assumes that the flow traveling towards the mountain barrier does not shift meridionally along the mountain ridge. For the studies presented in the following chapters, we focus on mountains that can be described as long two-dimensional ridges, such as the Sierra Nevada Mountains of California, as these types can be modeled using a two-dimensional model framework which is less computationally expensive given the number of simulations needed for some of the methods used.

1.2.3 Cloud and Precipitation Processes

Within a cloud, various microphysical processes can occur that determine the evolution of liquid or frozen water particles. The complex relationships between each of these factors existing at different spatial-temporal scales, can influence the precipitation location, amount, and type, making for quite the challenge for forecasters. The following section briefly describes the various pathways by which cloud water and ice crystals can grow and become large enough to precipitate. Warm-rain processes involve liquid-only particles within warm regions of the cloud (temperatures > 0°C), and mixed-phase and ice processes occur at temperatures below 0°C

(Figure 1.2; Rogers and Yau 1989). Mixed-phase processes include both liquid and ice particles, which can coexist in cloud regions with temperatures as low as -40°C (Rogers and Yau 1989).

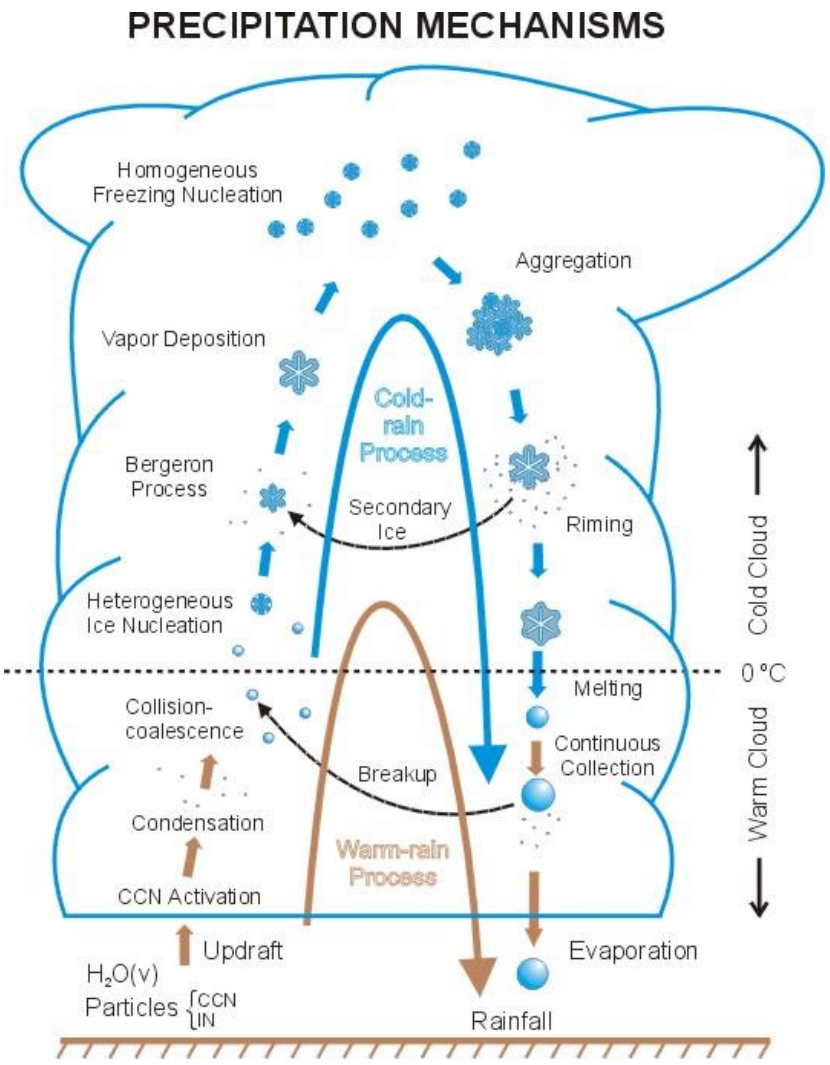

Figure 1.4 Schematic showing possible precipitation mechanisms within a mixed-phase cloud, i.e., liquid, supercooled liquid, and ice particles exist within the cloud. Source: Steve Platnick, NASA.

1.2.3.1 Warm-Rain Processes

As previously described, orographic lifting of a moist parcel of air can lead to condensation on the upwind side of the mountain. The initial condensation involves the activation of cloud condensation nuclei (CCN), which are typically water-soluble aerosols such as sea salt or ammonium sulfate (Rogers and Yao 1989; Pruppacher and Klett 2010). These CCN act as a nucleus for the water vapor to condense on and continue to grow through condensation into a cloud droplet within the updraft region (Rogers and Yao 1989; Pruppacher and Klett 2010). As the cloud evolves, larger cloud drops can develop that will fall faster compared to the smaller cloud droplets. As a result of the differential terminal velocities, these larger drops can collect smaller cloud droplets as they fall through the warm cloud region, growing large enough to overcome the updraft speeds and exit the cloud (Figure 1.4). This process is called collision-coalescence and is one of the primary ways by which rain drops can grow large enough to precipitate within a typical cloud lifetime (Rogers and Yao 1989; Pruppacher and Klett 2010). Once the rain drops exit the cloud, they may experience evaporation if the air below cloud is sub-saturated. Rain (and cloud) evaporation can increase relative humidity values below the cloud base, which can be advected elsewhere or provide additional moisture to a neighboring updraft.

1.2.3.2 Ice and Mixed-Phase Processes

Ice crystals can nucleate through homogeneous freezing at temperatures below -40°C or through heterogeneous freezing, i.e., an insoluble aerosol acts as an ice nucleus where water can deposit (Rogers and Yao 1989; Pruppacher and Klett 2010). The nucleated ice crystals can

continue to grow through vapor deposition in cloud regions where conditions are supersaturated with respect to ice ($RH_{ice} > 100\%$). Because the equilibrium vapor pressure of ice is less than that for water at the same subfreezing temperature, mixed-phase cloud regions where both liquid and ice particles exist can experience the Wegener-Bergeron-Findeisen process (Wegener 1911; Bergeron 1935; Findeisen 1938). During this process ice crystals grow through deposition at the expense of supercooled cloud water droplets (Figure 1.4), i.e., ambient conditions are sub-saturated with respect to liquid water but supersaturated with respect to ice, thus cloud droplets evaporate and ice crystals grow quickly through deposition (Rogers and Yao 1989; Pruppacher and Klett 2010). Various crystal shapes can form, such as dendrites, needles, plates, and columns, depending on the amount of moisture available and the ambient temperature (Rogers and Yao 1989; Pruppacher and Klett 2010). Ice crystals can collide with each other within the cloud and, if the temperatures are appropriate, the ice crystals can stick together and form snowflakes (Rogers and Yao 1989; Pruppacher and Klett 2010). If the temperatures below the cloud are cold enough or if the freezing level intersects the mountain side, these snowflakes can reach the surface below the cloud or be advected leeward if the horizontal winds can transport the snow particles over the mountain top before they reach the surface. If temperatures above freezing exist below cloud base, the snow can melt and reach the surface as rain. Within the cloud a snowflake may become large enough to precipitate, but melt within the warm cloud region (i.e., temperatures are above freezing) and serve as a rain drop that can grow through continuous collection of cloud droplets (Figure 1.4). This process can lead to enhanced precipitation rates over the mountain and is associated with the seeder-feeder mechanism by

which a synoptically-forced upper-level cloud precipitates over an orographically-forced low-level cloud to enhance precipitation over a mountain (Bergeron 1965; Robichaud and Austin 1988; Purdy et al. 2005).

Ice crystals within the mixed-phase region can also grow through the collection of supercooled cloud droplets that then freeze on contact, also known as riming (Rogers and Yao 1989; Pruppacher and Klett 2010). When an ice crystal experiences continuous riming to the point where its initial crystal shape is no longer distinguishable, the hydrometeor is called graupel. Graupel can melt within the warm regions of the cloud and may be able to reach the surface depending on its diameter. Graupel can be transported vertically within an updraft and experience frequent freezing-melting episodes, resulting in a multi-layered frozen hydrometeor termed hail (Rogers and Yao 1989; Pruppacher and Klett 2010). Hail more commonly forms in deep convective storms whose updrafts can be fast enough to suspend any rimed ice long enough to grow into hail (diameter > 5 mm, American Meteorological Society 2012).

1.2.3.3 Microphysical and Environmental Interactions

As hydrometeors change phase, they can release latent heat via freezing or condensation, and require latent heat via melting or evaporation. These phase and associated energy changes can affect the temperature profile and stability within those regions. For example, freezing processes can result in stronger updrafts as the clouds become more buoyant from latent heat release. On the other hand, the melting of snow can result in cooling upwind, which is theorized to be a cause for the vertical displacement of the freezing level towards the mountain side (Minder et al. 2011). Hobbs et al. (1973) demonstrated that the degree of riming of ice particles

influences where they will precipitate over a mountain, e.g., heavily rimed particles fall out faster and land on the upwind slope. The seminal study by Colle (2004) tested various mountain heights and half-widths and found the precipitation responses to mountain height and width depend on the horizontal wind speeds and location of the freezing level upwind. Horizontal wind speed can influence vertical velocities and condensation rates upwind (Roe 2005), affect mountain wave development downwind (Kunz and Wasserman 2011; Tushaus et al. 2015), and transport precipitation horizontally (Colle 2004; Kunz and Kottmeier 2006; Mott et al. 2014; Wang et al. 2017).

Although moisture content is important for the initial formation of clouds upwind, relative humidity values below the cloud can also impact the amount of precipitation that reaches the surface. This is especially true downwind, where descending dry air can evaporate cloud water and rain or sublimate ice crystals. Snow advected to the lee can melt due to the warmer temperatures and result in rain, which may be large enough to resist complete evaporation. Temperature can also affect the amount of moisture that is available, as a colder environment will have less precipitable water available compared to a warmer environment. If the temperature is low, the freezing level (height of 0°C isotherm) may be low enough to exist below the maximum terrain height and affect the spatial distribution of precipitation, i.e., more snow above the freezing level and rain production shifted far upstream. Changes to the freezing level can influence the dominant microphysical processes and the resulting precipitation type reaching the surface.

1.3 “Rivers in the Sky”

An atmospheric river (AR) is defined as “a long, narrow, and transient corridor of strong horizontal water vapor transport that is typically associated with a low-level jet stream ahead of the cold front of an extratropical cyclone” (Ralph et al. 2018; Figure 1.5a). ARs are the largest "rivers" of freshwater on Earth, transporting on average more than double the flow of the Amazon River poleward (American Meteorological Society 2019). Moist neutral flow is a typical characteristic of ARs (Ralph et al. 2004, 2005), and thus when ARs make landfall over mountainous regions they frequently lead to heavy precipitation production (Ralph and Dettinger 2012). ARs can contribute to flooding and damage to infrastructure (e.g., Ralph et al. 2006; White et al. 2019), while producing a large percentage of the annual precipitation in mountain regions such as the Sierra Nevadas (Dettinger et al. 2011) and the southern Andes (Viale et al. 2018).

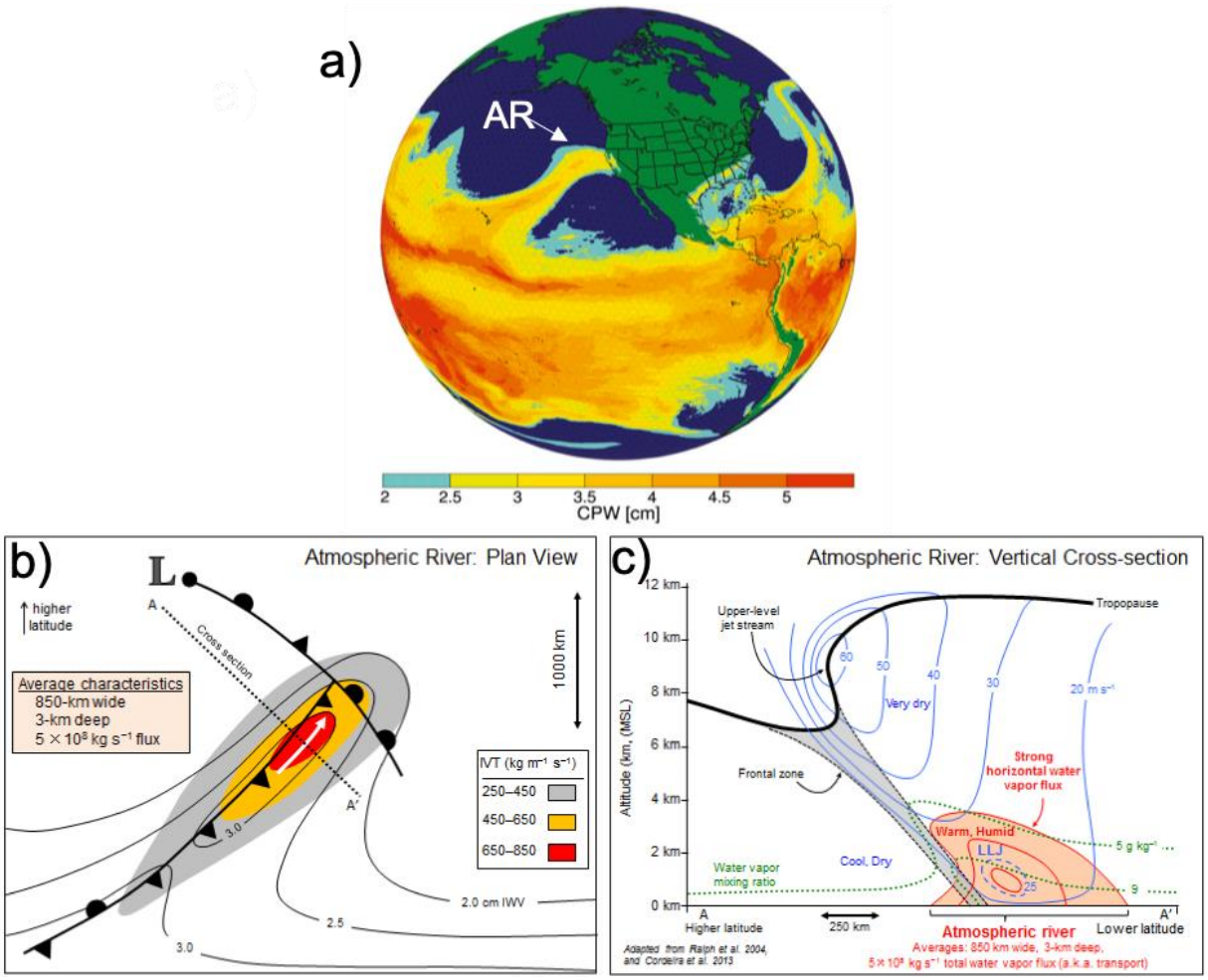

Figure 1.5 Atmospheric river (AR) schematics: (a) column-integrated precipitable water (CPW; cm) showing a typical atmospheric river event from Hagos et al. (2015), and (b) a plan view and (c) vertical-cross section across from Ralph et al. (2017).

More than 90% of the poleward transport of water vapor over the midlatitudes occurs within ARs, which cover less than 10% of the global circumference (Zhu and Newell 1998). ARs are most frequent during the winter months of each hemisphere (Guan and Waliser 2015; Viale et al. 2018), although some can occur during the summer but are not as intense as the winter ARs (Neiman et al. 2008; Kamae et al. 2017). Figure 1.6 shows that ARs frequently make landfall

over Great Britain (Stohl et al. 2008; Lavers et al. 2013), Greenland (Neff 2018; Mattingly et al. 2018), South America (Viale and Nuñez 2011), the Antarctic Peninsula (Gorodetskaya et al. 2014), British Columbia (Curry et al. 2019), and the Pacific Northwest and West Coast of the US (Neiman et al. 2011; Guan and Waliser 2015). An "AR event" is defined by the period of time when integrated water vapor transport (IVT) values are greater than or equal to 250 kg m^{-1} s^{-1}, or precipitable water values greater than 2 mm, are observed continuously over a specific location (Ralph et al. 2018). IVT is calculated by vertically-integrating the product of the horizontal wind speed (m s^{-1}) and specific humidity (kg kg^{-1}) from 1000 hPa to a pressure level between 500 hPa and 200 hPa (varies depending on approach), and dividing by the gravitational acceleration (m s^{-2}), resulting in IVT units of kg m^{-1} s^{-1} (Ralph et al. 2017). Over the U.S. West Coast, AR event duration can vary from 18-25 hours on average depending on the latitude (Rutz et al. 2014), and it is not uncommon to have consecutive ARs make landfall over the same region (e.g., White et al. 2019). The strength of an AR is determined by the IVT values, where IVT ≥ 250 kg m^{-1} s^{-1} (precipitable water ≥ 2 cm) constitute a weak AR and IVT ≥1000 kg m^{-1} s^{-1} (precipitable water ≥ 3.5 cm) constitute strong AR events (Ralph et al. 2019). General environmental characteristics of ARs that make landfall over the U.S. West Coast are warm, moist air from low-levels to the mid-troposphere, moist neutral or stable flow, and a low-level jet (wind speeds > 20 m s^{-1}) (Ralph et al. 2004, 2005; Neiman et al. 2008b; Figure 1.5c). On average, an AR is 850 km wide (rarely exceeding a width of 1000 km), 3 km deep, and over 2000 km in length (Rutz et al. 2004; Guan and Waliser 2015; Ralph et al. 2017; Figure 1.5b,c).

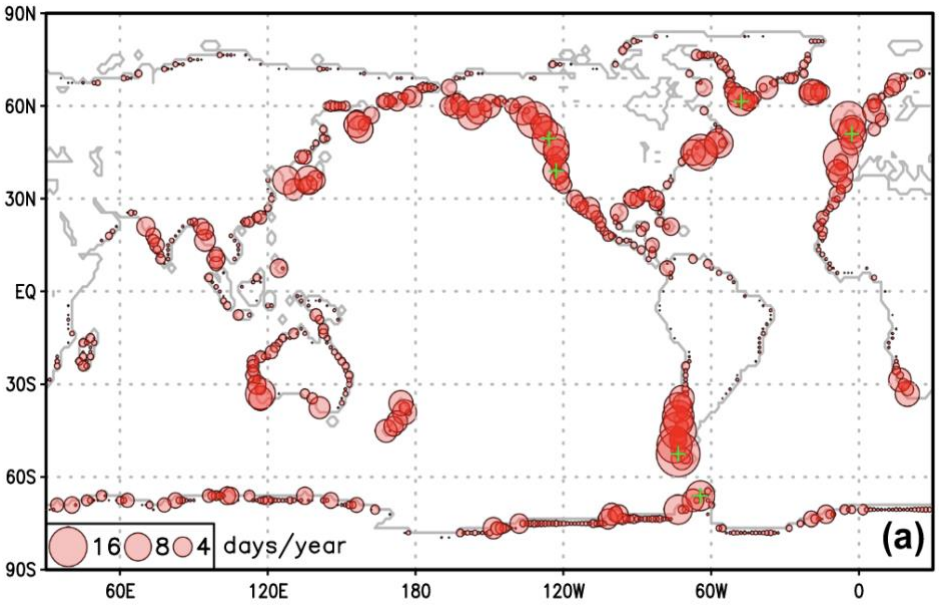

Figure 1.6 Frequency of atmospheric river landfalls worldwide from Guan and Waliser (2015).

1.4 Numerical Modeling and Microphysical Parameterizations

To summarize up to this point, this dissertation focuses on upwind precipitation caused by an atmospheric river interacting with a mountain. The socio-economic impacts of orographic precipitation from ARs emphasize the need for research on precipitation uncertainty within numerical weather prediction (NWP) and climate models. Although many sources of precipitation uncertainty exist within research and operational NWP models, e.g., horizontal grid spacing, (Morrison et al. 2015), boundary layer and radiation schemes (Jankov et al. 2017), the research presented here focuses on microphysics as these processes are closely tied to precipitation in models. Additionally, microphysics plays an important role to other processes in

weather and climate models, such as radiative transfer, cloud-aerosol interactions, and surface process.

NWP models contain grid points spatially separated by 100s of meters to 10s of kilometers, while the formation and interaction of liquid and ice particles happens on the scale of microns to meters. Microphysical parameterizations (MPs) address this scale gap by approximating the very small-scale behavior associated with the development of clouds and precipitation and their feedbacks on the atmosphere, which cannot be resolved directly by the model. Previous modeling studies have shown the choice of MP can affect the forecasted precipitation and storm evolution (Gilmore et al. 2004b; Jankov et al. 2009). Additionally, the choice of microphysics scheme can affect the vertical distribution of hydrometeors and their phase changes, thus affecting the vertical distribution of latent heat release which can have major influences on the dynamics and thermodynamics of a storm system (Gilmore et al. 2004a; Morales et al. 2015).

Two of the most common types of MPs are *bulk* and *bin* schemes. Bulk schemes typically represent the hydrometeors and suspended particles with particle size distributions that follow a functional form, such as gamma, log-normal, or inverse-exponential (Stensrud 2007). Bin schemes divide particles into a finite number of size categories and calculate the evolution of each bin (Stensrud 2007). Although bin schemes tend to be more realistic in their representation of particle sizes (i.e., better representation of particle fall speeds), they are very computationally expensive, especially for operational weather prediction (Stensrud 2007). Bulk schemes are thus often used operationally and for research purposes. Bulk schemes can also predict different

number of "moments" or bulk quantities for different species (x) such as cloud ice, cloud water, snow, rain, graupel, hail. Schemes can predict the mass mixing ratio q_x (1-moment), the number concentration N_x (2-moment), and simulated radar reflectivity Z (3-moment) (Stensrud 2007). For the purposes of this dissertation, a two-moment bulk scheme is sufficient to explore our science questions.

The microphysics parameterization used in this dissertation is the Morrison two-moment scheme (Morrison et al. 2005, 2009). It is a bulk scheme, meaning it represents the initial particle size distribution with a specified functional distribution (i.e., gamma distribution). The scheme predicts the mixing ratio and the number concentration for the following species or categories: cloud ice, cloud water, snow, rain, and rimed ice. The cloud ice species represents smaller ice crystals, regardless of the formation mechanism, and is converted to the snow species based on the deposition growth rate of particles at a specified diameter. In this scheme, the conversion of cloud ice to snow from aggregation of cloud ice is neglected, while aggregation of cloud ice by existing snow and aggregation via self-collection of snow is included. The rimed ice species in the Morrison scheme can be chosen as either graupel or hail, but not both. Although both species are formed by accretion of supercooled cloud droplets on ice crystals at sub-freezing temperatures, graupel is assumed to be far less dense than hail. Because of the characteristic vertical velocities and typical observations of AR precipitation, graupel is thus chosen over hail. The cloud ice and cloud water represent non-precipitating ice and liquid droplets, respectively. All particles are assumed to be spherical for calculating the mass-size relationship. However, the

terminal fallspeed is not itself calculated using a spherical assumption, instead it is based on empirical fallspeed-size relationships in the form of a power law that is a function of diameter.

For numerical simplicity MPs like the Morrison scheme assume the population of ice crystals all have a spherical shape when calculating the mass-size relationship (influencing the size distribution parameters), even though ice crystals come in a diverse range of shapes (e.g., long needles, flat plates, complex dendrites) and different levels of aggregation (snowflakes, graupel, hail). In nature, these different particle shapes/habits and types result in a variability in the particle fall speed and density, which can influence the spatial distribution of precipitation (Mott et al. 2014; Wang et al. 2017). The effects induced by the shape and size variability are approximated through the use of tunable parameters, whose values have an inherent variability and natural uncertainty. These parameters are associated with particle characteristics (e.g., particle density and fallspeed parameters), conversion thresholds (e.g., self-collection of cloud water to form rain (autoconversion) or rimed snow converted to graupel), collection efficiencies (e.g., cloud water-ice, ice-ice), and processes such as snow deposition, collision-coalescence, or riming. Changes in these parameters have been shown to affect cloud development and precipitation (Jankov et al. 2007, 2009; Liu et al. 2011). For example, reducing the speed at which a snow particle falls can shift maximum snowfall from the windward to lee side of a mountain (Colle and Mass 2000).

Over the past decade, effort has been made to produce MPs that allow ice particle types to vary as a function of different process rates such as riming and deposition as opposed to arbitrary conversion thresholds between pre-determined and fixed ice categories (e.g., Morrison

and Milbrandt 2015). More complex schemes also exist that predict the ice particle habits, as well as the mass, shape, size, density, and fall speed (e.g., Jensen et al. 2018). The use of these schemes is beyond the scope of this dissertation.

1.5 Specific Aims

ARs make landfall on every continent and can often coincide with mountainous regions, resulting in moist air to be forced to rise over the terrain. If there is enough moisture and ascent, clouds can form and the subsequent precipitation developed is termed orographic precipitation. In general, the heaviest orographic precipitation occurs on the upwind side of the mountain and can lead to flooding and landslides, while also providing a large percentage of the annual precipitation for regions downstream.

NWP and climate models used to understand precipitation distributions and development cannot directly resolve many of the physical processes occurring within the atmosphere, thus physical parameterizations are created to approximate the small-scale processes. The simplification of physical processes, such as cloud and precipitation processes, introduces uncertainty in the model. Although different sources of uncertainty exist, this dissertation focuses on cloud microphysical processes. Parameters within microphysical schemes represent simplified processes and contain natural variability, e.g., a parameter varies spatially/temporally but is constant in the model, and inherent uncertainty from limited observations and measuring capabilities. Additionally, phase changes within the cloud can influence the latent heat exchange in the environment, thus leading to impacts on the dynamics and thermodynamics of the system.

The upstream environmental conditions can also impact the processes within the cloud and the precipitation development, i.e., temperature can impact the precipitation type, and wind speeds and moisture content can affect condensation rates. Therefore, this dissertation aims to explore the quantitative sensitivity of orographic precipitation from an AR to microphysical and environmental parameter perturbations. The main science question explored here is: *how do cloud processes and environmental conditions affect orographic precipitation when an atmospheric river interacts with a mountain?* This question is approached through idealized numerical model experiments and the application of statistical methods in studies described below and presented in Chapters 2, 3, and 4.

Chapter 2 (Morales et al. 2018) explores the hypothesis that perturbations to microphysical parameters will exert a strong influence on orographic precipitation location and amount due to effects on the thermodynamics and dynamics caused by changes to latent heat release. The primary analysis focuses on the importance of microphysical parameters, with a secondary analysis investigating how the environment could affect the precipitation sensitivities to microphysical parameter perturbations. The study uses an idealized modeling framework and systematic perturbations of numerous microphysical parameters to explore the precipitation sensitivity. Although prior work has explored microphysical parameters in the past (Hobbs et al. 1973; Colle and Mass 2000; Colle 2004; Colle and Zeng 2004a,b; Colle et al. 2005; Miglietta and Rotunno 2006; Jankov et al. 2007, 2009; Lin and Colle 2009, 2011; Liu et al. 2011; Morrison et al. 2015), this is the first study evaluate a large number of parameters corresponding to ice and warm-rain processes for an environment characteristic of an atmospheric river. In

addition, the study explores how the precipitation sensitivities would change in an environment with a lower freezing level and a weaker horizontal wind speed profile.

Given the results from Chapter 2, Chapter 3 applied a more complex sensitivity analysis method to better understand if the simultaneous perturbation of parameters impacts the precipitation sensitivity to individual parameters (Morales et al. 2019). Additionally, multiple microphysical and environmental parameters are tested simultaneously to determine if microphysical parameters or environmental conditions are most influential to orographic precipitation within an atmospheric river environment. The main hypothesis tested here asserts that different combinations of microphysical parameters and environmental conditions could act to enhance, reduce, or nullify the impacts on orographic precipitation through complex interactions. This study used the Morris One-at-A-Time (MOAT) method (Morris 1991; Campolongo et al. 2007), which allowed for the simultaneous perturbation of multiple parameters and screen out parameters that were least influential to precipitation. This method was applied for the first time to the study of orographic precipitation and provided additional information on non-linear parameter interactions.

Results from Chapter 3 showed differences in the most influential parameters for different precipitation types (frozen vs liquid). Thus, Chapter 4 (Morales et al. 2019, in prep.) focuses on precipitation type and tests the following hypothesis: environmental conditions will affect the type of precipitation more so than perturbations to microphysical parameter perturbations. Results from Chapter 3 suggest that some parameters may interact with one another, i.e., the value of some parameter may influence the effect of another parameter on

precipitation. Therefore, this project explores any possible covariance in parameters through the application of a Markov Chain Monte Carlo (MCMC) method to the subset of parameters most influential to precipitation found in Chapter 3.

The motivation, background, methodology, and results for all three projects described above are found in Chapters 2, 3, and 4, respectively. Chapter 4 contains the results of the ongoing MCMC experiment, to be submitted for publication post-defense. Chapter 5 presents a summary and the general conclusions of this dissertation, and presents possible areas of future work, remaining science questions, and applications of this research.

Chapter 2. Orographic Precipitation Response to Microphysical Parameter Perturbations (Morales et al. 2018)

2.1 Introduction

Orographic precipitation during non-convective events commonly occurs in environments characterized by moist nearly neutral conditions. This type of flow allows for little resistance to orographic lifting resulting in enhancement of precipitation over windward mountain slopes (Miglietta and Rotunno 2005, 2006; hereafter MR05 and MR06). Atmospheric rivers (ARs) have been observed to have moist nearly neutral static stability in the lower levels of the troposphere, as well as high surface potential temperatures (approx. 285-289 K), strong wind speeds (low-level jet >20 m/s), high freezing level, and nearly saturated conditions (Ralph et al. 2005). When ARs interact with topography they can produce intense precipitation, triggering flooding and mudslides resulting in devastating and costly impacts to local infrastructure and loss of life and property (Ralph et al. 2006; Neiman et al. 2008b; Leung and Qian, 2009; Ralph et al. 2011).

In California, ARs are responsible for 20-50% of the annual precipitation (Dettinger et al. 2011), often from only a few storms producing large amounts of snow resulting in snowpack reaching "near-record levels of snow water equivalent" (Guan et al. 2010; Guan et al. 2013). Guan et al. (2013) found that lower than normal surface air temperatures during AR events favor increased snow accumulation over the Sierra Nevada. Colder AR events have lower amounts of integrated water vapor, yet they result in a higher snow-to-rain ratio and higher overall

precipitation values (Guan et al. 2010). Freezing level can also play an important role in snowpack stability. High freezing levels can shift precipitation from snow to rain (Yuter and Houze 2003; Colle et al. 2005a). Rain falling on snowpack can promote early snowmelt (Kim et al. 2013) and create challenges for water resource managers. Past studies have also found that a high freezing level affects where precipitation will fall, resulting in less downwind transport and a peak in precipitation on windward slopes or near peak elevations (Colle 2004; MR06; Stoelinga et al. 2013).

Complex interactions between mountain geometry, thermodynamics, and cloud microphysics can also control precipitation type, amount, and its location over a mountain (Lin et al. 2001; Jiang and Smith 2003; Stoelinga et al. 2003; Colle 2004; MR05; MR06; Tushaus et al. 2015 (hereafter T15)). For example, a wide barrier (≥30 km half-width) will provide more time for snow growth aloft, while a narrower barrier will generate more graupel through the collection of supercooled cloud droplets (Colle and Zeng 2004b). Wider barriers are thus more sensitive to parameters such as snow fall speed over the windward slope. Hobbs et al. (1973) demonstrated the degree of ice particle riming influences where ice particles will precipitate over a mountain, i.e., heavily rimed particles fall out faster and land on the windward slope.

Microphysical parameterizations are implemented in weather forecast models to represent the development of clouds and precipitation. Simulated orographic precipitation for both AR and non-AR events has been found to be sensitive to the choice of microphysics scheme (Jankov et al. 2007, 2009; Liu et al. 2011). Sensitivity studies exploring the effects of microphysical parameters on orographic precipitation show changes in these parameters can

impact cloud and precipitation development. Colle and Mass (2000) found lower snow fall speeds shifted precipitation from the windward to lee side of the barrier during an AR over the Pacific Northwest. Colle and Zeng (2004a) found condensation, snow deposition, and riming and melting of graupel contributed most to the development of surface precipitation on the upwind slope. Their results also showed surface precipitation and microphysical processes were most sensitive to parameters associated with snow/graupel fall speeds, CCN concentrations, and snow size distribution, and less with ice initiation and autoconversion. A similar study performed over the Cascade Mountains (Colle et al. 2005) also found strong sensitivity to snow size distribution and fall speed parameters, as well as having cloud water accretion and melting of graupel and snow contribute to most of the surface precipitation production. Colle et al. 2005 found riming processes to be important for the amount and distribution of supercooled water within clouds, affecting snow growth upwind.

These microphysical parameters have both uncertainty and inherent variability. Uncertainty arises because some parameters have a measurable uncertainty (e.g., particle densities, fall speeds), while others are uncertain because of limited measuring capabilities (e.g., process rates) or because they do not correspond to any physical, observable quantity in nature (e.g., autoconversion thresholds). There are also parameters whose values are known to vary spatially and temporally, beyond the range of measurement uncertainty, but are constant in the model. Uncertainty and variability in these parameter values leads us to ask the question: what is the sensitivity of orographic precipitation to changes in microphysical parameters?

We hypothesize that microphysics exerts a strong influence on the amount and location of orographic precipitation within moist nearly neutral conditions, such as those found within ARs. Changes in these microphysical parameters can then have secondary effects on the thermodynamics and dynamics through latent heating (Morales et al. 2015). Overall, we surmise microphysical parameter and process changes may result in non-linear responses due to complex interactions between parameters within the microphysics scheme. While orographic precipitation may vary with changes to microphysical parameter and process, will these responses differ if the upstream environment is also perturbed? Past studies by MR05, MR06, and T15 have shown a non-linear dependence of simulated precipitation to parameters controlling mountain geometry, mean zonal wind speed, moist static stability, relative humidity, and surface potential temperature. For example, increasing surface potential temperature did not result in higher rain rates on upwind slopes, since processes such as riming occur at lower temperatures and can contribute to surface precipitation (MR06). T15 performed a more systematic analysis of the parameter space for mountain geometry and upstream conditions, finding non-monotonic responses for mountain half-width, moist static stability, and mean zonal wind speed and monotonic responses to mountain height, relative humidity, and surface potential temperature. Their study focused on liquid-only microphysics. We extend this analysis to include ice microphysics and ask the following question: how will the sensitivities to changes in microphysical parameters change with different environments?

Following work by MR05, MR06, and T15, this study focuses on moist nearly neutral flow over a two-dimensional (2D) Gaussian-shaped mountain barrier and explores the

sensitivities of orographic precipitation to changes in microphysical parameters in different environments. We utilize an idealized modeling framework, which allows us to reduce model complexity and isolate the most important physical controls on orographic precipitation within the Cloud Model 1 (CM1).

2.2 Methodology

2.2.1 Model Configuration

The idealized simulations in this study were performed using version 17 of the Cloud Model 1 (CM1; Bryan and Fritsch 2002). CM1 is a non-hydrostatic atmospheric model designed for modeling of cloud-scale processes. Following MR05, MR06, and T15, our configuration uses a 2D domain with a horizontally stretched x-grid where the horizontal grid spacing is 2 km for the inner domain (1200 km in length) and stretches up to 6 km over 50 grid points on either side. The domain is 1600 km in length, and the total depth is 18 km with 55 vertical levels. The vertical grid spacing is 0.25 km from the surface to a height of 9 km, increases to 0.5 km between 9 and 10.5 km, then remains constant at 0.5 km until 18 km.

Lateral boundary conditions are open-radiative, with a no slip bottom boundary condition and free slip top boundary condition. A positive definite advection scheme is used and a Rayleigh damper with damping coefficient of 0.0003 s^{-2} is applied to the top 4 km to prevent reflection of vertically propagating gravity waves. Although interactions of radiation with the mountain surface can result in the forcing of mesoscale mountain circulations, e.g., mountain-valley winds, our focus is on the interaction of microphysics and dynamics. Thus, radiative

transfer and surface heat flux parameterizations are neglected. All simulations are run for 20 hours at a time step of 3 s. The Morrison microphysics scheme version 3.4 (Morrison et al. 2005, 2009) is used for all microphysical parameter perturbation experiments. The Morrison scheme is a two-moment bulk microphysical parameterization that prognoses mass and number mixing ratios of four hydrometeor categories: rain, cloud ice, snow, and the choice of either graupel or hail. It also prognoses the mass mixing ratio of cloud liquid water, and in the version used here specifies a constant cloud droplet number concentration (set to 200 cm^{-3}). The rimed ice species in the experiments presented here is set to graupel. For rain, cloud ice, snow, and graupel, the particle size distributions (PSDs) are described by inverse exponential functions. For cloud liquid water, the PSD follows a gamma function with a shape parameter that depends on the specified cloud water number concentration. Analysis of the precipitation produced by each simulation utilizes 5-min output cadence during simulated hours 6-20, as the precipitation rate, cross-mountain flow, and spatial distribution of cloud is relatively steady during this time period.

2.2.2 Experimental design – Control

The environmental parameters for the idealized sounding are guided by observations of an AR event during the Olympic Mountains Experiment (OLYMPEX; Houze et al. 2016). The observed sounding (Figure 2.1a) was taken at 0300 UTC on 13 Nov 2015 at the base of the Quinault River Valley in Washington state (Zagrodnik et al. 2017, submitted). Our goal in idealizing this sounding was to create a realistic environment described by as few parameters as possible; thus, the observed profile was smoothed using a simple 1-2-1 filter and characteristic values for each parameter were determined. Table 2.1 lists the environmental parameters

calculated from the observed sounding. Moist Brunt-Väisälä frequency (N_m^2) for the troposphere (4×10^{-5} s^{-2}) and stratosphere (5×10^{-4} s^{-2}) was calculated by averaging N_m^2 below and above the tropopause height (approx. 12 km), respectively, using equation (36) of Durran and Klemp (1982). Within CM1 equation (13) is used for N_m^2, along with equation (19) for the moist adiabatic lapse rate, found in Durran and Klemp (1982).

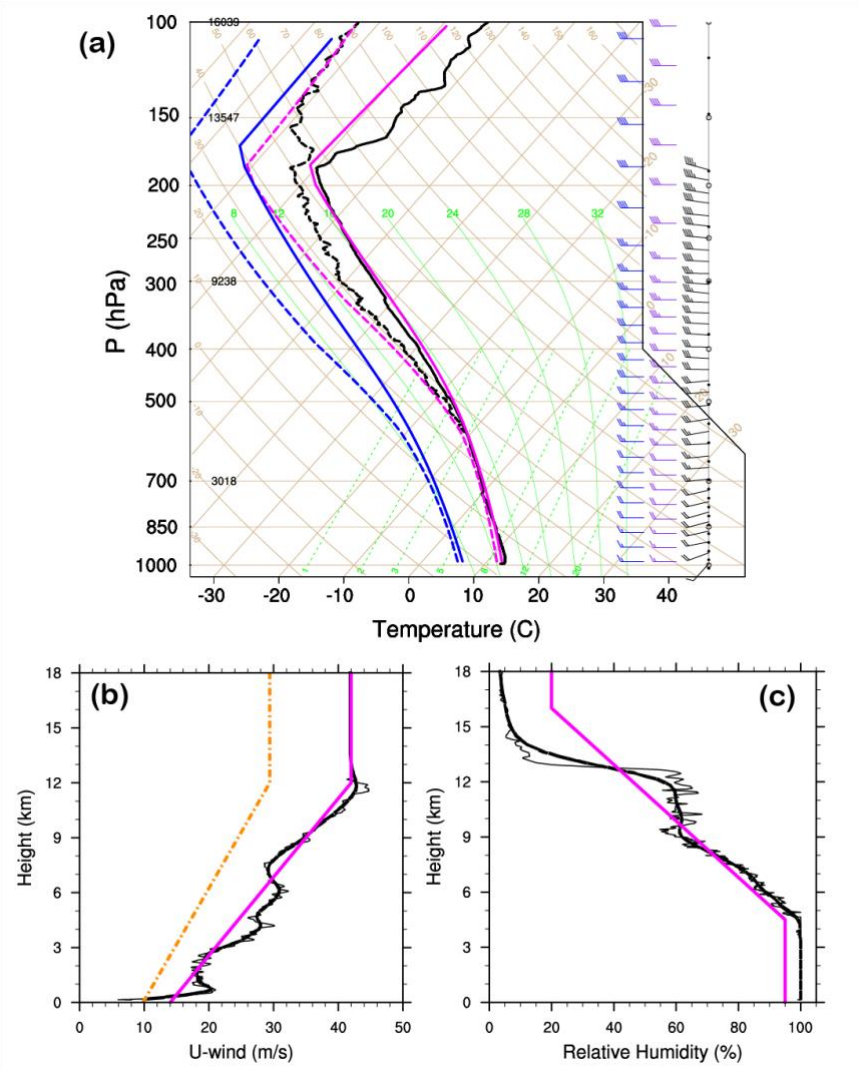

Figure 2.1 a) Skew-T diagram showing the observed sounding from OLYMPEX 13 Nov 2015 (black), idealized sounding (magenta), and lower freezing level (LowFL) sounding (blue). For all

soundings, solid lines represent temperature and dashed lines represent dewpoint temperature, all in Celsius. (b) Vertical profile of zonal wind speed (m/s) showing the observed winds (thin black line), smoothed profile (thick black line), idealized profile (magenta), and reduced wind profile (LowU, dot-dash orange). (c) Vertical profile of relative humidity (%) showing the observed values (thin black line), smoothed profile (thick black line), and idealized profile (magenta).

Table 2.1 List of parameters describing the environmental sounding and mountain geometry.

Parameter description (Symbol)	Control	Units
Squared moist Brunt– Vaisala frequency for troposphere ($N^2_{m,Trop}$)	4×10^{-5}	s^{-2}
Squared moist Brunt– Vaisala frequency for stratosphere ($N^2_{m,Strat}$)	5×10^{-4}	s^{-2}
Surface potential temperature (θ_{sfc})	286	K
Mountain height (H_{mtn})	1×10^{3}	m
Mountain half-width (W_{mtn})	4×10^{4}	m

The surface potential temperature is set to 286 K. Figure 2.1b shows the original wind profile, which is smoothed and idealized with linearly increasing winds of 14 m/s at the surface to 42 m/s at a height of 12 km, and constant winds at 42 m/s above 12 km. The idealized wind profile contains no directional shear, i.e., zonal winds are perpendicular to the barrier. The relative humidity (RH) profile (Figure 2.1c) is divided into three layers: below 4.5 km, between 4.5 km and 12 km, and above 12 km. This sounding has already likely undergone humidification relative to the upstream conditions through flow interaction with the barrier, thus the RH below 4.5 km was decreased to 95% in order to have initial conditions representative of air not yet forced to rise. This sub-saturated profile also helps limit cloud development far upstream before the flow approaches the barrier. The RH profile linearly decreases with height from 95% at 4.5 km to 20% at 12 km, and remains constant at that value up to the model top (Figure 2.1c).

The idealized mountain barrier is created using the following equation from MR05, MR06, and T15,

$$h(x) = \frac{H_{mtn}}{1+\left[\frac{x-x_0}{W_{mtn}}\right]^2}, \tag{2.1}$$

where mountain height (h) is a function of the horizontal position within the domain (x) and is described using the maximum mountain height (H_{mtn}), the center of the mountain (x_0), and the mountain half-width (W_{mtn}). The center of the mountain is shifted 400 km downstream of the center of the domain to reduce influence of mountain-generated upstream-propagating waves on the flow entering at the upstream boundary.

Again, we use observations to guide the barrier characteristic parameters by averaging the elevation over a 0.6° latitude-wide box through the center of the Olympic Mountains (Figure 2.2). From the observations, the barrier is idealized to a maximum height of 1 km and a half-width of 40 km (Table 2.1). This mountain shape was chosen to match as closely as possible the upwind slope and mean height of the Olympic mountains. Although the environmental sounding and mountain geometry are idealized from observations, our aim is *not* to simulate the exact evolution of the 13 Nov 2015 event, but to use these observations to anchor our simulations in reality.

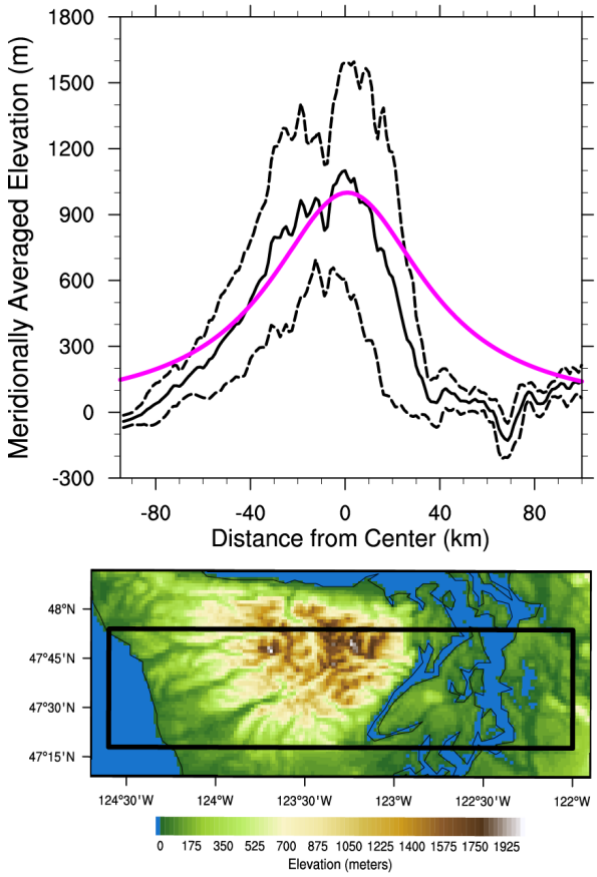

Figure 2.2 Meridionally-averaged elevation over a 0.6° latitude-wide box including the center of the Olympic Mountains and the Quinault river valley (black box in bottom map). Solid black line depicts mean topography, dashed black lines correspond to +/- standard deviation, and magenta line corresponds to the idealized mountain shape used in CM1 simulations (height of 1 km, half-width of 40 km).

2.2.3 Microphysical Parameters

One-at-a-time parameter perturbation experiments were performed on the previously described control simulation using the microphysics parameters listed in Table 2.2. Some parameters are associated with physical characteristics of the frozen hydrometeors, e.g., fall speed coefficient (A) and bulk particle density (ρ) of cloud ice (i), snow (s), and graupel (g), and

have an empirical range of values. Others are parameters within microphysics parameterizations that do not correspond to a real physical quantity, e.g., autoconversion thresholds, and thus they generally have a greater range of uncertainty. Within the Morrison scheme, like other schemes, there exist "hard-wired" thresholds for autoconversion rates and other processes, thus we create parameters acting as multiplicative factors in order to vary the processes. Multiplicative factors are used to perturb the processes of cloud water autoconversion, rain accretion, and snow deposition to represent the uncertainty and inherent variability associated with these processes. The control values are the default settings for these parameters within the Morrison scheme. For parameters which describe observable cloud properties (e.g., fall speeds and particle densities) the range of values is set to a consistent range from observations. The other parameters are varied over a range of plausible values. Each one-parameter perturbation experiment has five points, i.e., the control value, the min and max, and values between the control and min/max. Based on the complex interactions and feedbacks microphysics can have on the system, we surmise that the responses to changes in the microphysical parameters will be non-linear and test five values per parameter to explore this idea. The precipitation rate responses to microphysical parameter changes are assessed over six regions on the mountain where spatial averaging is performed: the upwind foothills, slope, and top and the downwind foothills, slope, and top (Figure 2.3c).

Table 2.2 List of microphysical parameters, including control values and range over which the parameters are perturbed. Parameters in bold are those which have the largest impact on surface precipitation in the control simulation.

Parameter description (Symbol)	Control	Min	Max	Units
Cloud ice fall speed coefficient (A_i)	700	350	1050	$m^{(1-b)}\ s^{-1}$
Snow fall speed coefficient (A_s)	**11.72**	**5.86**	**17.58**	**$m^{(1-b)}\ s^{-1}$**
Graupel fall speed coefficient (A_g)	19.3	9.65	28.95	$m^{(1-b)}\ s^{-1}$
Cloud ice density (ρ_i)	500	250	750	$kg\ m^{-3}$
Snow density (ρ_s)	**100**	**50**	**150**	**$kg\ m^{-3}$**
Graupel density (ρ_g)	400	200	600	$kg\ m^{-3}$
Cloud ice autoconversion threshold (DCS)	125	50	200	μm
Nucleated ice crystal radius (RMI0)	10	1	30	μm
Embryo graupel radius (RMG0)	45.71	35	1000	μm
Ice-Ice collection efficiency (EII)	0.1	0.01	1	--
Ice-cloud water collection efficiency (ECI)	**0.7**	**0.3**	**1**	**--**
Radius of splintered ice particle (RMMULT)	5	1	30	μm
Rain accretion factor (WRA)	**1**	**0.5**	**2**	**--**
Cloud water autoconversion factor (WRC)	1	0.1	10	--
Snow deposition factor (SDEP)	1	0.5	2	--

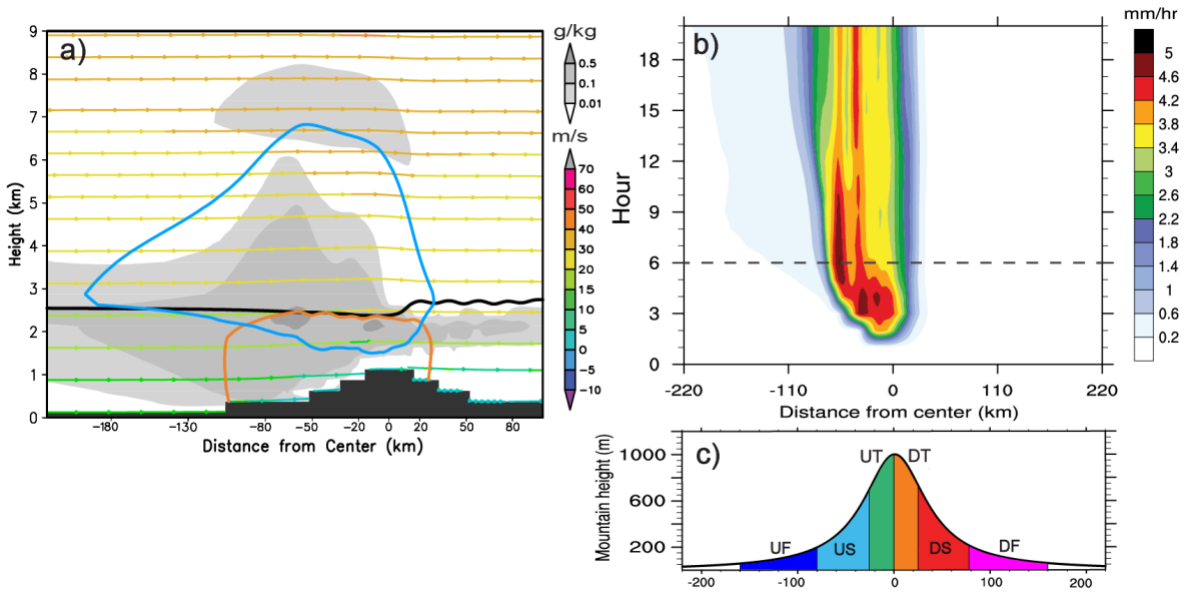

Figure 2.3 **(**a) Vertical cross-section over a portion of the domain of the control simulation showing temporally-averaged (hours 6-20) streamlines colored with wind speed (m s^{-1}), cloud water and ice mixing ratios (gray shaded contours, g kg^{-1}), snow mixing ratio (0.05 g kg^{-1} contour, cerulean), rain mixing ratio (0.05 g kg^{-1} contour, orange), and freezing level (black line). (b) Hovmöller diagram of precipitation rate (mm/hr) with simulation time (hours) on the ordinate and distance from center of the mountain (km) on the abscissa. Dashed gray line corresponds to hour 6, start of temporal averaging. (c) Mountain height (m) profile with the 6 averaging regions used for the calculations: upwind foothills (UF), slope (US), top (UT), and downwind top (DT), slope (DS), and foothills (DF).

2.2.4 Experimental Design – Environmental Tests

Two additional experiments are performed to test if the sensitivities to changes in microphysical parameters remain the same with a different environment. The first environmental test involves scaling down the wind profile. The control wind profile has high cross-barrier wind speeds (~16 m/s); the strong dynamical forcing in this case may exert a large influence on the precipitation response to microphysical parameter changes. To explore how changes in the dynamical forcing impact the precipitation response to microphysical parameter perturbations,

the first environmental test reduces the wind speeds by 30% throughout the entire profile (hereafter experiment LowU, Figure 2.1b). In addition, T15 found that adjusting the environment can lead to large changes in precipitation for a similar idealized moist neutral environment. Their results found zonal wind speed to be a dominant control on precipitation, leading to a non-monotonic upwind precipitation response to changes in wind speed.

The second environmental test explores the impact of the freezing level height on the changes in microphysics parameters/processes. The freezing level in the control is at a height of approximately 2.6 km, which may result in warm-rain processes dominating the production of precipitation at the surface. To explore how changes to the most influential microphysical parameters are affected in an environment where ice processes play a larger role in precipitation production, the freezing level is lowered by reducing the surface potential temperature by 6 K while retaining the same profile of N_m^2 (hereafter experiment LowFL, Figure 2.1a). This new atmospheric profile has an initial freezing level at a height of approx. 1.3 km, which descends to below the mountain top after hour 3 of the simulation, likely through adiabatic ascent and melting of graupel and snow that cool air near the mountain top.

2.3 Results and Discussion

2.3.1 Control Simulation

A cloud forms on the upwind slope and top of the mountain with a depth of approximately 7 km within the first hour of our idealized simulation (not shown). Surface precipitation also occurs within the first hour of the simulation (Figure 2.3b) through warm-rain

processes and increases after the generation of snow and graupel. The high freezing level (approximately at 2.5 km height) provides sufficient distance for frozen hydrometeors to melt before reaching the surface. After hour 6, the mid-level cloud over the upwind slope begins to dissipate, seemingly due to the Wegener-Bergeron-Findeisen process as snow development extends upstream (not shown), and the upper-level cloud becomes detached from the parent cloud, persisting for the rest of the simulation (Figure 2.3a). A shallow cloud forms between 2-3 km heights and extends across the domain, and a deep cloud containing high mass mixing ratios (> 0.5 g kg^{-1}) persists over the upwind mountain side (Figure 2.3a). Also, after hour 6, graupel no longer occurs and the orographic precipitation system becomes quasi-steady. Thus, we neglect the initial transient graupel feature and perform our temporal averaging over hours 6-20. Melting of snow, in addition to warm-rain processes, provide the quasi-steady precipitation from hours 6-20 with the highest precipitation rates occurring over the upwind slope (maximum rate of 5.02 mm hr^{-1}; Figure 2.3b,c).

In general, the flow is laminar (i.e., there are no breaking waves, rotors, or strong lee waves) as it traverses the barrier. Downwind we see an elevated freezing level (Figure 2.3a), likely due to adiabatic warming from descending winds on the lee side of the mountain. There are also low amplitude lee waves, which trigger shallow cloud development downstream (Figure 2.3a). The freezing level remains fairly constant at $z = 2.6$ km far upstream, while sloping downward near the upwind top of the mountain (Figure 2.3a). This downward sloping of the freezing level was observed during OLYMPEX (Houze et al. 2016) and has been suggested to be a result of a combination of processes: latent cooling from snow melting, adiabatic cooling from

upslope lifting, and the melting distance of hydrometeors, which is controlled by particle size and density, as well as ambient conditions (Marwitz 1987; Medina et al. 2005; Minder et al. 2011). The freezing level does not become low enough to reach the mountain top in our control simulation.

As mentioned in the Methods section, the goal of this study is not to simulate the events of 13 Nov 2015 exactly, but to use observations from this atmospheric river case to guide our upstream environmental conditions. Nevertheless, it is encouraging to see a similar magnitude of orographic enhancement in our idealized control simulation (precipitation rate over UT/precipitation rate over UF = 5.6) compared to the observed enhancement of 4-5 on 13 Nov 2015 (A. Rowe, 2017, personal communication). Our idealized simulation also had the highest precipitation rates occur on the upwind slope and not on the highest peak, which was similarly observed during this OLYMPEX case (Zagrodnik et al. 2017, submitted). Thus, we are confident in our control simulation and its ability to provide understanding of this moist nearly neutral environment.

2.3.2 Microphysical Parameter Perturbations

Perturbations were performed on the control simulation to explore the sensitivity of orographic precipitation and cloud development to changes in various parameters within the Morrison scheme. Table 2.2 lists all of the parameters tested, as well as the range of values over which the parameter perturbations were performed.

To understand the overall effect of these parameters on the control simulation, the relative change (%) within each set of parameter perturbations was calculated by taking the

difference between the maximum and minimum response values and dividing it by the average of the five response values. All values are temporally and spatially averaged over hours 6-20 for the 6 mountain regions described in Figure 2.3c. Figure 2.4 shows the relative change for precipitation rate (PREC; mm hr^{-1}), and liquid and ice water paths (LWP and IWP, respectively; kg m^{-2}). LWP is the total amount of cloud water and rain between the surface and model top, calculated by vertically-integrating the cloud water and rain mixing ratios. Similarly, IWP represents vertically-integrated cloud ice, snow, and graupel mixing ratios. Overall, some parameters have little influence (< 20%) on our output metrics (PREC, LWP, and IWP), while others have a larger influence over specific regions or across the entire mountain. Downwind regions have the highest relative change, mostly because the PREC, LWP, and IWP there have small magnitudes and hence small absolute changes will result in large relative changes. There are four parameters which stand out because of large relative responses or widespread impacts on PREC, LWP, and IWP: snow particle fall speed coefficient (A_s), snow particle density (ρ_s), ice-cloud water collection efficiency (ECI), and rain accretion multiplicative factor (WRA) (Fig. 2.4). A_s and ρ_s describe hydrometeor characteristics, while ECI and WRA are associated with cloud water collection by ice species and rain, respectively. We focus on the responses to perturbing these four parameters in the rest of this section.

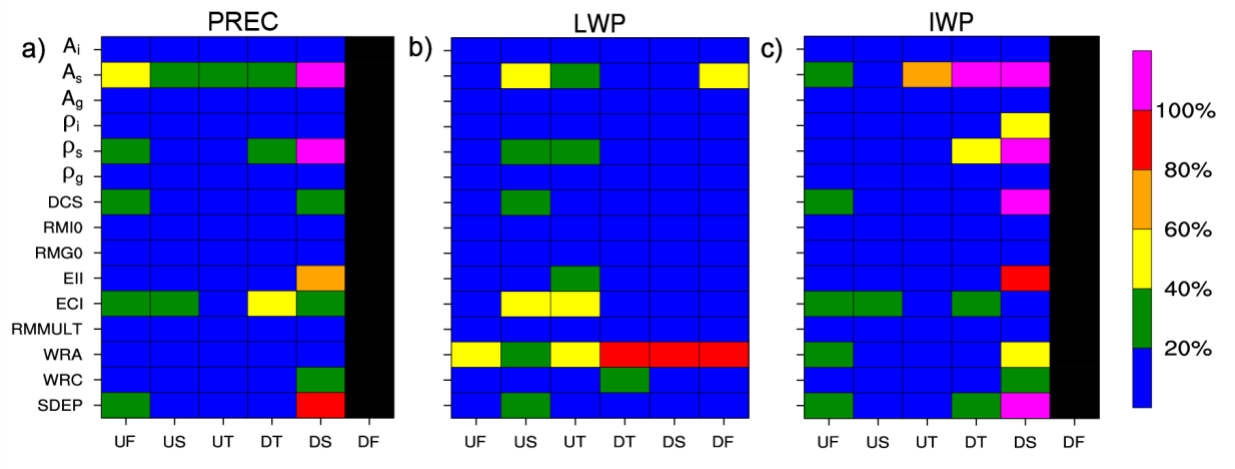

Figure 2.4 Percent relative change given by 100 x (max-min)/average for each 5-point parameter perturbation experiment for (a) precipitation rate (PREC; mm hr^{-1}), (b) liquid water path (LWP includes cloud water and rain mixing ratios; kg m^{-2}), and (c) ice water path (IWP includes cloud ice, snow, and graupel mixing ratios; kg m^{-2}). Black colors denote undefined values, i.e. infinity. Ordinate: list of parameter symbols defined in Table 2.2. Abscissa: averaging regions over the mountain shown in Figure 2.3c.

Hovmöller diagrams in Figure 2.5 provide information on the impact on precipitation location and amount compared to the control simulation for each parameter perturbation. Overall, the effect on precipitation amount is largest at lower perturbation values (left two columns in Figure 2.5) for A_s, ρ_s, and ECI, and at the minimum and maximum values for WRA (Figure 2.5m,p). Given that the control simulation's maximum precipitation value is 5 mm hr^{-1}, the parameter perturbations result in precipitation changes ranging from a 42% decrease (Figure 2.5m) to a 30% increase (Figure 2.5e). For low values of A_s, less precipitation falls on the upwind side (Figure 2.5a-d), while ρ_s has the opposite effect where less precipitation falls downwind for low ρ_s values (Figure 2.5e-h). ECI precipitation responses are similar to A_s (less precipitation upwind for lower values), but with changes occurring over a narrower region

(Figure 2.5i-l). At the maximum value of WRA (WRA=2; Figure 2.5p) we see more surface precipitation over the upwind slope/top, while the minimum value (WRA=0.5; Figure 2.5m) shows more precipitation over the upwind slope/top initially but shifting with time to the upwind foothills, in contrast to A_s, ρ_s, and ECI which has a consistent spatial change in precipitation with time.

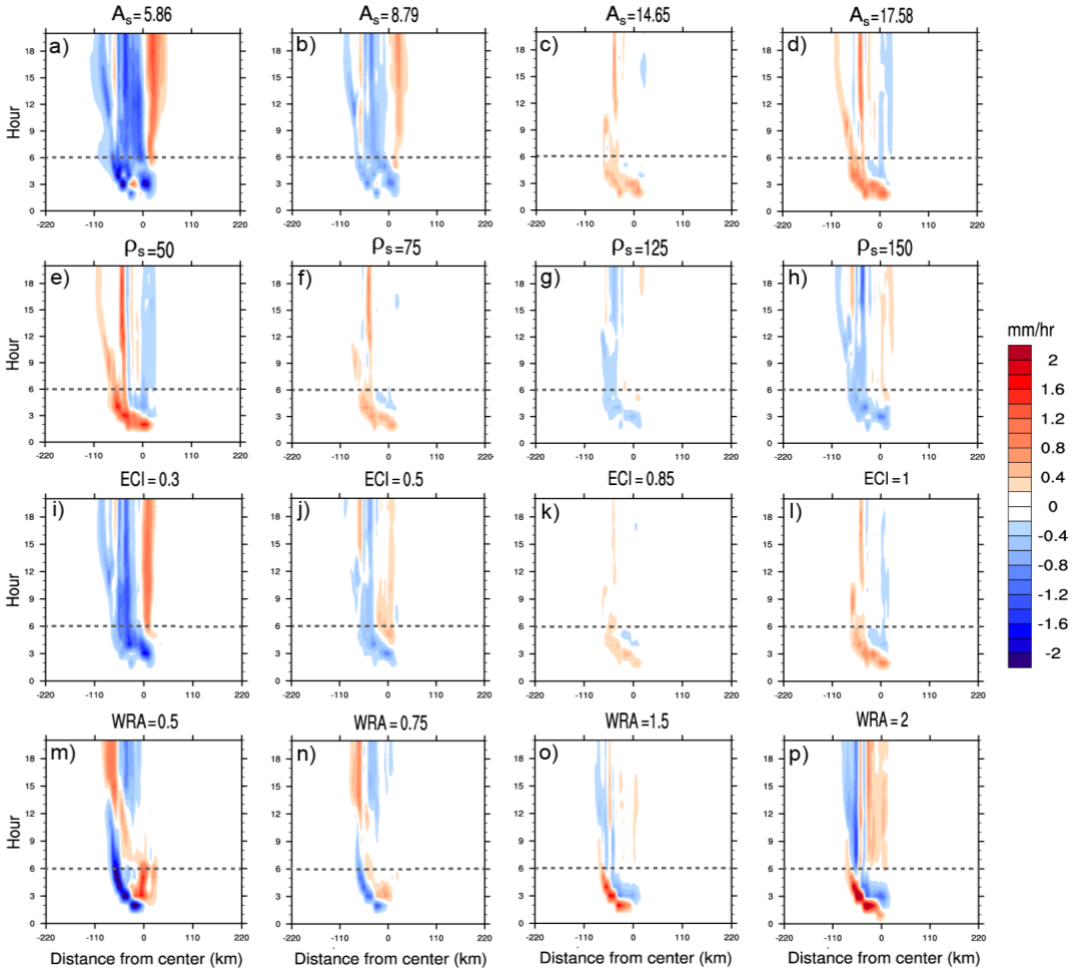

Figure 2.5 Hovmöller diagrams of precipitation rate difference (mm hr^{-1}) between microphysics parameter/process perturbation experiments and the control. Panels show perturbations for (a-d) snow fall speed coefficient (A_S; control=11.72 $m^{(1-b)}$ s^{-1}), (e-h) snow particle density (ρ_s; control=100 kg m^{-3}), (i-l) ice-cloud water collection efficiency (ECI; control=0.7), and (m-p)

cloud water accretion by rain (WRA; control=1). Blue colors represent larger rain rates for the control, red colors represent larger rain rates for the parameter perturbation experiment. Dotted lines show hour 6, where temporal averaging begins.

We next present temporally averaged (hours 6-20) precipitation rates for each region over the mountain and analyze the response functions to changes in A_s, ρ_s, ECI, and WRA. Precipitation rate (mm hr^{-1}) is further analyzed using the following equation:

$$PREC = PE \langle COND \rangle, \quad (2.2)$$

where surface precipitation rate (PREC) is a product of precipitation efficiency (PE) and vertically-integrated total condensation rate (<COND>, mm hr^{-1}). Total condensation rate includes all processes that convert water vapor to condensate, i.e., cloud ice, snow, and graupel deposition and cloud water condensation, which are then vertically-integrated (indicated by < >) from the surface to model top. In the model, <COND> depends mainly on the vertical air velocity in saturated conditions, and therefore changes to <COND> indicate a link to dynamical changes caused by parameter perturbations. PE is directly affected by microphysical parameter perturbations and describes how efficiently condensate is removed from the atmosphere through microphysical processes and sedimentation, resulting in surface precipitation. Since we analyze Equation 2.2 over sub-regions of limited spatial extent, PE is also affected by horizontal advection of condensate. Thus, the response of PE to parameter perturbations shows that a particular parameter has affected the conversion of condensate to vapor (from evaporation or sublimation) and/or transport (sedimentation and horizontal advection). A PE value less than one in the sub-region corresponds to less precipitation reaching the surface compared to the amount of condensate produced within that sub-region. If PE is greater than one, the increase in

precipitation relative to the amount of condensate produced in the column is due to net convergence of the condensed water horizontal advective fluxes across the sub-region. We use this analysis to determine how much condensate is generated (<COND>), how efficient the model is in removing this condensate as surface precipitation, and how both are affected by microphysical parameter perturbations. In our calculations of PE from model output, we take the ratio of the average <COND> and PREC (spatial and temporal) to reduce noise, which can contaminate PE calculated as an average of the ratio.

A_s response functions show a general trend of increasing (decreasing) precipitation rate upwind (downwind) with increasing A_s (Figure 2.6a). Using Equation 2.2 to understand the precipitation response, we see PE has a similar response as precipitation rate, while <COND> is relatively unaffected (Figure 2.6b-c). Perturbations to A_s influence the efficiency of condensate removal through the direct effect that A_s has on the snow particle fall speed in the Morrison scheme:

$$V_s = A_s D^{B_s} , \qquad (2.3)$$

where A_s is the snow fall speed coefficient ($m^{(1-b)} s^{-1}$), D is the particle diameter (m), B_s is an exponent parameter (that we do not vary here), and V_s is the fall speed of snow. Decreasing A_s causes the mass-weighted mean fall speed of snow to decrease, allowing more snow produced upwind of the mountain top to be advected downwind. Because of the change in horizontal advection of snow, the vertically-integrated snow melting rate increases downwind with decreasing A_s (Figure 2.6d). Thus, decreasing A_s reduces the snow terminal fall speed, leading to more snow being transported downwind of the mountain top, and increasing the amount of snow

that melts and reaches the surface as rain there. This is reflected by the increase of PE downwind of the mountain top with a decrease of PE upwind (Figure 2.6b).

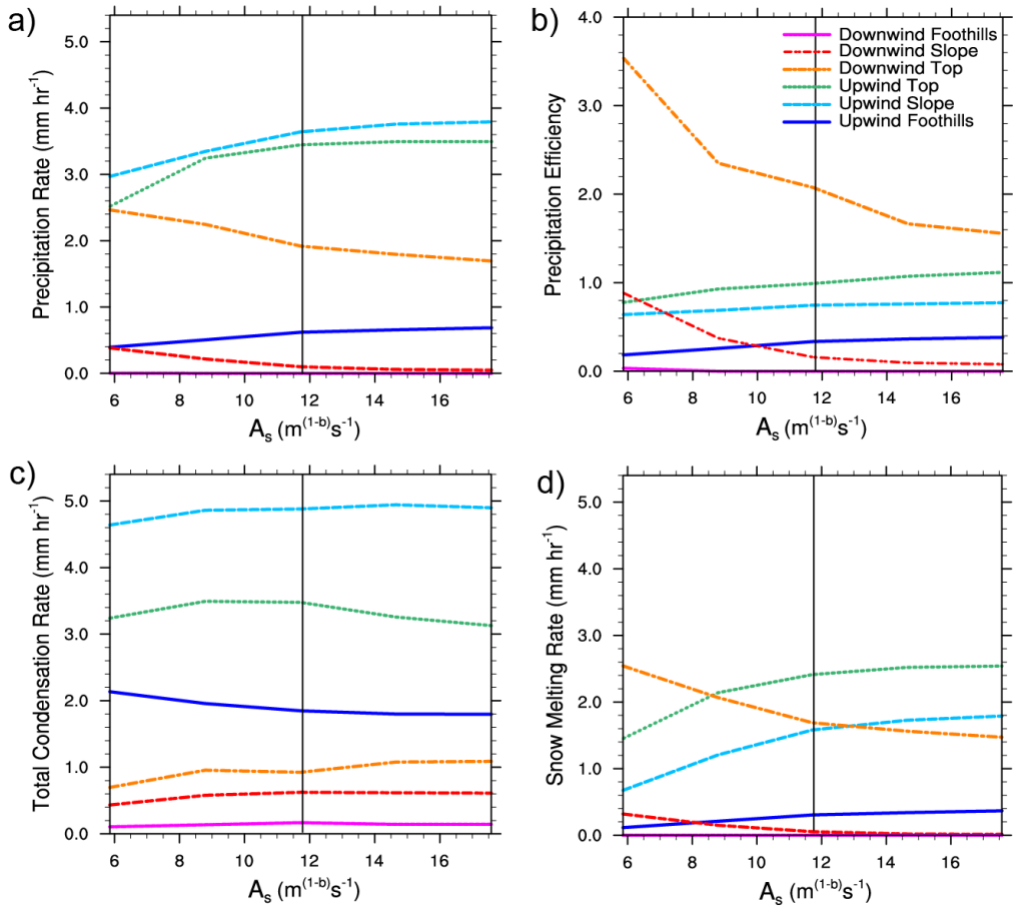

Figure 2.6 Snow fall speed coefficient (A_s; $m^{(1-b)}\ s^{-1}$) response functions for (a) precipitation rate (mm hr^{-1}), (b) precipitation efficiency, (c) vertically-integrated total condensation rate (mm hr^{-1}), and (d) vertically-integrated snow melting rate (mm hr^{-1}). Values are temporally-averaged over hours 6-20 and spatially-averaged over the 6 mountain regions shown in Figure 2.3c. Black vertical lines depict the control parameter value.

Snow density (ρ_s) response functions show the opposite trend compared to A_s; increased (decreased) precipitation rates occur downwind (upwind) with increasing values of ρ_s. Similarly, <COND> is relatively unaffected (Figure 2.7c). From a physical standpoint, it would be

expected that if the bulk density of snow particles is increased they should fall faster. However, in the Morrison scheme, as in almost all microphysics schemes, the snow particle fall speed is only determined through A_s, B_s, and D following Equation 2.3. Nonetheless, the bulk particle density indirectly influences the fall speed through the particle size distribution. The slope parameter (λ), which describes the slope of the gamma particle size distribution, depends on the cubic root of the particle density ($\rho^{1/3}$):

$$\lambda = \left[\frac{\pi \rho N \Gamma(\mu+4)}{6 q \Gamma(\mu+1)}\right]^{\frac{1}{3}}, \qquad (2.4)$$

where q is the mass mixing ratio, N is the number mixing ratio, Γ is the Euler gamma function, and μ is the shape parameter of the size distribution (equal to 0 for snow). Thus, increasing ρ_s for given values of q, N, and μ results in an increase in λ (Equation 2.4). Increasing λ leads to a shift in the particle size distribution towards smaller diameters. Since the particle fall speed is a function of the diameter following Equation 2.3, the shift of the distribution toward smaller particle sizes results in a *decrease* in the mass-weighted mean snow fall speed. This explains the trend in precipitation efficiency for ρ_s: more snow is advected downwind because of the slower mean fall speeds with increasing ρ_s (Figure 2.7b), leading to more snow melting downwind (Figure 2.7d). This relationship between ρ_s and snow fall speed causes an unphysical response in the precipitation rates. This unphysical behavior to changes in particle density has motivated the recent development of schemes that explicitly calculate fall speed as a function of the ratio of the particle mass and projected area, and hence incorporate the effects of particle density in a

physically realistic way (e.g., Lin and Colle 2009, 2011; Harrington et al. 2013; Morrison and Milbrandt 2015).

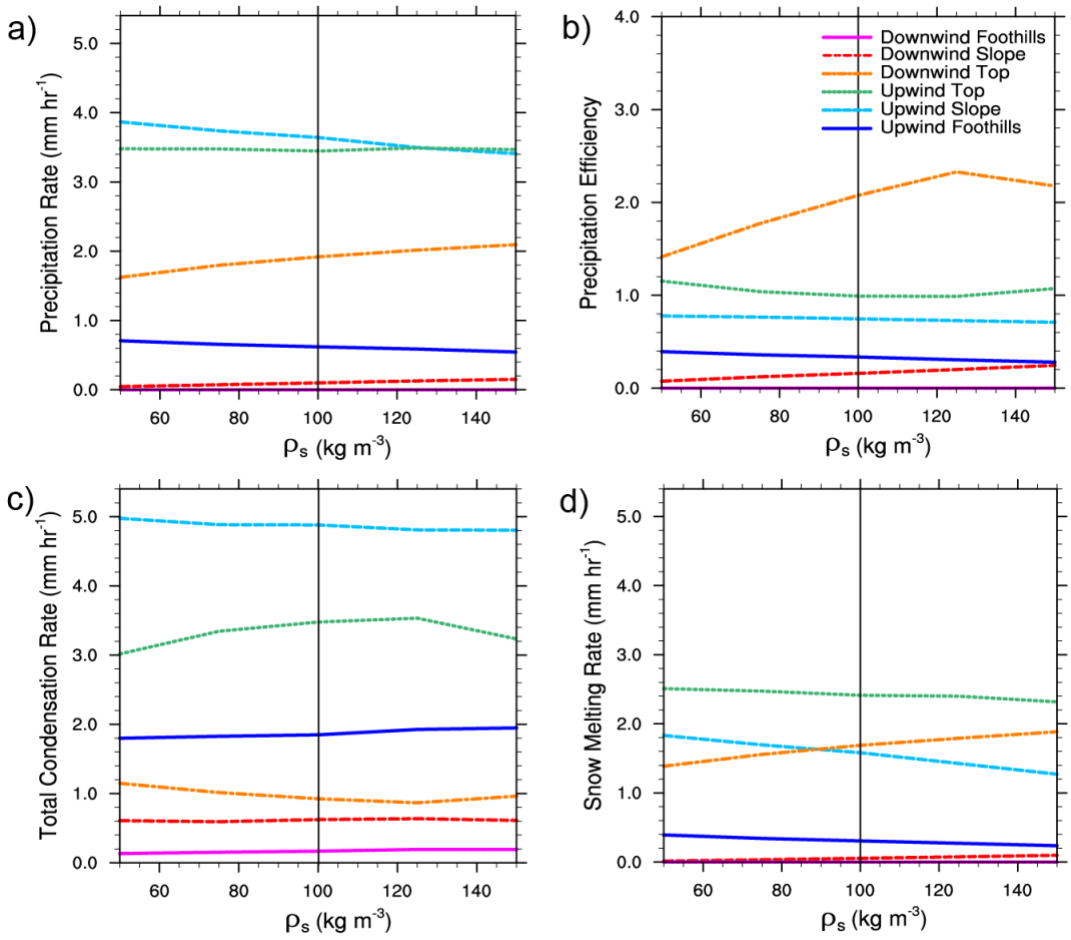

Figure 2.7 Same as Figure 2.6, but for snow particle density (ρ_s; kg m^{-3}).

Response functions for WRA differ from the other parameters, in that there is little effect on PREC (Figure 2.8a). This occurs because of compensation between the effects of increasing PE and decreasing <COND> as WRA increases (Figure 2.8b,c). The WRA parameter is a multiplicative factor which acts to increase or decrease the rain accretion process within the

simulation. Higher WRA corresponds to more efficient removal of cloud water, while lower WRA results in more cloud water remaining within the atmosphere. Therefore, increasing the removal of cloud condensate through higher WRA results in higher PE (Figure 2.8b). This rain accretion process has the largest effect on <COND> compared to the other parameters modified, with a decrease of over 70% on the upwind and downwind tops when WRA is increased from 0.5 to 2 (Figure 2.8c). In all simulations, <COND> is dominated by cloud water condensation which occurs through saturation adjustment in the Morrison scheme. That is, at every time step all excess vapor above water saturation is converted to cloud water, while evaporation is treated by converting cloud water to vapor each time step at a rate that ensures almost exactly saturated conditions are maintained inside liquid cloud. We emphasize that cloud condensation rate using saturation adjustment in the model does *not* depend directly on the number or size of existing cloud droplets.

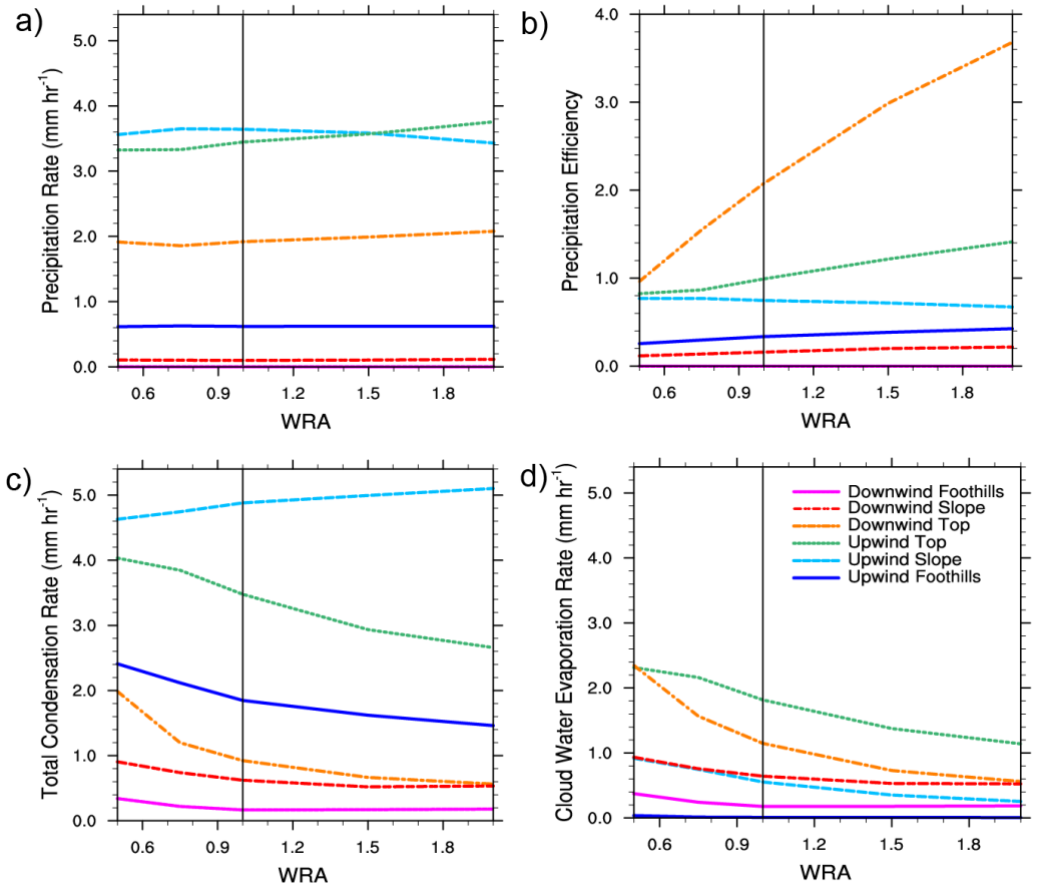

Figure 2.8 Cloud water accretion by rain (WRA) response functions for (a) precipitation rate (mm hr^{-1}), (b) precipitation efficiency (note: log axis), (c) vertically-integrated total condensation rate (mm hr^{-1}), and (d) vertically-integrated cloud water evaporation rate (mm hr^{-1}). Values are temporally-averaged over hours 6-20 and spatially averaged over the 6 regions shown in Fig. 2.3c. Black vertical lines depict the control parameter value.

Figure 2.9a,b shows temporally-averaged (hours 6-20) vertical cross-sections of cloud mixing ratios, vertical air motion, cloud condensation rate, and cloud evaporation rate for the simulations with the smallest and largest values of WRA. We see updrafts increase in magnitude over the upwind slope with increasing WRA (Figure 2.9b), which may be due to the reduction in condensate loading as more cloud water is effectively removed upwind. Stronger updrafts likely explain the 10% increase in <COND> over the upwind slope seen in Figure 2.8c. For the other

five regions, there is little change in vertical velocity for points containing liquid cloud, and the large decrease in <COND> with increasing WRA is primarily explained by an indirect effect of cloud water removal on the cloud base height (depicted here approximately by the 0.01 g kg^{-1} cloud mixing ratio contour in Figure 2.9). For small WRA, reduced conversion of cloud to rain means that more cloud water is available for evaporation in downdrafts compared to the simulations with large WRA. With more cloud water available, this implies a lowering of the cloud base and increasing vertical depth of the cloud layer, since the local evaporation rate calculated using saturation adjustment only depends on the pressure and tendencies of temperature (controlled mainly by the vertical velocity) and water vapor mixing ratio.

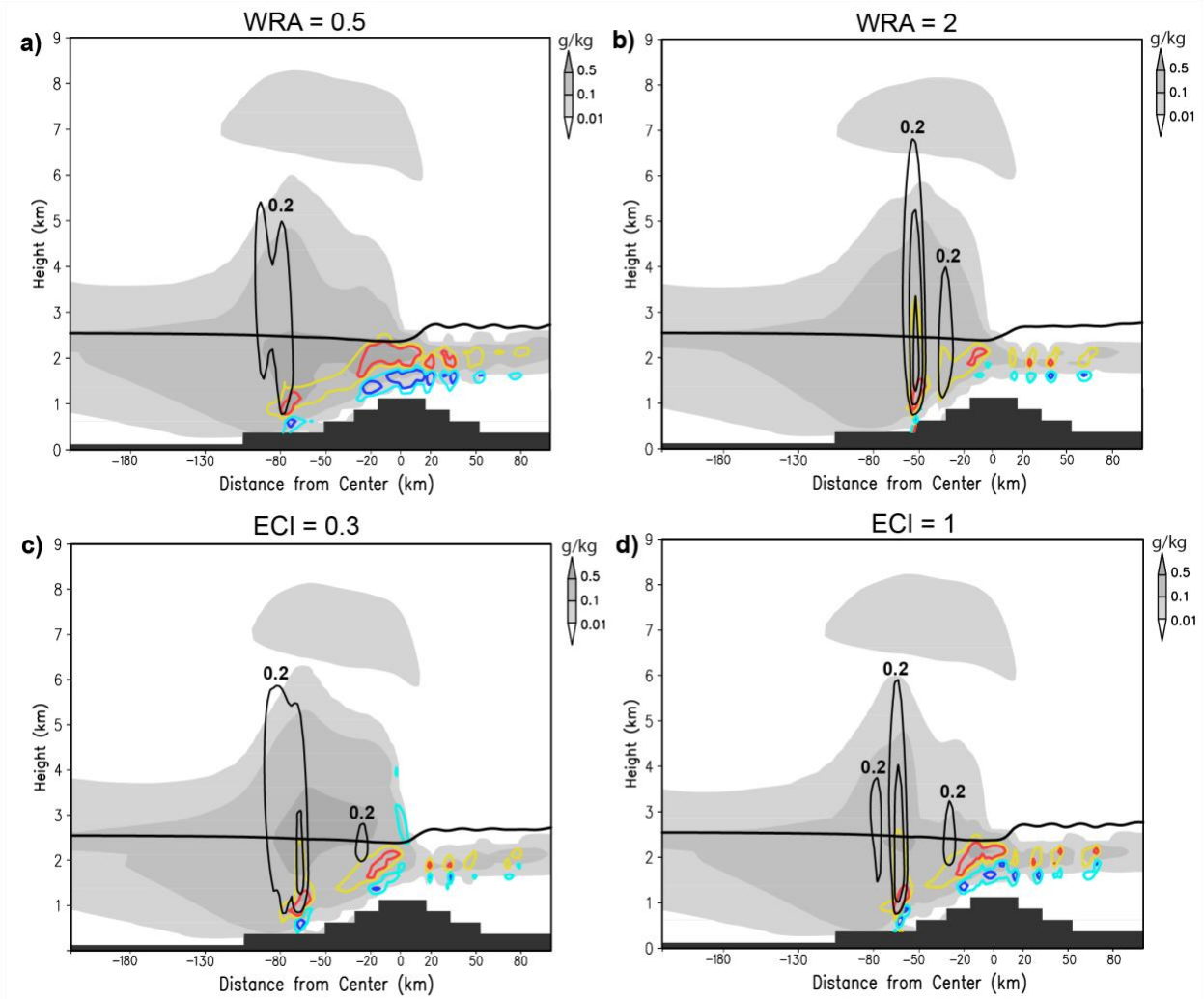

Figure 2.9 Vertical cross-sections over a portion of the domain of temporally-averaged (hours 6-20) cloud mixing ratio (cloud water and ice; g kg^{-1}), positive vertical wind speed (black contours at 0.1 m/s intervals starting at 0.2 m/s), cloud water condensation rate (red contours = $1x10^{-3}$ g kg^{-1} s^{-1}, yellow contours = $5x10^{-4}$ g kg^{-1} s^{-1}), cloud water evaporation rate (blue contours = $-1x10^{-3}$ g kg^{-1} s^{-1}, cyan contours = $-5x10^{-4}$ g kg^{-1} s^{-1}), and freezing level (thick black line). (a) WRA = 0.5, (b) WRA = 2, (c) ECI = 0.3, (d) ECI = 1.

This point can be illustrated clearly for moist pseudo-adiabatic descent; while the model has diabatic forcing due to mixing and other microphysical processes, moist pseudo-adiabatic descent can serve as a useful guide for explaining this behavior. For reversible moist pseudo-

adiabatic descent (and ascent), and assuming steady-state, we can write the change in cloud mass mixing ratio (q_c) with height (z) as $dq_c/dz = -dq_v/dz = -dq_s/dz$ above the cloud base, where q_v is the water vapor mixing ratio and q_s is the saturation mixing ratio that is a function only of temperature (T) and pressure (p). Since dq_s/dz only depends on T and p, dq_c/dz also depends only on T and p. Thus, if q_c near cloud top is relatively large due to a reduction of WRA, cloud parcels must descend further in order to completely evaporate all of the cloud water they contain, compared to the situation with relatively small q_c associated with an increase in WRA. Indeed, a lower cloud base and greater cloud depth are seen in the small WRA simulation compared to the large WRA simulation (compare Figure 2.8a,b). A lower cloud base in turn contributes directly to larger <COND> because the region of condensation extends over a greater depth. In addition to wider regions of condensation and evaporation associated with the lower cloud base, somewhat larger magnitudes of the condensation and evaporation rates occur for the small WRA simulation compared to the large WRA simulation (Figure 2.8d). Since the small WRA simulation has somewhat higher relative humidity consistent with the lower cloud base, this is likely attributable to the mixing of relatively moist air into updrafts, which limits the effects of entrainment in reducing the condensation rate compared to the large WRA simulation.

To briefly summarize, perturbations to WRA demonstrate the non-linear interactions between cloud water and surface precipitation. Reducing the rain accretion process initially reduces PE and precipitation rate and increases cloud water in the atmosphere, but the increased cloud water is associated with a deeper cloud layer (lower cloud base), leading to an increase in

<COND> that compensates for the decrease in PE. The opposite occurs for large WRA, thus resulting in little sensitivity of PREC to WRA.

ECI also acts to remove cloud water from the atmosphere, but through the riming process occurring at temperatures below freezing. The response functions for ECI clearly show the importance of the altitude at which cloud water is being removed since, unlike WRA, changes to ECI *do* result in a change in precipitation rate; as ECI is increased there is an increase of PREC over the upwind slope and decrease over the downwind top (Figure 2.10a). This is consistent with an increase in PE over the upwind slope and a decrease over the downwind top, but little change in <COND>. The decrease in PE upwind by lowering ECI is expected since it corresponds to a decrease of the conversion of cloud water to precipitation through riming. Figure 2.9c,d shows an impact on cloud water amount above the freezing level on the upwind top and slope as ECI is varied. Increased snow amounts with an increase in ECI and the fallout and subsequent melting of this snow leads to more precipitation on the upwind slope. The PREC and PE responses are similar to those for A_s (compare Figure 2.6a,b and Figure 2.10a,b). In contrast to WRA, perturbations to ECI result in little change in <COND> even though it also affects the efficiency of conversion from cloud to precipitation. This occurs because ECI has little effect on cloud water below the freezing level. The amount of cloud water in descending air near cloud base is relatively unaffected, leading to little impact on the cloud base height. Thus, cloud depth is relatively unaffected with perturbations to ECI, in contrast to WRA (compare Figure 2.9c,d with 2.9a,b); correspondingly there is little impact on overall evaporation and condensation rates whose magnitudes are much larger below the freezing level than above.

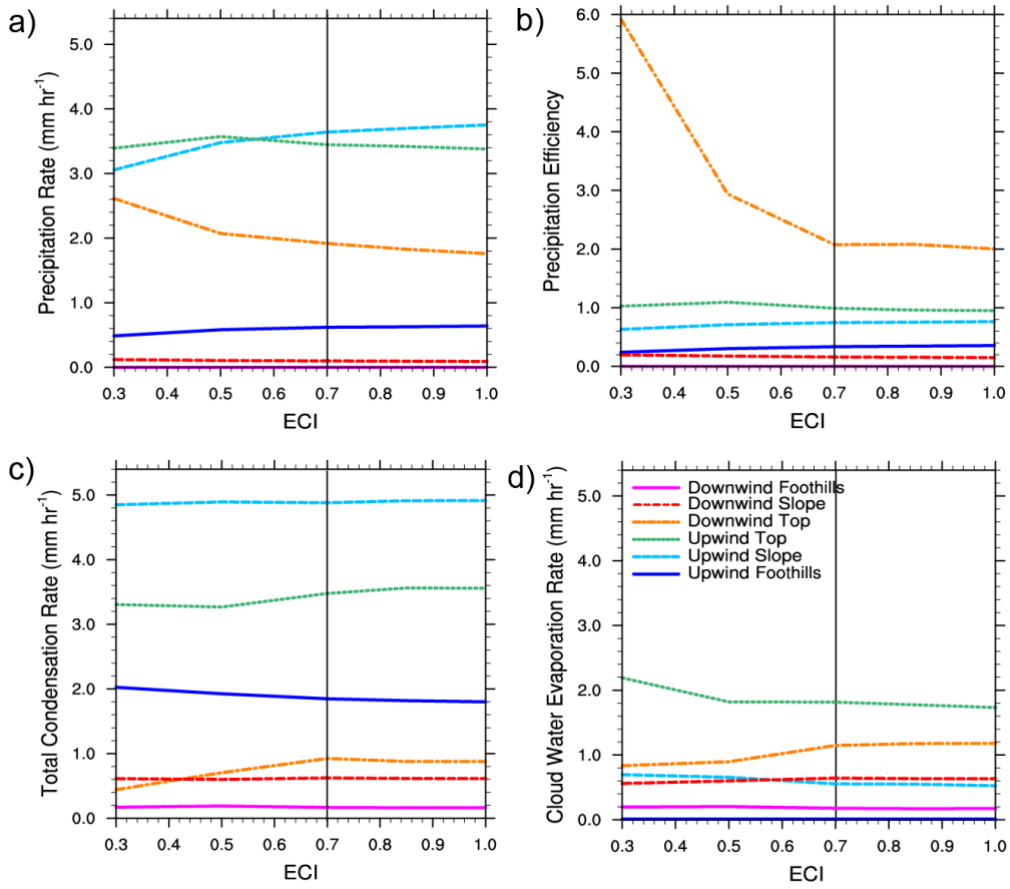

Figure 2.10 Same as Figure 2.8, but for ice-cloud water collection efficiency (ECI).

2.3.3 Environmental Experiments

Experiments were performed to test how the sensitivities to microphysical parameter changes compared to those in an environment where the wind profile is reduced by 30% (LowU) or the temperature is reduced to produce a freezing level that reaches below the mountain peak (LowFL). The LowU experiment contains the same amount of precipitable water compared to the control simulation, but the reduction in horizontal wind speed causes a reduction in the vertical velocities (near the ground, vertical velocities are proportional to mean horizontal wind

speed times mountain slope) resulting in a shallower cloud than in the control environment (Figure 2.11a). Precipitation rates for LowU are a factor of 3 less than in the control (Figure 2.11c), due to smaller <COND> and generally smaller PE (Figure 2.11d,e). Although the melting layer remains deep enough for warm-rain processes to remain active, the reduced cloud depth substantially reduces the contribution of ice processes to surface precipitation, as seen from the reduced development of snow in Fig. 2.11a. The highest total condensation and precipitation rates are shifted toward the upwind top in LowU compared to the control.

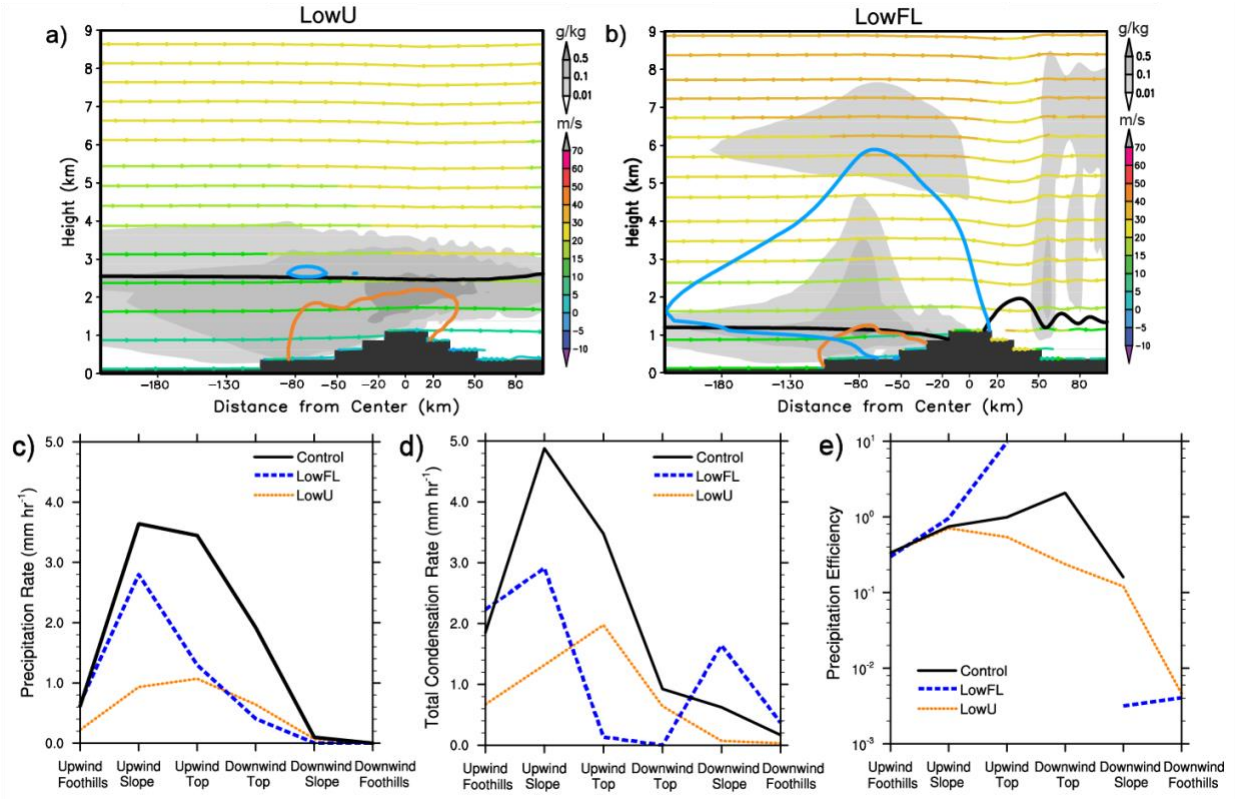

Figure 2.11 Top panels similar to Figure 2.3a, but for (a) LowU and (b) LowFL. Bottom panels are temporally-averaged (hours 6-20) and spatially-averaged (6 regions) values for (c) precipitation rate (mm hr^{-1}), (d) vertically-integrated total condensation rate (mm hr^{-1}), and (e)

precipitation efficiency. Solid black lines show values for the control simulation, dashed blue lines for the LowFL experiment, and dotted orange lines for the LowU experiment.

The LowFL experiment results in a deep cloud with a detached upper-level ice cloud, similar to the control (Figure 2.11b). In addition, high amplitude and frequency lee waves are triggered downstream once the freezing level descends below the mountain top (not shown). These lee waves form clouds over the downwind foothills and beyond. Although the precipitable water available in the LowFL environment is 11.7 cm less than for the control, the peak precipitation rate over the upwind slope is closer to that of the control than LowU (Figure 2.11c). This is because the condensate produced on the upwind slope is efficiently converted to precipitation (Figure 2.11d,e). A secondary peak in <COND> is located over the downwind slope, due to the lee waves previously mentioned, but because PE << 1 in this region little of this condensate makes it to the surface as precipitation. The reduction in freezing level allows for more cloud area to exist above the freezing level, thus increasing the potential for ice processes to dominate in this environment, as shown by the spatial reduction of rain in Figure 2.11b.

Overall, the LowU case results in a reduction in the magnitude of PREC responses to perturbations in A_s, ρ_s, ECI, and WRA than in the control environment (Figure 2.12 and Figure 2.13), mainly due to less condensate being available (Figure 2.11a,d, Figure 2.12c,f, and Figure 2.13c,f). Compared to the control simulation, WRA does have a minor effect on PREC in this case, with PREC increasing with WRA over the upwind slope/top and downwind top associated with a combination of large increases in PE and smaller decreases in <COND> (Figure 2.13). Additionally, PE responses to ECI are weaker in the LowU case compared to the control

simulation (Figure 2.13e). These responses are expected, as LowU results in weaker ascent, causing a reduction in the amount of cloud water available above the freezing level, thus allowing for warm-rain processes to dominate precipitation production. Although the ice processes play a smaller role in this case, the mechanisms controlling PE and <COND> are similar to those in the control environment: 1) changes in PE primarily explain the PREC responses to A_s and ρ_s perturbations (Figure 2.12), and 2) WRA affects <COND> through changes in the cloud base, while ECI does not (Figure 2.13).

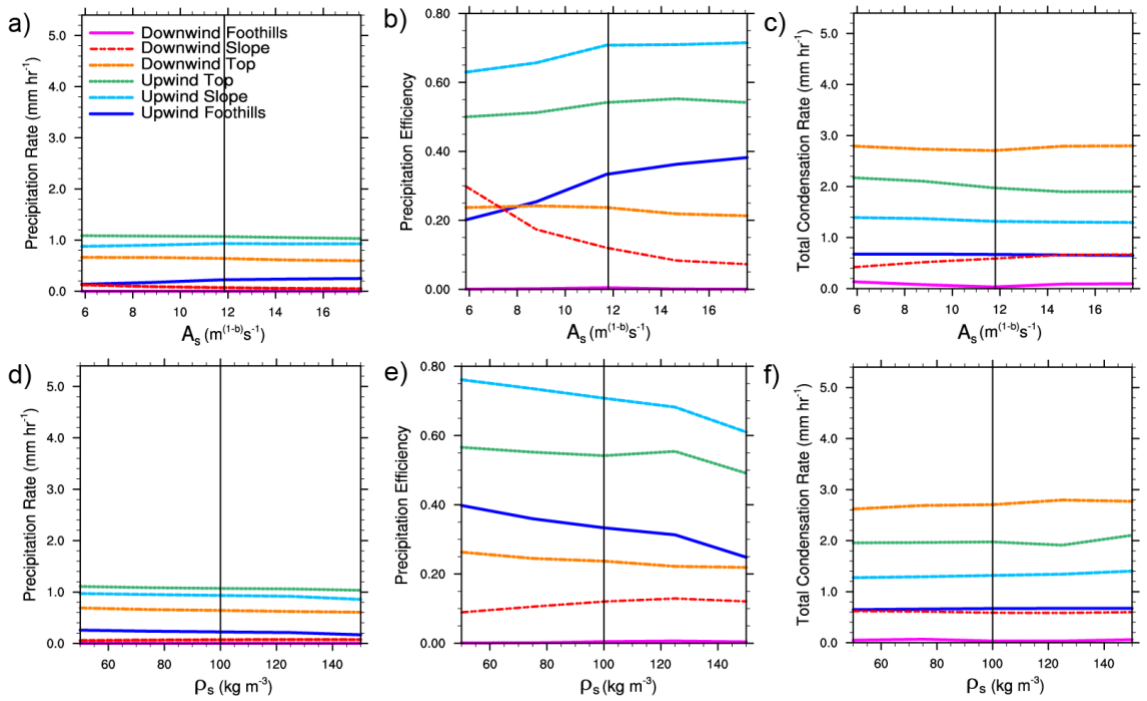

Figure 2.12 Snow fall speed coefficient (A_s, top panels) and snow particle density (ρ_s, bottom panels) response functions for precipitation rate (mm hr^{-1}, left panels), precipitation efficiency (middle panels), and vertically-integrated total condensation rate (mm hr^{-1}, right panels) for the LowU experiment. Black vertical lines depict the control parameter value.

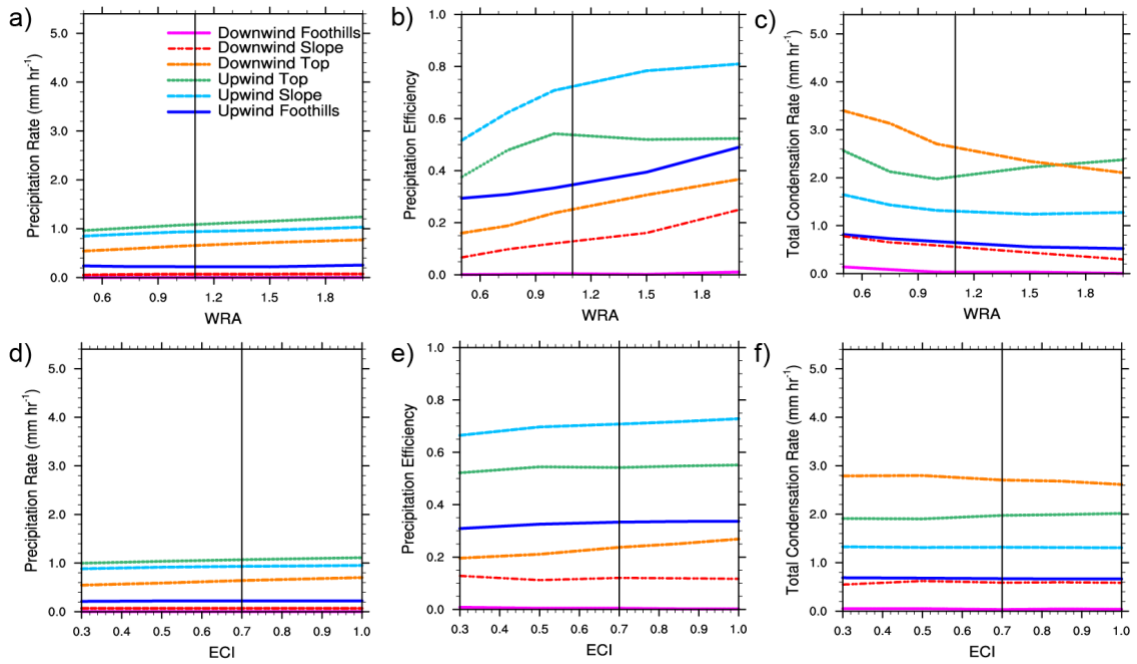

Figure 2.13 Similar to Figure 2.12, but for rain accretion (WRA, top panels) and ice-cloud water collection efficiency (ECI, bottom panels).

In contrast to the control environment and LowU environments, perturbations to A_s in the LowFL case produce notable impacts on <COND> (Figure 2.14). With a lower freezing level in the LowFL case, more of the cloud depth is present above the freezing level and thus, more cloud condensation occurs so that A_s has a noticeable effect on <COND> in addition to WRA (Figure 2.15c). Figure 2.16 illustrates this effect. Along the upwind slope the horizontal extent of cloud water above the freezing level increases as A_s is decreased, meaning that condensation extends over a wider region leading to greater <COND> on the upwind slope. The opposite occurs downwind, where <COND> increases as A_s is increased; this seems to be due to large A_s inducing higher amplitude lee waves compared to small A_s, resulting in more condensation downwind (Figure 2.16). As for WRA, the <COND> response functions are flatter than those in

the control simulation (Figure 2.15c); this is most likely due to a reduced impact of warm-rain processes on cloud and precipitation development because of the lower freezing level. For LowFL there is a minimal response of PREC, PE, and <COND> to changes in ρ_s (Figure 2.14d-f), and PREC to changes in ECI (Figure 2.15d), compared to the control simulation. These results reflect the complexity of precipitation sensitivities; although ice microphysical processes are generally expected to play a larger role in this case, this does not hold true for all of the associated parameter perturbations.

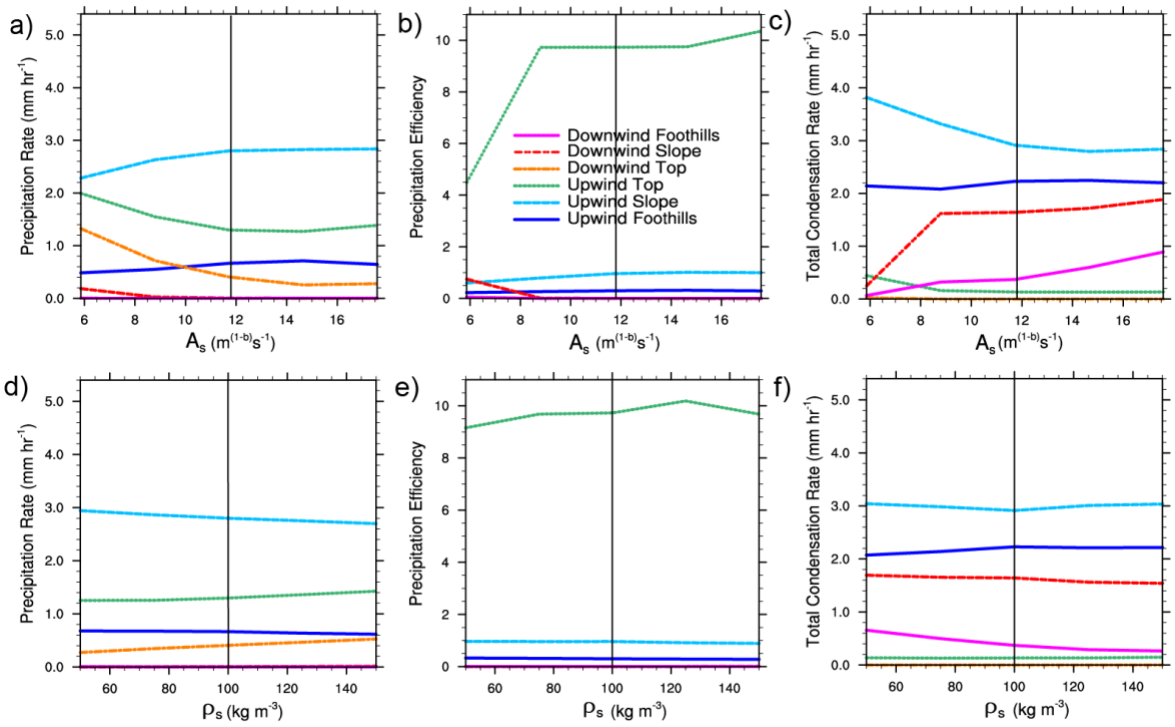

Figure 2.14 Similar to Figure 2.12, but for the LowFL experiment.

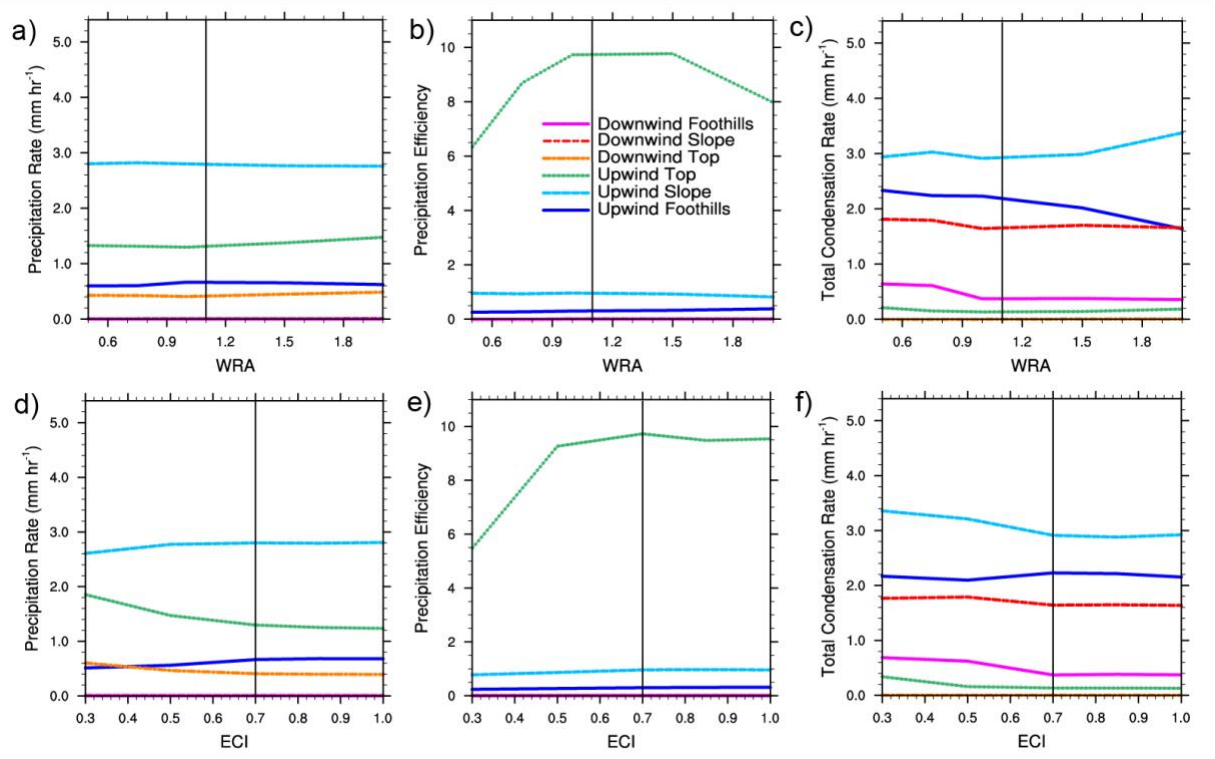

Figure 2.15 Similar to Figure 2.13, but for the LowFL experiment.

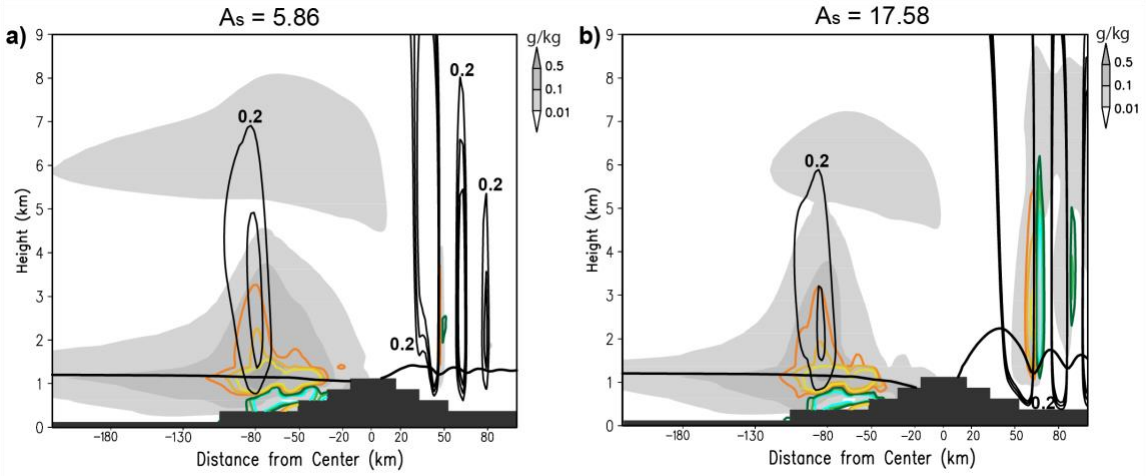

Figure 2.16 Similar to Figure 2.9, except with smaller values of cloud water condensation contours (dark orange contours = $2x10^{-4}$ g kg^{-1} s^{-1}, orange contours = $3.25x10^{-4}$ g kg^{-1} s^{-1}, yellow contours = $5x10^{-4}$ g kg^{-1} s^{-1}) and cloud water evaporation rate (dark green contours = $-2x10^{-3}$ g

$kg^{-1}\ s^{-1}$, green contours = $-3.25x10^{-4}$ g $kg^{-1}\ s^{-1}$, cyan contours = $-5x10^{-4}$ g $kg^{-1}\ s^{-1}$) for (a) $A_s = 5.86$ and (b) $A_s = 17.58$.

2.4 Summary and Conclusions

Idealized 2D simulations of moist nearly neutral flow over a bell-shaped mountain were performed using the CM1 model. The idealized upwind sounding was guided by observations from an atmospheric river event during the 2015 OLYMPEX field campaign. The objective of these simulations was to explore the sensitivity of orographic precipitation to changes in microphysical parameters, as well as testing the robustness of these results in different environments. Fifteen microphysical parameters associated with both ice and warm-rain processes within the Morrison microphysics scheme were perturbed over a range of values encompassing the uncertainty in these parameters. Two environmental sensitivity experiments were performed where the wind speed profile was reduced by 30% and the temperature was reduced enough to result in a freezing level below the mountain peak. These experiments allowed us to explore the precipitation sensitivity to microphysical parameters in environments where different precipitation processes were dominant.

Four parameters stood out as most influential to precipitation and cloud development: snow fall speed coefficient (A_s), snow particle density (ρ_s), rain accretion multiplicative factor (WRA), and ice-cloud water collection efficiency (ECI). A_s and ρ_s affect snow particle characteristics, while WRA and ECI are related to particle interaction (collection) processes. Precipitation rate responses to A_s and ρ_s perturbations are mainly a result of changes to precipitation efficiency (PE) through direct and indirect impacts, respectively, on snow fall

speed. This results in a location-dependent orographic precipitation sensitivity with an increase of windward precipitation and decrease downwind with an increase of A_s, with the opposite occurring as ρ_s is increased. Increasing WRA leads to greater removal of cloud water below the freezing level from conversion of cloud to precipitation and reduced <COND> caused by drying and raising of the cloud base height. Increased PE compensates the decrease in <COND> and results in little sensitivity on PREC. On the other hand, increasing ECI also removes cloud water from the atmosphere yet *does* cause changes to PREC. Increasing ECI results in a decrease in cloud water above the freezing level, but little effect on updraft speeds or <COND> below the freezing level, where the largest condensation rates occur. An increase in riming efficiency through large ECI results in responses similar to those for increasing A_s. In conclusion, we see that:

1) microphysics parameters which directly or indirectly impact snow fall speed induce a large sensitivity on the location of orographic precipitation and
2) perturbations to processes which affect the conversion of cloud water to precipitation will result in different sensitivities to cloud development, orographic precipitation, and thermodynamics-dynamics, depending on where the cloud water is affected in the vertical.

The environmental experiments showed that perturbing the upwind environment results in changes to the dynamics, which has consequences for the precipitation distribution and amount, as found in MR06 and T15. Compared to perturbations of the microphysical parameters,

the total amount of precipitation was more sensitive to environmental parameter perturbations. Overall, reducing wind speed had a strong effect on the amount of precipitation, while the changes in microphysical parameters in this environment had similar mechanisms responsible for changes in precipitation as in the control environment. However, because this case had much less condensate, the sensitivities were weaker. Lowering the freezing level through a reduction in the temperature profile resulted in A_s having an effect on <COND>, while PREC and PE were insensitive to ρ_s perturbations. Changes to the freezing level also had an effect on the overall location of maximum precipitation, shifting it upstream to where the freezing level was above the surface and warm-rain processes could aid in precipitation production. In general, our results show complex responses of microphysical parameter perturbations to precipitation for environments where different cloud processes dominate, i.e., warm-rain processes in LowU and ice processes in LowFL.

These results highlight the complexity of the orographic precipitation response to microphysical parameter changes, leading us to the following questions: 1) will changing various parameters simultaneously modify the precipitation response? 2) how do simultaneous changes to microphysical, environmental, and mountain shape parameters affect the orographic precipitation sensitivity? To answer these questions, chapter 3 presents results from multivariate perturbations using the parameters tested in this study as well as additional environmental parameters.

Chapter 3. Orographic Precipitation Sensitivity Analysis using the Morris One-at-a-Time Method (Morales et al. 2019)

3.1 Introduction

Microphysical parameterizations represent cloud and precipitation processes within numerical weather prediction models used in operational forecasting and research. All schemes contain parameters whose values are known to naturally vary in space and time, yet are typically held constant, e.g., snow particle density. These parameter values also have a range of uncertainty due to limited observations and measuring capabilities, or because the parameter may not have a physical equivalent in nature, e.g., autoconversion thresholds. Changes in these parameters have been shown to affect cloud development, as well as precipitation distribution and timing over mountains (e.g., Colle et al. 2005; Jankov et al. 2007, 2009; Liu et al. 2011). For example, reducing the snow particle fallspeed, or the degree of riming, can shift maximum precipitation from the windward to lee side of a mountain (Hobbs et al. 1973; Colle and Mass 2000; Lin and Colle 2009, 2011; Morrison et al. 2015; Morales et al. 2018 (hereafter M18)). Communities worldwide depend on orographic precipitation for their freshwater resources, thus it is of utmost importance to understand how uncertainty in microphysical parameters may impact where and how much precipitation is forecast to occur.

Colle (2004) was one of the first studies to rigorously explore the sensitivity of orographic precipitation to changes in ambient conditions and mountain geometry. Performing hundreds of two-dimensional (2D) idealized simulations, the study showed the spatial

distribution of precipitation was dependent on the flow regime and gravity wave evolution caused by changes to horizontal wind speed and direction. Through the numerous combinations of individual parameter perturbations, this study demonstrated the complex relationships between microphysics, dynamics, and environmental conditions. For example, melting of snow and graupel can lower the freezing level upwind of a mountain range more for a wider and higher barrier in a moderate wind speed environment (Colle 2004). Additionally, precipitation distribution response to wind speed changes can vary depending on the height of the freezing level, i.e., lower freezing level can result in decreased upwind precipitation efficiency with increasing wind speed, as faster flow favors the leeside advection of ice (Colle 2004). For a higher freezing level, more efficient warm-rain processes would increase precipitation over the windward slope as less precipitation is advected leeward (Colle 2004; M18).

Motivated by previous studies attributing poor precipitation forecasts to microphysics representation in mesoscale models, Colle and Zeng (2004a) varied parameters within a bulk scheme for an idealized simulation of a 1986 Sierra Nevada precipitation event. They found precipitation to be most sensitive to snow and graupel fall velocities, snow size distribution intercept parameter, and cloud condensation nuclei concentration. A subsequent study by Colle and Zeng (2004b) varied barrier width and freezing levels in addition to microphysical parameters. They found orographic precipitation over wide mountains was most sensitive to snow fall velocity owing to increased time for snow growth before reaching the surface (Colle and Zeng 2004b). Additionally, precipitation sensitivity to microphysics varied for different freezing levels due to different processes being activated. Although an increase in surface

temperature led to an increase in available precipitable water, there was a nonlinear effect on precipitation due to different microphysical processes activating at different temperatures and a decrease in the depth over which ice processes occur, resulting in reduced precipitation contribution from melting (Miglietta and Rotunno 2006; Kirshbaum and Smith 2008; M18). Orographic precipitation location and amount can be affected by changes to static stability, wind speed, and mountain height through changes in updraft strength, flow characteristics, and gravity wave dynamics (Durran 1990; Colle 2004; Kunz and Kottmeier 2006; Kunz and Wassermann 2011).

More recently, Tushaus et al. (2015) performed a multivariate sensitivity analysis using Bayesian methods to determine the impact of upwind environment and mountain geometry to orographic precipitation. Their results showed non-unique responses of precipitation rate to changes in mountain half-width, Brunt-Väisälä frequency, and horizontal wind speed values, as well as showing multiple combinations of parameters can result in the same precipitation amount and distribution. Tushaus et al. (2015) did not include ice microphysical processes in their study, which are influential to precipitation development and intensity (Castellano et al. 2004; Colle et al. 2005; Purdy et al. 2005; Minder et al. 2008). Ice microphysics adds considerable complexity owing to the numerous processes for ice growth, and the wide variety of ice types and crystal habits. Thus, M18 expanded on previous work by including ice microphysics while testing the effects of microphysical parameter perturbations on orographic precipitation. Their idealized simulations found four dominant parameters were responsible for the largest changes in precipitation rate and liquid and ice water paths: snow fallspeed coefficient, snow particle

density, rain accretion, and ice-snow collection efficiency. Overall, M18 found changes to environmental parameters (i.e., wind speed and surface temperature) were largely responsible for the total amount of available condensate for the microphysics to act upon, and affected which microphysical processes were dominant (i.e., warm-rain versus ice).

These previous studies suggest complex relationships between microphysics and the upstream environment, i.e., microphysical parameter sensitivities can change with different environments, perturbations to environmental conditions can result in non-linear responses, etc. However, most model parameter sensitivity studies on orographic precipitation perturb one parameter at a time while holding the rest constant, also known as having a constant "base state". This method for sensitivity analysis is inherently limited, and if relationships among parameters are nonlinear, may result in incomplete conclusions. On the other hand, quantifying multi-parameter sensitivity is challenging because the number of simulations required is equal to M^N, where M is the number of values tested per parameter and N is the number of parameters. As microphysical parameterizations have become more complex, the number of "tunable" parameters have increased. Thus, brute-force calculation of multi-parameter sensitivity in the large-dimensional parameter space is not generally computationally feasible.

To address this problem, we employ the Morris one-at-a-time (MOAT) method, which explores interactions between parameters through multivariate parameter perturbations (Morris 1991; Campolongo et al. 2007). MOAT can test a large number of parameter combinations and isolate the influences of individual parameters on model output (Saltelli et al. 2008). This statistically robust method has been widely used for hydrologic model sensitivity analysis (King

and Perera 2013; Shin et al. 2013; Yang et al. 2014; Song et al. 2015) but has been infrequently applied to atmospheric science. Covey et al. (2013) introduced this method to the climate science community in a study that explored the sensitivity of outgoing longwave and shortwave radiation to various climate model input parameters in the Community Atmospheric Model; while Zhang et al. (2015) used MOAT for parameter sensitivity analysis in the Grid-point Atmospheric Model. Most recently, Zarcycki and Ullrich (2017) applied MOAT to investigate the sensitivity of "objectively tracked output metrics", e.g., accumulated cyclone energy and false alarm rate, in climate model data to various tropical cyclone tracking algorithm parameters. To our knowledge, the study described herein is the first to use MOAT to analyze simulations of orographic precipitation.

Our study focuses on understanding simulated precipitation sensitivities for moist, nearly neutral flow over a 2D bell-shaped mountain. This type of flow is commonly found within wintertime atmospheric rivers (ARs) off the Western US Coast and allows for little resistance to orographic lift, causing enhanced precipitation over windward mountain slopes (Lin et al. 2001; Ralph et al. 2004, 2005; Nieman et al. 2011; Ralph and Dettinger 2011). This AR-produced precipitation is responsible for up to 50% of California's annual precipitation (Dettinger et al. 2011) and can lead to flash floods and landslides (Ralph et al. 2006).

Given the importance of both microphysics and environmental conditions to orographic precipitation, this study explores the following science questions:

- Which microphysical parameters are most influential to orographic precipitation when multi-parameter interactions are allowed?

- How are microphysical parameter sensitivities changed when environmental parameters are perturbed simultaneously for a given environmental state?
- Are the effects from microphysical parameter perturbations larger than the effects of environmental parameter uncertainty?
- How does the influence of microphysical parameter perturbations change when different environments are imposed?
- Are the effects from microphysical parameter perturbations in a single scheme larger than the effects caused by using different microphysical schemes?

We hypothesize that both microphysical and environmental parameters will be important; that is, perturbations to microphysical parameters will cause a change in the model output comparable to that from small perturbations to the environmental state, over ranges of parameter uncertainty for both. We also expect that sensitivity to microphysical parameter perturbations will vary depending on the environmental state, regardless of multi-parameter perturbations allowed in MOAT, since changes to environmental conditions have been shown to be responsible for the total amount of condensate produced (M18).

3.2 Methodology

3.2.1 Model Configuration

All experiments are performed using version 17 of CM1, a non-hydrostatic numerical model often used for idealized simulations of cloud-scale processes (Bryan and Fritsch 2002). The model configuration follows that of M18, thus only a brief summary will be provided here.

A two-dimensional (2D) domain 1600 km in length is used. The inner domain is 1200 km in length, spanning over 600 grid points, with a horizontal grid spacing of 2 km that stretches to 6 km over 50 grid points on each side. The mountain center is shifted 400 km downstream to limit the reflection of waves from the upwind boundary. Total domain height is 18 km with 55 vertical levels. The vertical grid spacing (Δz) is 0.25 km below a height of 9 km, and stretches to 0.5 km up to 10.5 km, after which Δz remains constant at 0.5 km. Lateral boundaries are open-radiative and the bottom boundary condition is no-slip. Radiation, surface fluxes, and Coriolis acceleration are neglected. Simulations are run for 20 hours using a 3 sec time step. A Gaussian bell-shaped mountain with a 2 km height and 40 km half-width is used. Note, the mountain height used here is twice the size of that used in M18. These mountain shape parameters are characteristic of the Sierra Nevada and Cascade mountains, which have been idealized as 2D ridges in previous studies (e.g., Colle and Zeng 2004a,b; Colle 2004; Kirshbaum and Smith 2008). Limitations do exist when using a 2D domain, for example over-amplification of mountain waves due to energy dispersion limited to one direction, unrealistic mountain profiles, and reduced deflection of low-level flow. However, a 2D model configuration is applied as it

simplifies the number of parameters controlling the upstream flow, allowing for a more controlled set of experiments. We thus follow past studies which have applied a 2D domain to study mountain flow dynamics and orographic precipitation (e.g., Doyle et al. 2000; Colle 2004; Colle and Zeng 2004; Miglietta and Rotunno 2005, 2006; Tushaus et al. 2015; M18).

The idealized control sounding and wind speed profile (Figure 3.1) is the same as in M18, and closely corresponds to conditions observed during atmospheric river events for OLYMPEX (Houze et al., 2017) and other field campaigns (e.g., Ralph et al. 2005). The atmospheric profile is described by the following default values: a surface potential temperature (θ_{sfc}) of 286 K; surface u-wind speed (U) of 14 m s^{-1}, linearly increasing to 42 m s^{-1} at a height of 12km, then remaining constant at 42 m s^{-1} above 12 km; relative humidity (RH) below 4.5 km of 95%, then linearly decreasing to 20% at a height of 16 km, and remaining constant above 16 km; and a moist Brunt-Väisälä frequency (N_m^2) for the troposphere and stratosphere of $4x10^{-5}$ s^{-2} and $5x10^{-4}$ s^{-2}, respectively.

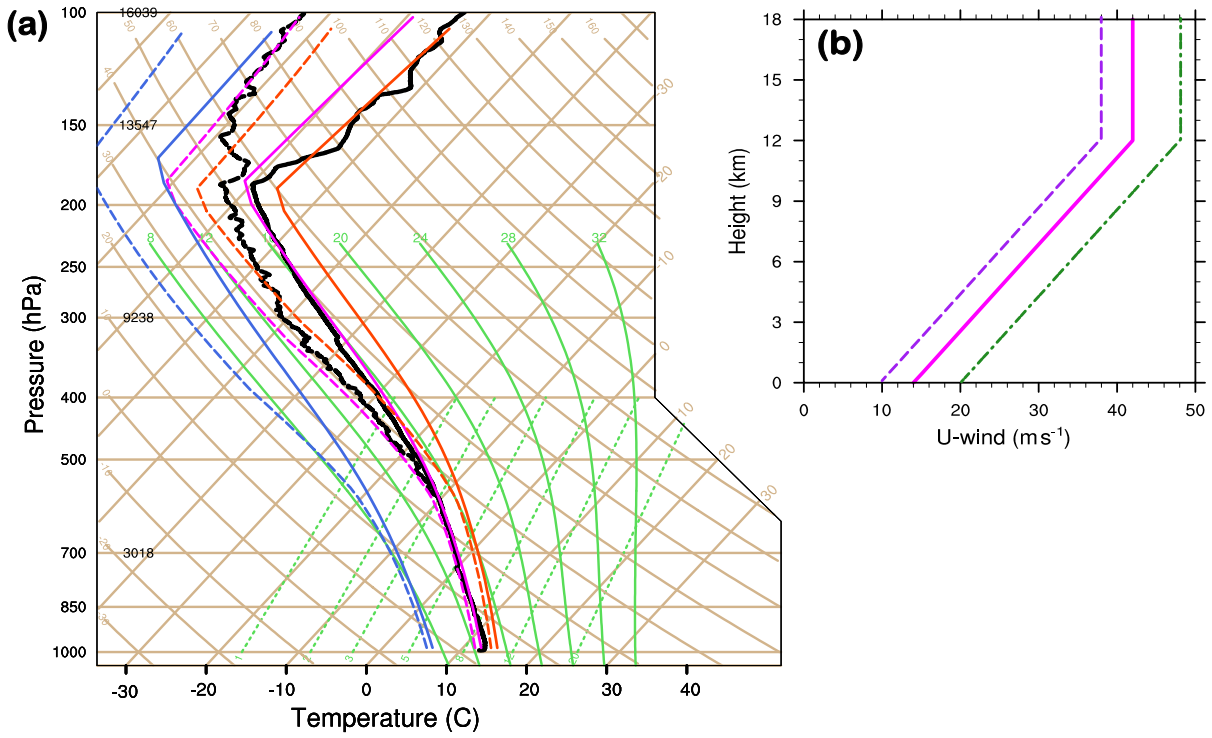

Figure 3.1 a) Skew-T diagram showing the observed sounding from OLYMPEX 0300 UTC 13 NOV 2015 (black), idealized sounding (magenta), MP_COLD sounding (blue), and MP_WARM sounding (orange). For all soundings, solid lines represent temperature and dashed lines represent dewpoint temperature, all in degrees Celsius. (b) Vertical profile of zonal wind speed (m s^{-1}) showing the idealized profile (solid magenta), MP_SLOW profile (dashed purple), and MP_FAST profile (dot-dashed green).

3.2.2 Microphysical and Environmental Parameters

The Morrison two-moment microphysics scheme version 3.4 (Morrison et al. 2005; 2009) is used, with the rimed ice species set to graupel. Microphysical parameters and their uncertainty ranges are the same as those listed in M18. The microphysical parameters examined focus on prescribed parameters for frozen condensate, conversion thresholds, collection efficiencies, and ice processes within the Morrison scheme (Table 3.1). Because there are few

prescribed parameters for warm-rain processes, we apply a multiplicative factor for rain accretion and autoconversion. The range of values used to perturb the parameters is based on our estimate of uncertainty and variability for each microphysical parameter. As described in the introduction, previous studies have found θ_{sfc}, RH, tropospheric N_m^2, and U impact orographic cloud and precipitation development through condensate production and advection, freezing level effects, and changes to the vertical velocities. To understand the influence of environmental parameter perturbations on microphysical parameter sensitivities, and compare the effects on precipitation when both groups of parameters are perturbed, we use a range of values consistent with the relative uncertainty of observations. For example, we assume the average uncertainty for θ_{sfc} in a sounding is 1 K, thus our uncertainty range is +/- 1 K from the default surface potential temperature of 286 K (Table 3.1). The RH, N_m^2, and U parameters are perturbed using "additive factors", which act to increase/decrease the value for that parameter in the module. To determine the N_m^2 change for a potential temperature perturbation of 1 K, equation 36 from Durran and Klemp (1982) is used to calculate a range of uncertainty +/- 2.5×10^{-6} s^{-2} from the default tropospheric moist Brunt-Väisälä frequency. The additive factors for U and RH act to shift the wind speed and relative humidity profiles, respectively, to higher or lower values. The additive factor for wind speed is given a typical uncertainty range for a sounding of +/- 1 m s^{-1}, thus the control wind profile is perturbed within this narrow range of values. Lastly, the additive factor for RH is assumed to have an uncertainty of +/- 10% for a sounding. Because the control profile has a surface RH at 95% and the profile below 16 km depends on the surface RH value, this region has an uncertainty range between -10% and 5%.

Above a height of 16 km it is allowed to increase up to 10%. Thus, the range of RH values in our sensitivity tests is 85-100% below 4.5 km, and 10-30% above 16 km.

Analysis of precipitation rate, total condensation rate, and precipitation efficiency is performed using 5-minute model output temporally-averaged between hours 6-20, during which the cross-mountain flow, precipitation rate, and cloud and hydrometeor development are relatively steady (Figure 3.2). We spatially average model output over six locations on the mountain: upwind foothills (UF), slope (US), and top (UT) and downwind foothills (DF), slope (DS), and top (DT) (Figure 3.2c). Total condensation rate (<COND>, mm hr^{-1}) is a vertical integral of all process rates that convert water vapor to condensate, and is subsequently horizontally-averaged over the six mountain regions (M18). Precipitation efficiency (PE) is calculated as PE = PREC/<COND>, where PREC is the horizontally-averaged total (liquid + frozen) precipitation rate over the six regions, and quantifies the fraction of condensate removed through microphysical processes (evaporation and sublimation) and sedimentation. PE can also be affected by horizontal transport of condensate because of the spatial averaging performed over limited regions of the domain. This analysis provides information on whether a parameter's influence on PREC is due to that parameter effecting dynamical-thermodynamical processes (<COND>) and/or microphysical processes and sedimentation (PE).

Table 3.1 Input parameters varied in MOAT experiments

j	Parameter Description (Symbol)	Uncertainty Range
1	Cloud ice fallspeed coefficient (A_i)	700 $m^{(1-b)}$ s^{-1} +/- 50%
2	Snow fallspeed coefficient (A_s)	11.72 $m^{(1-b)}$ s^{-1} +/- 50%

3	Graupel fallspeed coefficient (A_g)	19.3 $m^{(1-b)}$ s^{-1} +/- 50%
4	Cloud ice density (ρ_i)	500 kg m^{-3} +/- 50%
5	Snow density (ρ_s)	100 kg m^{-3} +/- 50%
6	Graupel density (ρ_g)	400 kg m^{-3} +/- 50%
7	Cloud ice autoconversion threshold (DCS)	125 μm +/- 50%
8	Nucleated ice crystal radius (RMI0)	1–30 μm
9	Embryo graupel radius (RMG0)	35–1000 μm
10	Ice-Ice collection efficiency (EII)	0.01–1
11	Ice-cloud water collection efficiency (ECI)	0.3–1
12	Radius of splintered ice particle (RMMULT)	1–30 μm
13	Rain accretion multiplicative factor (WRA)	0.5–2
14	Cloud water autoconversion multiplicative factor (WRC)	0.1–10
15	Snow deposition multiplicative factor (SDEP)	0.5–2
16	Relative humidity profile additive factor (RH)	+/- 10%
17	U-wind speed profile additive factor (U)	+/- 1 m s^{-1}
18	Surface potential temperature (θ_{sfc})	285 K–287 K
19	Tropospheric moist Brunt-Väisälä frequency additive factor (N_m^2)	+/- 2.5x10^{-6} s^{-2}

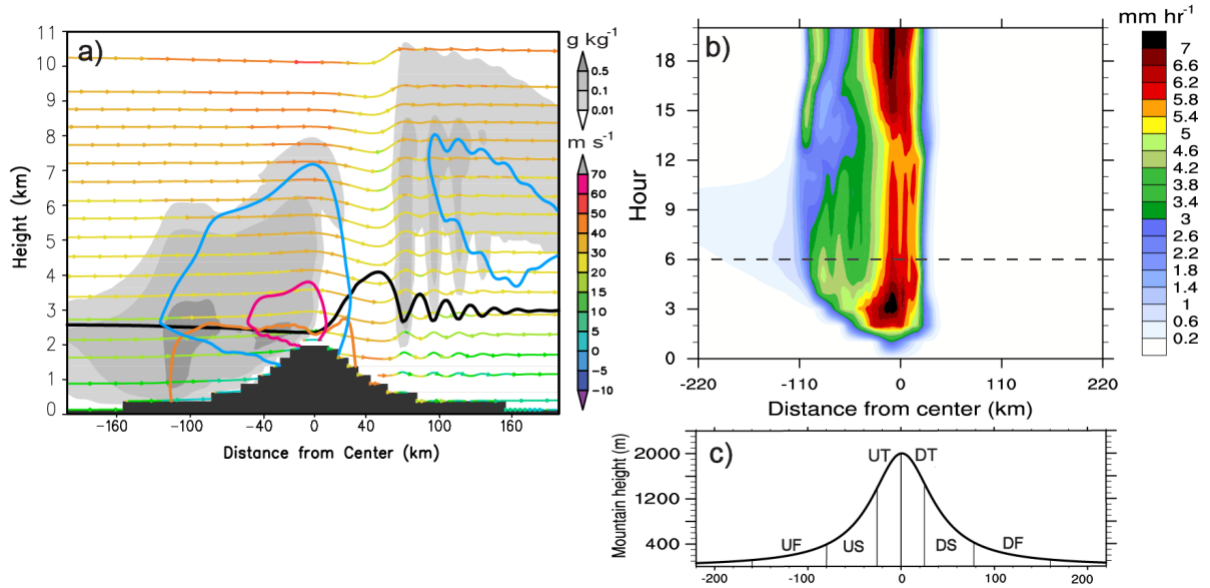

Figure 3.2 (a) Vertical cross-section showing temporally averaged (hours 6-20) streamlines colored with wind speed (m s^{-1}), freezing level (black line), cloud water and ice mixing ratios (gray shaded contours, g kg^{-1}), and 0.05 g kg^{-1} mixing ratio contours for snow (blue), rain (orange), graupel (magenta) for the control simulation over a portion of the domain. (b) Hövmöller diagram of precipitation rate (mm hr^{-1}) with simulation time on the ordinate and distance from center of the mountain on the abscissa. The dashed gray line corresponds to hour 6, the start of temporal averaging. (c) Mountain height (m) profile with the six averaging regions used for the calculations: upwind foothills (UF), slope (US), top (UT), and downwind top (DT), slope (DS), and foothills (DF).

3.2.3 Experimental Design

The Morris one-at-a-time (MOAT) method is used to determine which subset of microphysical and environmental parameters results in the largest changes to surface precipitation. To understand how simultaneously perturbing microphysical and environmental parameters impacts precipitation sensitivities, experiment "MP_ENV" is performed and compared to "MultiParam", which perturbs multiple microphysical parameters using MOAT while keeping the environment constant (Table 3.2). It is known that upstream conditions can

vary the precipitation sensitivity to microphysical parameter perturbations (Colle and Zeng 2004b; Miglietta and Rotunno 2006; M18), thus we perform a second set of experiments to test if these previous findings still hold when multi-parameter perturbations are included using MOAT. We expand on M18 and test four environments corresponding to a colder (MP_COLD), warmer (MP_WARM), slower wind speed (MP_SLOW), or faster wind speed (MP_FAST) environment.

Table 3.2 List of experiments

Experiment	**Description**	**Purpose**
MultiParam	Multiple microphysical parameters perturbed using MOAT. Environmental parameters held constant at default values.	Building on Morales et al. (2018) by allowing for multi-parameter interactions using MOAT
MP_ENV	Microphysical and environmental parameters perturbed simultaneously using MOAT.	Testing the influence of microphysics versus environment
MP_COLD	Multiple microphysical parameters perturbed using MOAT. Surface potential temperature default value decreased by 6 K (θ_{sfc} = 280K).	Testing microphysical parameter sensitivities in a low freezing level environment
MP_WARM	Multiple microphysical parameters perturbed using MOAT. Surface potential temperature default value increased by 2 K (θ_{sfc} = 288K).	Testing microphysical parameter sensitivities in a higher freezing level environment
MP_SLOW	Multiple microphysical parameters perturbed using MOAT. Zonal wind speed profile decreased by 4 m s^{-1} (U_{sfc} = 10 m s^{-1}).	Testing microphysical parameter sensitivities in an environment with weaker dynamics
MP_FAST	Multiple microphysical parameters perturbed using MOAT. Zonal wind speed profile increased by 6 m s^{-1} (U_{sfc} = 20 m s^{-1}).	Testing microphysical parameter sensitivities in an environment with stronger dynamics

MultiPhys	An "ensemble" (4 simulations total) using different microphysical schemes (Morrison two-moment, Thompson, NSSL two-moment, and NASA-Goddard LFO). No changes to default environmental or microphysical parameters in any schemes.	Comparing the influence of using different schemes to parameter perturbations within a single scheme

MP_COLD decreases the control temperature profile by 6 K (θ_{sfc} = 280 K; Figure 3.1a), thus simulating an environment where much of the upwind slope and mountain top are above the freezing level and upon which most precipitation falls as snow. This case should exhibit greater dominance of ice processes, since a larger amount of the cloud occurs above the 0°C level, and there will be less available precipitable water owing to the decrease in temperature. MP_WARM increases the control temperature profile by 2 K (θ_{sfc} = 288 K; Figure 3.1a) and thus has a deeper melting layer where warm-rain processes dominate and a larger fraction of the precipitation falls as rain. Because RH is held constant, increased water vapor content due to increased temperatures is expected to increase total precipitation. MP_SLOW decreases the wind speed profile by 4 m s^{-1}, resulting in a surface wind speed of 10 m s^{-1} (Figure 3.1b). MP_FAST increases the wind speed profile by 6 m s^{-1}, resulting in a surface wind speed of 20 m s^{-1} (Figure 3.1b). This case acts to simulate a low-level jet, which has been observed below 2 km MSL during AR events (Ralph et al. 2005), impinging on the barrier. Given a strong cross-barrier flow, we expect more downwind transport as well as more condensation upwind caused by stronger vertical velocities relative to the control environment.

Finally, experiments are performed in which the entire microphysics scheme is changed rather than individual parameters within a single scheme (MultiPhys) to compare the sensitivity

of surface precipitation to different microphysics schemes. In addition to the Morrison two-moment scheme used for the MOAT experiments, the Thompson (Thompson et al. 2008), NASA-Goddard LFO (Gilmore et al. 2004), and NSSL two-moment (Ziegler 1985; Mansell et al. 2010; Mansell 2010) schemes are used for the "ensemble" used in MultiPhys. The same four schemes are tested with the upstream soundings used for MP_COLD, MP_WARM, MP_SLOW, and MP_FAST to account for possible sensitivity to the environment. A summary of all the experiments is listed in Table 3.2.

3.2.4 Morris one-at-a-time (MOAT) Method

As described in Section 3.1, previous studies have performed sensitivity analysis on microphysical and environmental parameters by perturbing each parameter of interest individually while holding the rest constant, i.e., a "constant base state". This type of single parameter perturbation may miss interactions with other parameters. Therefore, the MOAT method, also known as the Morris screening or Elementary Effects method, is used to determine the input factors that have the largest influence on the model output when considering multivariate parameter perturbations (Morris 1991; Campolongo et al. 2007).

MOAT allows for simultaneous testing of a large number of input parameters while being computationally affordable, i.e., $M(N+1)$ simulations are required for N input parameters and M trajectories or paths, compared to M^N for a standard multi-parameter sensitivity analysis. Although MOAT allows for nonlinearity and interaction effects, is computational efficient, and its results are straightforward to understand, this method only provides a qualitative sensitivity analysis. For example, while it can be used to rank the influence of parameters and determine

whether there is nonlinearity in the input – output relationship, it cannot be used to compute the fraction of the variance in model output explained by each parameter, or combinations of multiple parameters. For a quantitative analysis that can provide deeper understanding of nonlinear parameter interactions and determine individual parameters' contribution to the output variance, more computationally expensive variance-based methods must be applied (Saltelli et al. 2008). MOAT is commonly used as a first step toward variance-based analysis, as it identifies which parameters are influential, allowing a smaller subset to be explored using more computationally expensive methods.

MOAT provides a sensitivity analysis by perturbing individual input parameters with respect to different parameter base states. The values for each input parameter are randomly chosen from a range of values encompassing the parameter uncertainty and/or variability (see Table 3.1). For a set of parameters $X = x_1, x_2, \dots, x_N$ the "elementary effect" of the j[th] parameter is defined as:

$$d_j = \frac{y(x_1,\dots,x_j+\Delta,\dots,x_N)-y(x_1,\dots,x_j,\dots,x_N)}{\Delta}\ , \qquad (3.1)$$

where y represents the model output and Δ represents a small, discrete change in the value of parameter *j* relative to the range. These variables are normalized to a range of [0,1] before each initial parameter set is generated, to avoid issues comparing parameters with different units. The elementary effect basically calculates the change in the model output, i.e., surface precipitation rate, given a change in the input parameter. This process is repeated for *M* paths within the parameter space, where each path uses a different randomly generated base state. Here we apply

the algorithm M = 20 times, resulting in a total of 320 simulations for 15 parameters (e.g., MultiParam) and 400 simulations for 19 parameters (e.g., MP_ENV). Tests showed the results for this study generally converge after M = 15, thus we believe 20 MOAT paths is sufficient as suggested by Covey et al. (2013). From this distribution of elementary effects, the mean of the absolute value of the elementary effects, $\mu_j{}^*$(Campolongo et al. 2007), and the standard deviation of the elementary effects, σ_j, are calculated as follows:

$$\mu_j{}^* = \frac{1}{M}\sum_{i=1}^{M}\left|d_{i,j}\right|, \tag{3.2}$$

$$\sigma_j = \sqrt{\frac{1}{M}\sum_{i=1}^{M}(d_{i,j} - \frac{1}{M}\sum_{i=1}^{M} d_{i,j})^2}, \tag{3.3}$$

The average influence of the input parameter on the model output is given by $\mu_j{}^*$ and the nonlinearity is determined by σ_j. If $\mu_j{}^*$ is large, this means the input parameter caused a large change in the model output, i.e., it is an influential/important parameter. If σ_j is large, or large relative to its corresponding $\mu_j{}^*$, this means a perturbation to the input parameter resulted in a large variety of output values caused by nonlinear interactions with other parameters or a nonlinear individual response. Parameters with low $\mu_j{}^*$ and σ_j are non-influential, implying they could be set to a constant value in the model. These two sensitivity measures can be further used to rank the most influential parameters (high to low $\mu_j{}^*$), as well as calculate sensitivity characteristics like monotonicity of the response. In the following section, we use fractional sensitivity (FS) to understand the influence of the input parameters on precipitation rate over the six averaging regions of the domain. FS normalizes $\mu_j{}^*$ by the model output range (y_{max} - y_{min}) to

compare the variation caused by individual parameters to the variation generated from all the one-at-a-time simulations (Equation 3.4):

$$FS = \frac{\mu_j^*}{y_{max} - y_{min}} \times 100 \qquad (3.4)$$

For a more detailed description of MOAT and a step-by-step example of how the algorithm is applied, see Section 3.2 in Covey et al. (2013).

3.3 Results and Discussion

3.3.1 Control Simulation

Temporally-averaged results for the analysis period (hours 6-20) show the control simulation is characterized by a deep mixed-phase cloud over the upwind mountain side and an upper-level ice cloud downwind (Figure 3.2a). Snow extends from a height of 7 km to below the freezing level upwind, where it reaches the surface over the mountain top, but melts into rain over UF, US, and DT (Figure 3.2a). Rain formed through warm-rain processes exists mainly over UF and US. Graupel forms over the top of the mountain and upwind slope, where vertical velocities are strong enough to sustain growth of rimed ice hydrometeors, and plenty of cloud water is available within supercooled cloud regions. The freezing level lowers towards the mountain, but does not actually intersect the mountain. As the flow descends on the lee side of the mountain, the wind speed increases by approximately 20 m s^{-1} and the freezing level rises to a height of approximately 4 km, caused by adiabatic warming. Trapped lee waves develop, with

narrow upward motion strong enough to generate clouds and snow, but no surface precipitation (Figure 3.2). In general, the flow follows the terrain and contains no wave-breaking or blocked flow upstream.

A Hovmöller diagram of precipitation rate shows an initial maximum over UT caused by rapid graupel development, fallout, and melting, followed by relatively steadier precipitation and a secondary period of intense precipitation (Figure 3.2b). Frozen precipitation (snow and graupel) reaches the surface within a narrow region centered over the mountain peak, while liquid precipitation extends to UF/US and DT, caused by melting of snow and advected rain (not shown). To avoid the 0-6 hour model spin-up period and gain a broader perspective of the effects caused by multi-parameter perturbations, our analysis is focused on hours 6-20, where the condensate development, and flow are relatively steady (Figure 3.2a).

A brief comparison of the control simulation in this study and that of M18 shows the difference caused by the increased mountain height. The taller mountain height (2 km) used in this study generates stronger vertical velocities that are able to sustain graupel development during hours 6-20 and produce higher PREC over the mountain top. In contrast, the control simulation in M18 with a 1 km mountain height had a PREC maximum over US and no graupel during hours 6-20.

3.3.2 Microphysical and environmental parameter perturbations

We first discuss which microphysical parameters are most influential to PREC when the environmental conditions are held constant within the control sounding based on the MultiParam

MOAT experiment. Figure 3.3 shows the μ_j^*-σ_j plots with each parameter color-coded and labeled. The MultiParam results show the largest effects on PREC occur over the upwind slope and top (Figure 3.3b,c), and are caused by changes to the snow fallspeed coefficient (A_s) and density (ρ_s), ice-cloud water collection efficiency (ECI), and rain accretion multiplicative factor (WRA). Notably, these parameters are the same as those identified by M18 as influential based on one-at-a-time individual parameter perturbations. Ranking the parameters from highest to lowest μ^* shows that A_s is ranked most important over more locations on the mountain than any other parameter (Figure 3.4a). In addition to having a large influence on PREC, the use of MOAT shows that A_s has nonlinear parameter interactions (i.e., large σ). This means there are a variety of elementary effects from changes to A_s, seemingly as a result of interactions with other parameters. A_s acts to directly affect the snow fallspeed and thus impacts existing snow aloft. The large variability in PREC responses to A_s is understandable, because various microphysical parameters and processes can impact how much snow is generated for A_s to subsequently act upon. Although not as highly ranked, ρ_s is also influential over all regions on the mountain. M18 found this parameter caused an unphysical indirect impact on snow fallspeeds through interactions with the particle size distribution. WRA is highest ranked over the upwind foothills and slope (Figure 3.4a). This is expected, as these locations have large amounts of cloud water and a deep melting layer creating a favorable environment for rain accretion (Figure 3.2a). Results also show that ECI and ice-ice collection efficiency (EII) are ranked highly over regions that would have cloud ice and supercooled water, respectively. Thus, the microphysical parameters' influence on PREC can vary spatially, depending on the specific processes

dominating over a particular region. Normalizing the rankings by the range of PREC (max – min computed per spatial region) generated from all simulations performed using MOAT gives us the fractional sensitivity of each parameter (Equation 3.4). Parameters with the highest fractional sensitivities are A_s and WRA (Figure 3.4b). This means that perturbations to A_s and WRA produce variability in PREC that is 30-50% as large as the total variation in PREC.

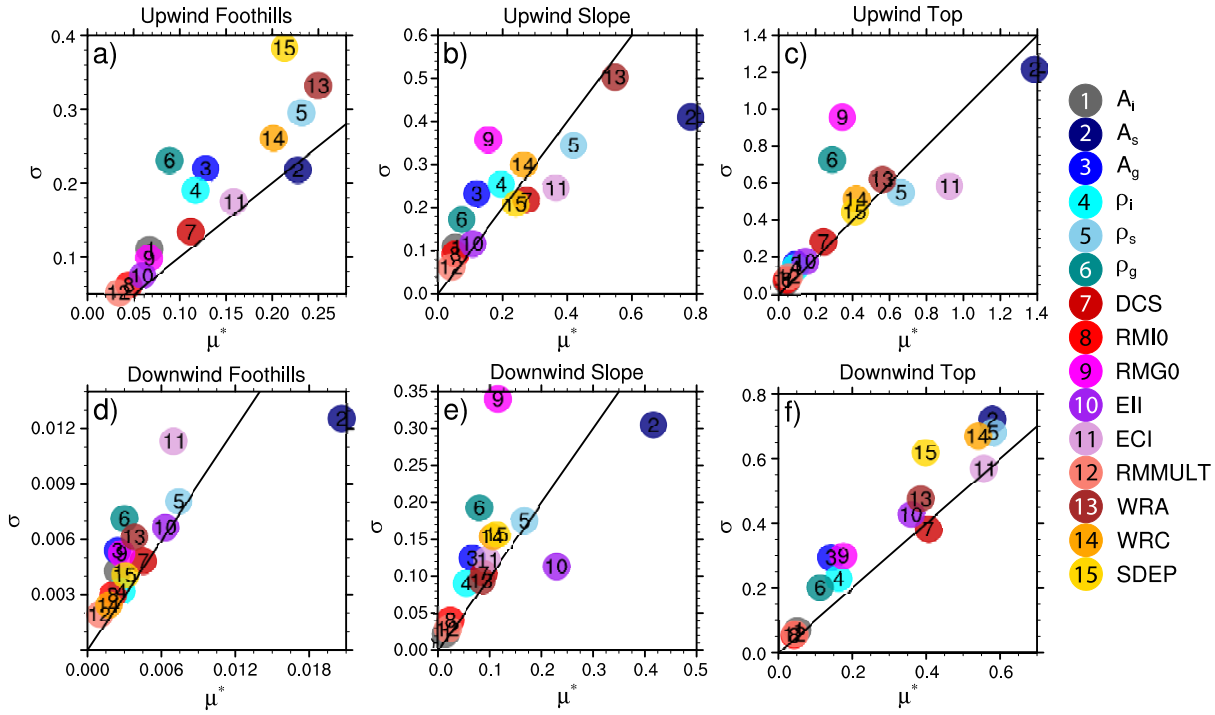

Figure 3.3 Mean magnitude μ_j^* and standard deviation σ_j for total precipitation rate (mm hr^{-1}) given 15 microphysical parameters varied using the MOAT screening method for the control environment (MultiParam). Labels j =1,…,15 correspond to the parameters listed in Table 3.1. Results are temporally and spatially averaged over the six locations on the mountain: (a) upwind foothills, (b) upwind slope, (c), upwind top, (d), downwind foothills, (e) downwind slope, and (f) downwind top. The one-to-one line is shown for reference.

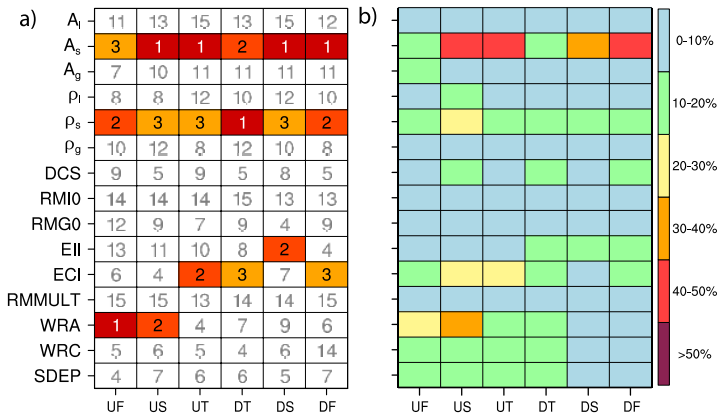

Figure 3.4 (a) Ranking of precipitation rate (mm hr^{-1}) sensitivity to parameters for MultiParam. Rank 1 represents the largest μ_j^* value, while Rank 15 or 19 represents the smallest μ_j^* value, for the simulations. Rows are the input parameters described in Table 1 and columns show results for each region over the mountain. (b) Fractional sensitivity (%) of precipitation rate (mm hr^{-1}) to parameters for MultiParam. Rows are input parameters described in Table 3.1 and columns show each region over the mountain.

Next, we describe the MOAT experiment MP_ENV that simultaneously perturbs microphysical *and* environmental parameters, testing the influence of environmental parameter uncertainty on PREC sensitivities to microphysics. The MP_ENV results show that perturbations to environmental parameters cause a larger change in PREC than microphysical parameter perturbations alone, mainly over regions UF, US, and DT (Figure 3.5). This is because changes in the environment affect the amount of moisture available, the resistance to vertical motion, and/or the type of precipitation that develops. Over the UF, US, and DT regions, perturbations to the RH result in the largest effects on PREC, while perturbations to RH and A_s have similar magnitudes of μ* over UT (Figure 3.5). These results show that although the environment does dominate the formation of condensate through dynamic-thermodynamic effects, in some regions, perturbations to microphysics are as important to surface precipitation as are perturbations to the

environment; over DS, microphysical impacts can actually be larger than those of the environment (Figure 3.5e). Additionally, the inclusion of environmental parameter perturbations can have an effect on the microphysical parameter sensitivities. For example, over UT in MultiParam, ρ_s and ECI have different μ^* values, but when environmental parameters are simultaneously perturbed, the value for ρ_s increases while the value for ECI decreases resulting in them having a similar influence as one another (Figure 3.5c). Overall, the MP_ENV results show that RH, θ_{sfc}, and U are the environmental parameters causing the largest changes to PREC (Figure 3.5).

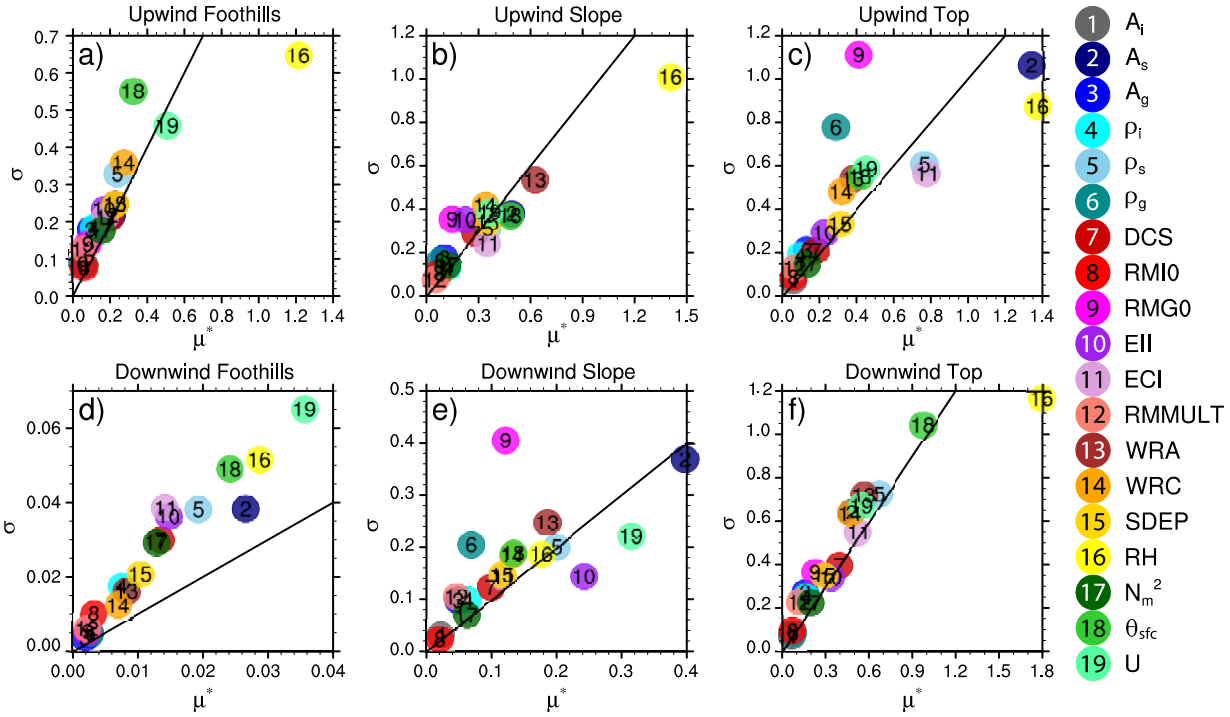

Figure 3.5 Same as Figure 3.3, except for MP_ENV, which includes the additional four environmental parameters varied using MOAT. Labels j = 1,…,19 correspond to the parameters listed in Table 3.1.

Ranking all the parameters by their μ* values shows the top parameters in MultiParam (A_s, ρ_s, ECI, and WRA) are also relatively influential in MP_ENV, but with A_s being the only microphysical parameter ranked as number 1 in at least one region (Figure 3.6a). Relative humidity is ranked as most influential over the windward side and DT/DF regions; this may be due to its effect on the number of grid points undergoing condensation in the model, resulting in changes to spatially-averaged condensation rates and the amount of condensate available to generate precipitation. Over DS, adiabatic warming leads to low RH, thus perturbations within 5-10% RH do not have a significant influence over this region. The surface potential temperature is most important over DT (Figure 3.6a), likely due to its effect on the freezing level height which affects the type of precipitation reaching the surface. The wind speed is most important over UF, DS, and DF (Figure 3.6a), most likely due to its impact on vertical velocities associated with uplift over the elevated terrain and subsequent effects on lee wave generation. Normalizing the μ* values shows RH and A_s are the most dominant parameters, responsible for fractional sensitivities of 30-50% (Figure 3.6b). The difficulty in trying to understand why A_s is such an important microphysical parameter arises when attempting to disentangle its interactions with other parameters. However, some microphysical parameter interactions can be plausibly explained. For example, the response of PREC to changes in ECI is moderately anti-correlated with the response to changes in A_s (correlation coefficient = -0.53). An increase in ECI results in more snow converted into graupel owing to more efficient riming of snow by cloud water, and because A_s only acts on existing snow, this reduction of the snow amount aloft limits the effect of perturbations to A_s. To quantify which parameter combinations are acting together to

influence PREC, a variance-based or Bayesian method would be required (Saltelli et al. 2008), which is beyond the scope of this study.

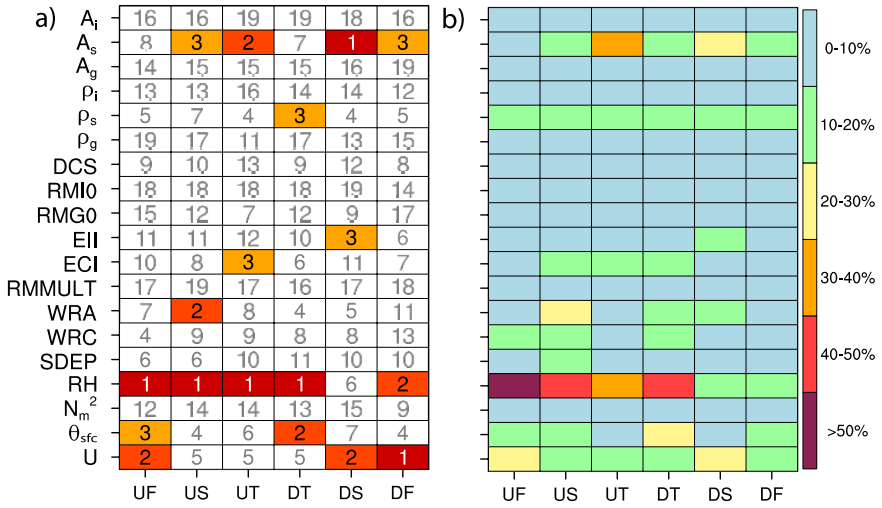

Figure 3.6 Same as Figure 3.4, except for MP_ENV, which includes the additional four rows for the environmental parameters described in Table 3.1.

The MP_ENV fractional sensitivity results show that over the regions with the largest μ* (UF, US, UT, and DT), the upwind top is the only location where both microphysical and environmental parameter perturbations have a large effect on PREC. If we compare the change in PREC caused by the three most influential environmental parameters (RH, θ_{sfc}, and U) to the maximum change in PREC caused by any microphysical parameter we observe generally similar magnitudes (Table 3.3). For example, over the upwind top the value of μ* for A_s (ranked 2) is 98% of the value for relative humidity (ranked 1). MP_ENV results show that both microphysical and environmental parameter perturbations can result in similar changes to PREC when perturbing over a typical observational uncertainty range for the environmental parameters.

Table 3.3 Ratio of maximum μ_j^* for j = 1-15 to μ_j^* for j = 16, 18, and 19 for experiment MP_ENV.

	UF (WRC)	**US (WRA)**	**UT (A_s)**	**DT (ρ_s)**	**DS (A_s)**	**DF (A_s)**
RH	20%	45%	98%	37%	226%	74%
θ	85%	130%	320%	68%	298%	110%
U	54%	172%	171%	122%	126%	93%

Total condensation rate <COND> (vertically integrated and horizontally-averaged over the domain sub-regions) is primarily affected by changes to the dynamics (vertical motion) and relative humidity, and secondarily by changes to the temperature. Figure 3.7 shows the parameters most influential (highest values of μ*) to <COND> are RH, U, θ_{sfc}, and WRA. Moving downwind over the mountain, we see more microphysical parameters acting to influence <COND>, with the largest μ* values occurring over DF and DS (Figure 3.7). These results show that the environmental parameters strongly impact condensation, as expected, through changes in the dynamics and thermodynamics. For example, increased U results in larger vertical velocities upwind of the mountain top, which triggers strong downslope winds and generates lee waves. Changes to θ_{sfc} affect the height of the freezing level and directly impact cloud water condensation/evaporation through the model's saturation adjustment scheme, while perturbing RH can influence the number of grid points that undergo condensation and thus the average condensation rate. WRA was shown to be a key influence on <COND> in M18, but using MOAT shows us that other microphysical parameters can also strongly affect condensation (Figure 3.7), evidently by impacting lee wave development which affects cloud development downwind of the mountain.

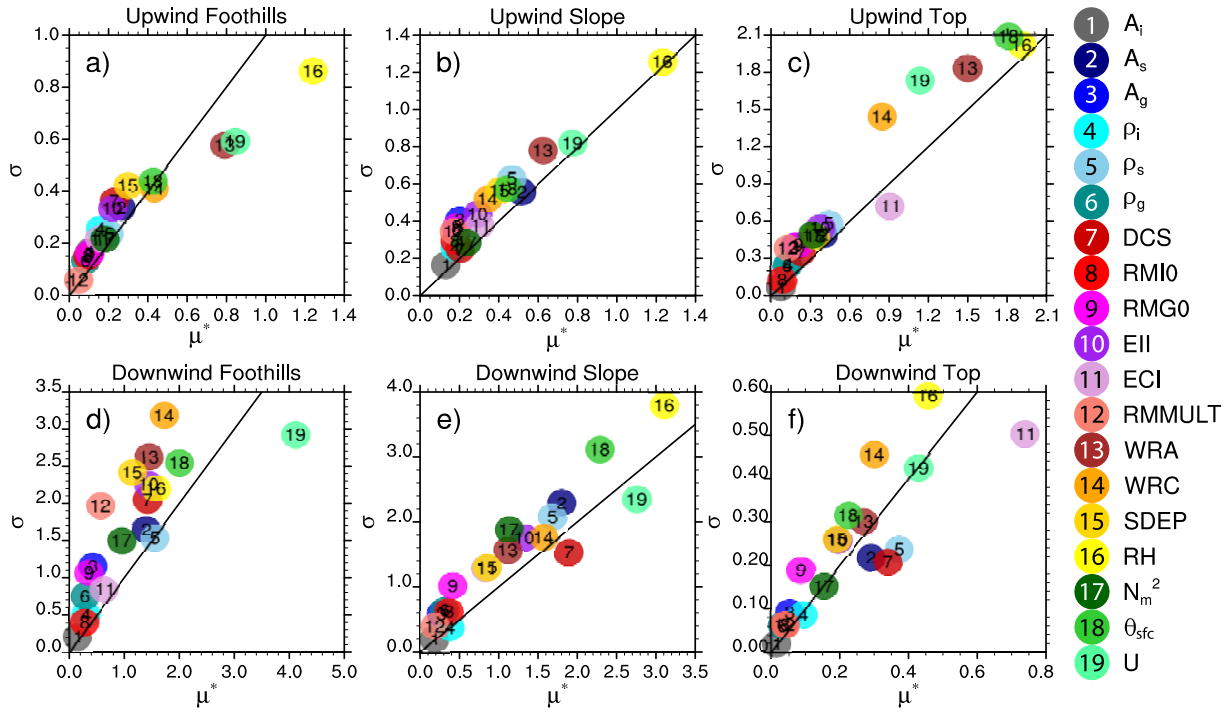

Figure 3.7 Same as Figure 3.5, except for total condensation rate (mm hr^{-1}).

Because precipitation efficiency PE is affected both by microphysical processes acting on condensate and condensate transport, it is reasonable that both microphysical and environmental parameters influence it (Figure 3.8). Changes to θ_{sfc} affect the phase of condensed water as well as the condensation rate, and changes to U directly impact condensate horizontal transport. Values of μ* for PE become very large over the downwind slope (Figure 3.8) because microphysical and environmental parameter perturbations affect transport of condensate to this region by horizontal advection, which can lead to relatively large PREC despite little generation of condensate locally, and hence very large values of PE. This analysis shows that the large changes in PREC over UT from perturbations to A_s (Figure 3.5c) are seemingly a result of the large influence A_s has on PE (Figure 3.8c) compared to <COND> (Figure 3.7c). Thus,

supporting the findings in M18, which conclude that the direct effects of A_s on the snow fallspeed, and hence transport, are the primary mechanism for this parameter's strong influence on PREC.

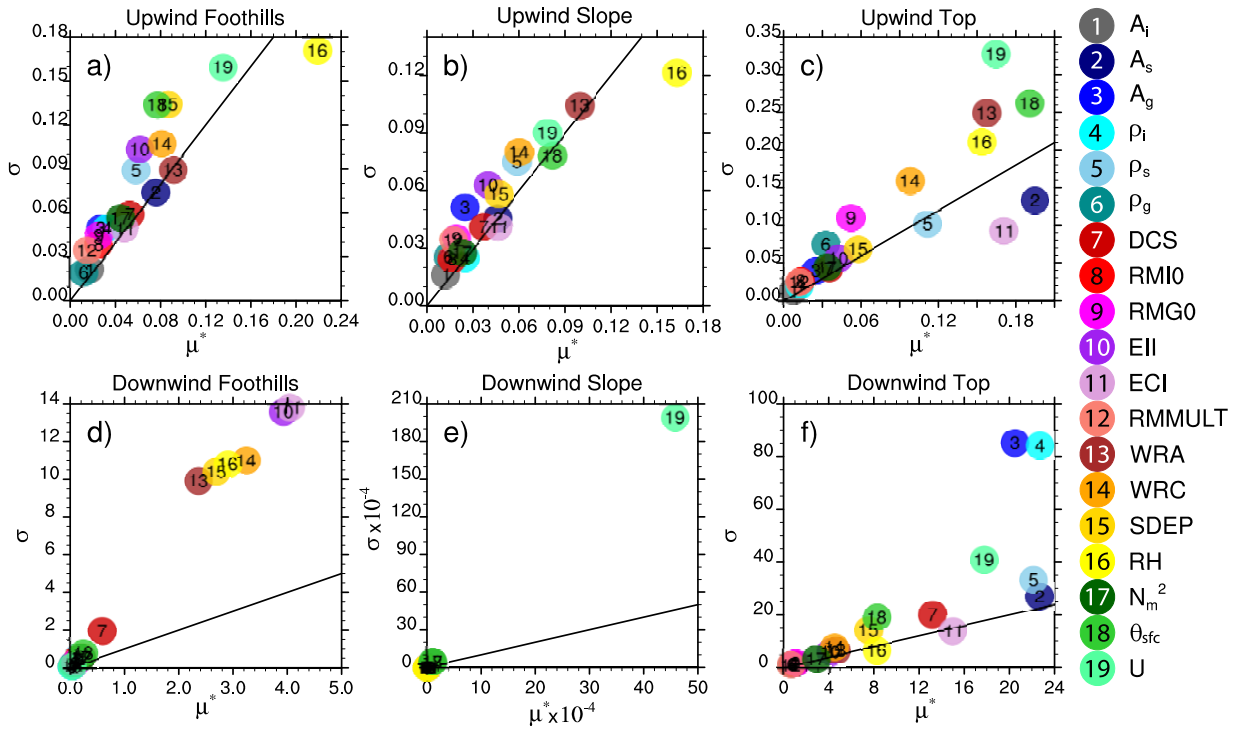

Figure 3.8 Same as Figure 3.5, except for precipitation efficiency.

3.3.3 Microphysical Parameter Perturbations in Different Environments

The MP_ENV results showed that microphysical parameter sensitivities are affected by relatively small changes in environmental parameters, and since the range of values chosen for the parameters can influence the results, we test different wind speed and surface potential temperature regimes within a climatological range to understand the impact of different processes and changes to available precipitable water on PREC. Figure 3.9 shows a summary of

PREC for simulations using the default microphysical parameter values and the MP_COLD, MP_WARM, MP_SLOW, and MP_FAST environments, compared to using the control environment. For the different wind regimes, the overall pattern of precipitation is similar, with a PREC peak over the upwind top (Figure 3.9a) and frozen precipitation only occurring over the mountain tops (not shown). The difference in PREC values between the slower and faster wind speed environments is mainly caused by changes to the vertical velocities over the upwind slope. Averaging over hours 6-20 and over the windward side, a maximum vertical velocity of 0.13 m s^{-1} occurs at a height of ~1.5 km above sea level (ASL) in the slower wind speed case, while the faster wind speed case produces a maximum vertical velocity of 0.25 m s^{-1} at a height of 2.7 km ASL. The warm environment is more similar to the control, but with slightly more precipitation over the upwind foothills/slope (Figure 3.9b). The freezing level in this case is approximately 1 km above the mountain top, thus there is a significant depth where frozen hydrometeors can melt. The only region where frozen precipitation occurs in the control and warm environment is over the mountain top. The cold environment has two PREC peaks, one over the upwind foothills where both liquid and frozen precipitation occurs and the other over the upwind top where all precipitation is frozen (Figure 3.9b). In this case, the freezing level intersects the mountain at about 1 km ASL, so that rain is limited to the UF and US regions, while all other regions have only frozen precipitation (not shown). The large difference in PREC amounts between the warm/control environments and the cold environment is caused by a reduction in precipitable water in the cold environment; it has precipitable water of 16 cm, while the warm and control environments have values of 33 cm and 27 cm, respectively.

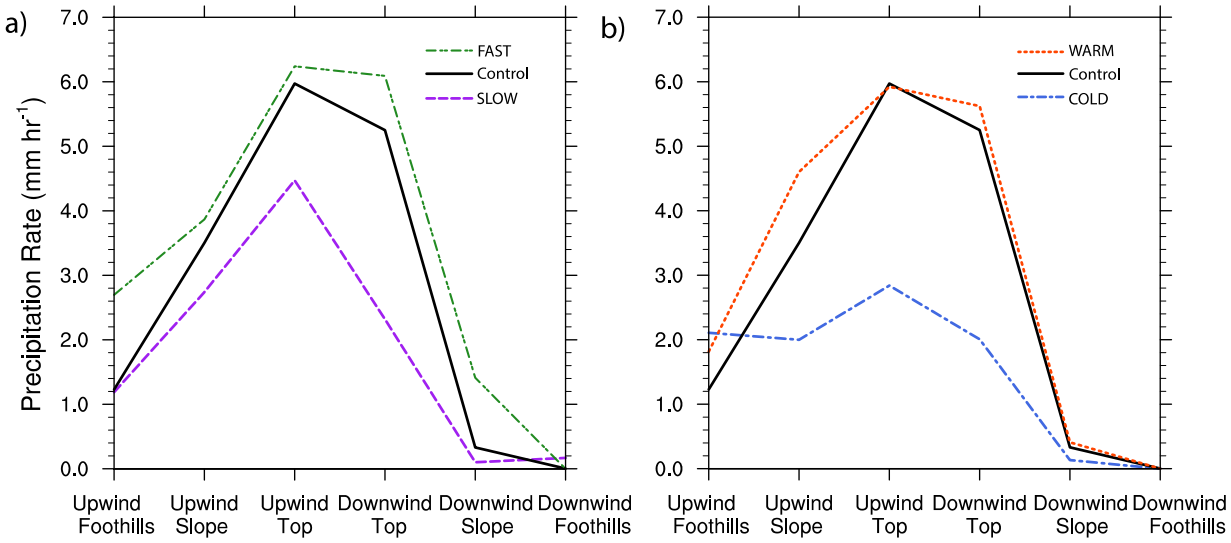

Figure 3.9 Temporally (hours 6-20) and spatially averaged (six regions) precipitation rate (mm hr^{-1}) for simulations with default microphysical parameter values and (a) reduced and increased wind speeds or (b) lower and higher θ_{sfc}. Solid black lines represent values using the control sounding.

3.3.3.1 MOAT Results for Wind Speed Regimes

Results for MP_SLOW show that perturbations to the microphysical parameters produce the largest influence on PREC over US, UT, and DT. The most influential parameter over US and UT is A_s (Figure 3.10), similar to the control environment. Over DT, the largest μ^* values are caused by WRA, DCS, and ρ_s. The MP_FAST results have the largest μ^* values over both slopes and tops and A_s is the most influential parameter in all four locations (Figure 3.11). Microphysical parameters that are moderately influential in this case are WRC, ECI, EII, WRA, and ρ_s.

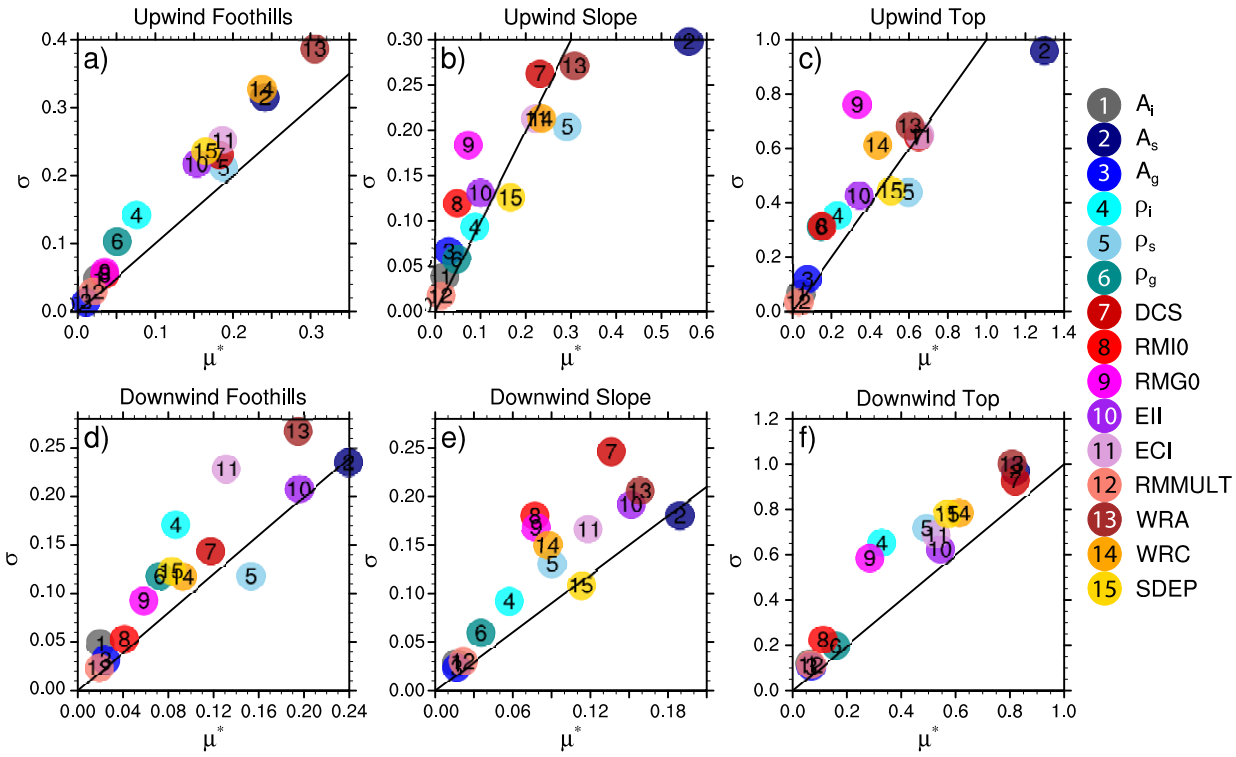

Figure 3.10 Same as Figure 3.3, except for experiment MP_SLOW.

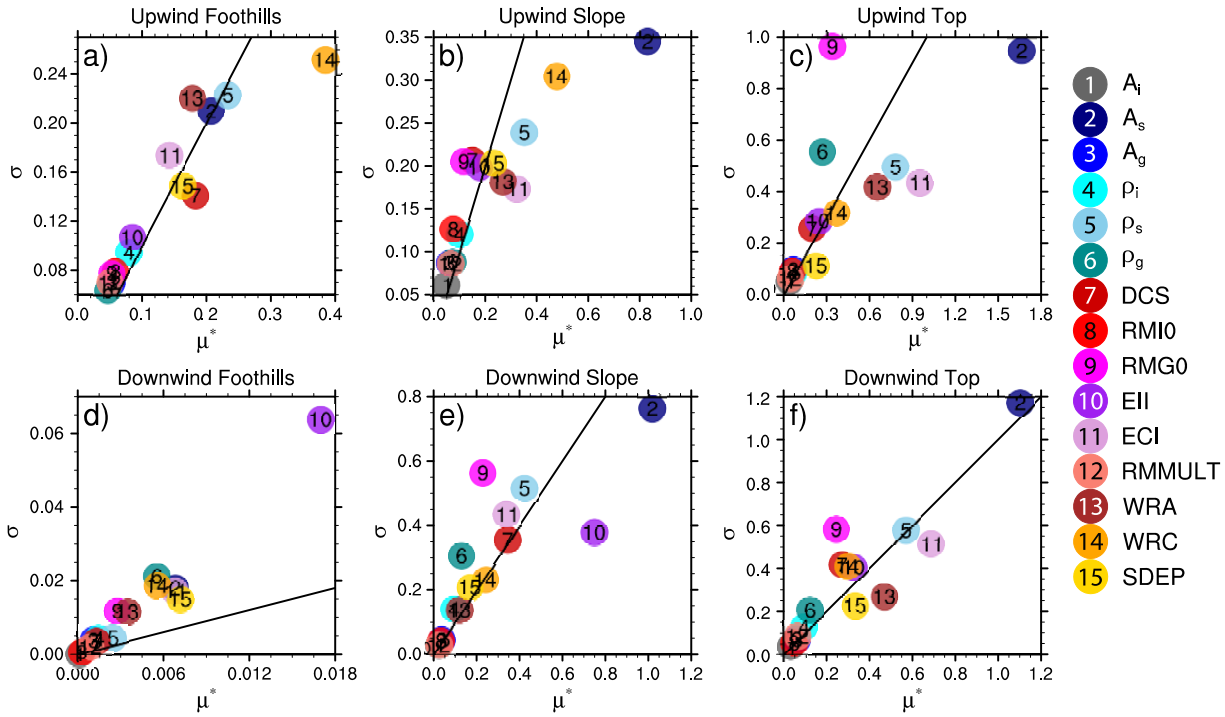

Figure 3.11 Same as Figure 3.3, except for experiment MP_FAST.

Fractional sensitivity results for these two experiments show there are many more microphysical parameters with FS >20% in MP_SLOW (Figure 3.12a) than in MP_FAST (Figure 3.12b) or the control (Figure 3.4b). We surmise that the weaker sensitivity to microphysics in MP_FAST and the control may be due to those environments being more dynamically forced. Stated another way, more rapid flow leads to stronger water vapor flux convergence upwind, and as such, condensate will form and precipitate regardless of changes to microphysical parameter values. Differences in fractional sensitivity over the downwind regions between MP_SLOW and MP_FAST may be due to the different mountain wave regimes that develop given the change in wind speed. The environment in MP_SLOW produces vertically-propagating, large amplitude lee waves, while MP_FAST and the control simulation produce

trapped lee waves with smaller amplitudes that dissipate in the vertical (Figure 3.13). We hypothesize that the waves in MP_SLOW trigger a wider region downwind to reach its lifting condensation level where latent heating then further enhances buoyancy and condensate development, e.g., the vertical velocities are strong enough to form graupel at mid-levels (Figure 3.13). MP_FAST does not form condensate downwind as the wave amplitude is small over very narrow regions. Therefore, precipitation downwind would be more sensitive to changes in microphysical parameters for MP_SLOW because this environment allows for cloud, snow, and graupel to form downwind, while condensate over DT and DS in MP_FAST is mainly formed upwind of the mountain top and advected downwind. The control simulation does form clouds and some snow in the mid-levels over DF despite the trapped lee waves; this may be due to some threshold wave amplitude being met that allows for enough upward motion to generate condensate. Nonetheless, A_s continues to have a large fractional sensitivity regardless of wind speed regime (Figure 3.12a,b). If we separate the PREC results into liquid and frozen (snow + graupel) components, details emerge as to how each environment affects precipitation type. Results for MP_SLOW show that the liquid precipitation is most sensitive to A_s and WRA (Figure 3.12c). In MP_FAST we see that frozen precipitation is sensitive to additional parameters: ρ_s, EII, and ECI also have large impacts on frozen precipitation (Figure 3.12d).

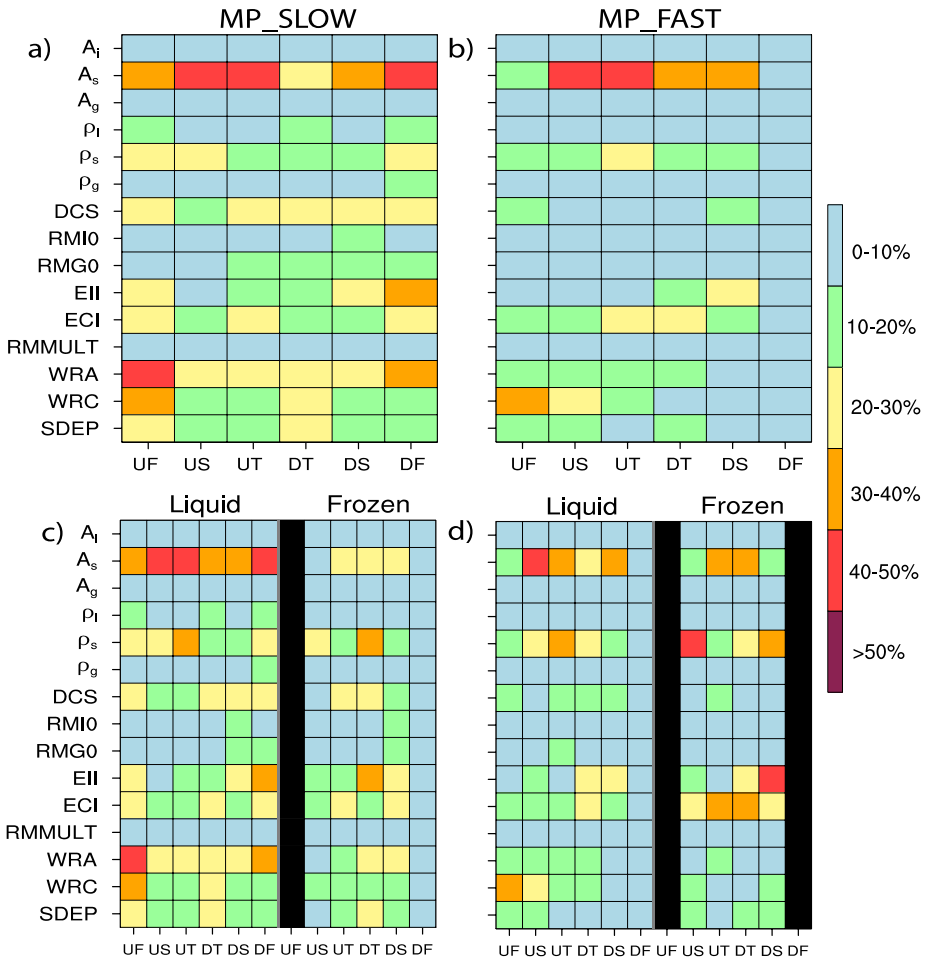

Figure 3.12 Top panels are the same as Figure 3.4a, but for experiments MP_SLOW (left panels) and MP_FAST (right panels). Bottom panels show the fractional sensitivity (%) for liquid and frozen precipitation rate (mm hr^{-1}) for their respective environmental experiments. Black shaded cells represent no precipitation over these regions.

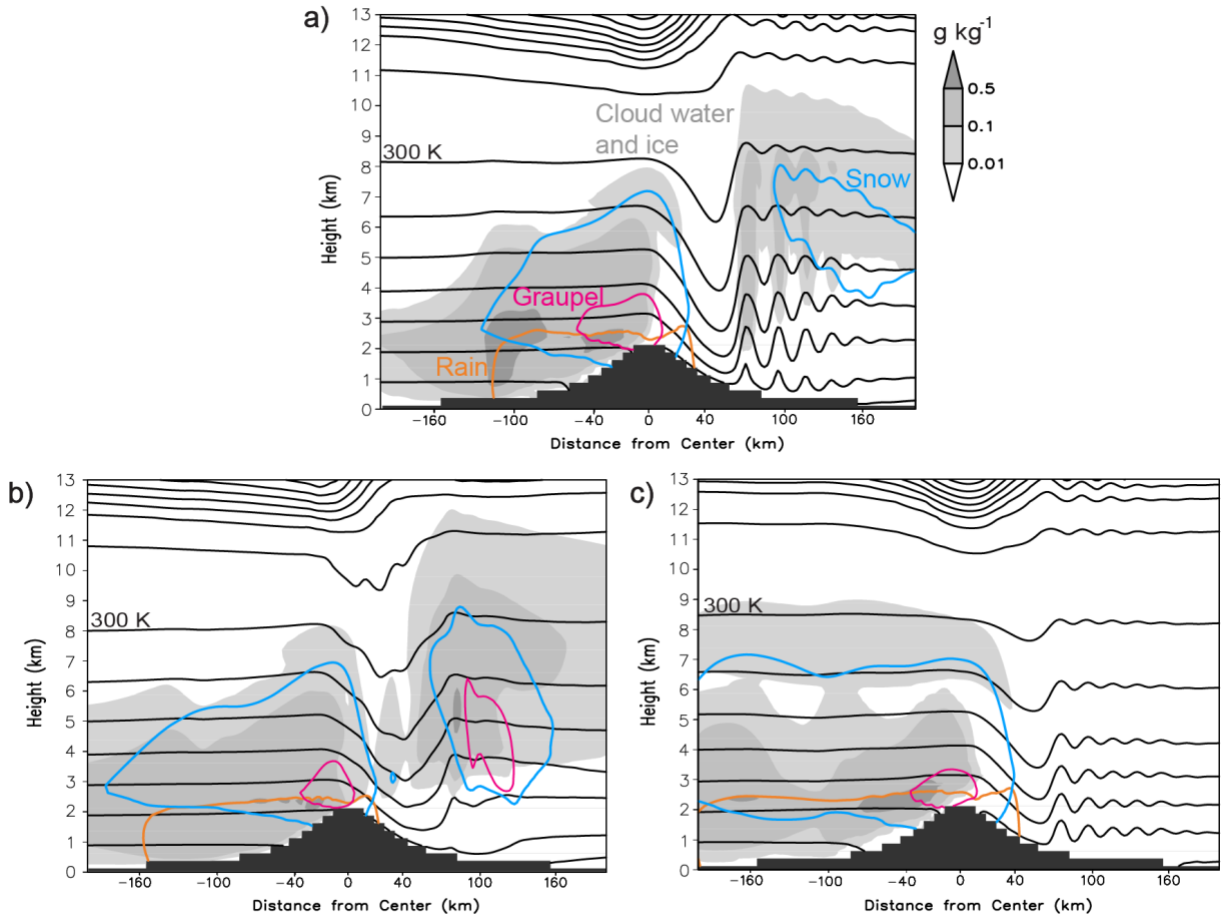

Figure 3.13 Temporally-averaged (hours 6-20) vertical cross-sections over a portion of the domain for simulations using the (a) control sounding, (b) slower wind speed profile used in MP_SLOW, and (c) faster wind speed profile used in MP_FAST. Shaded contours represent cloud water and ice mixing ratios (g kg^{-1}). Colored contours represent the 0.05 g kg^{-1} mixing ratio for snow (cyan), rain (orange), and graupel (magenta). Black contours are isentropes starting at 270 K at 5 K intervals (the 300 K isentrope is labeled for reference).

3.3.3.2 MOAT Results for Temperature Regimes

Results for MP_COLD have relatively smaller values of μ* compared to the other experiments, but all regions except DF have non-negligible values (Figure 3.14). The most influential parameter for UF and DS is A_s, and for US it is WRA. The upwind and downwind

tops both have a cluster of parameters considered influential in this case: A_s, WRA, EII, ECI, and WRC for UT, and A_s and EII for DT (Figure 3.14c,f). Similar to MP_FAST, results for MP_WARM show the largest μ* values occur over both the mountain slopes and tops (Figure 3.15). In this case it is clear that A_s is the most influential parameter overall, and WRA, WRC, ECI, and ρ_s are moderately influential over the slopes and tops (Figure 3.15).

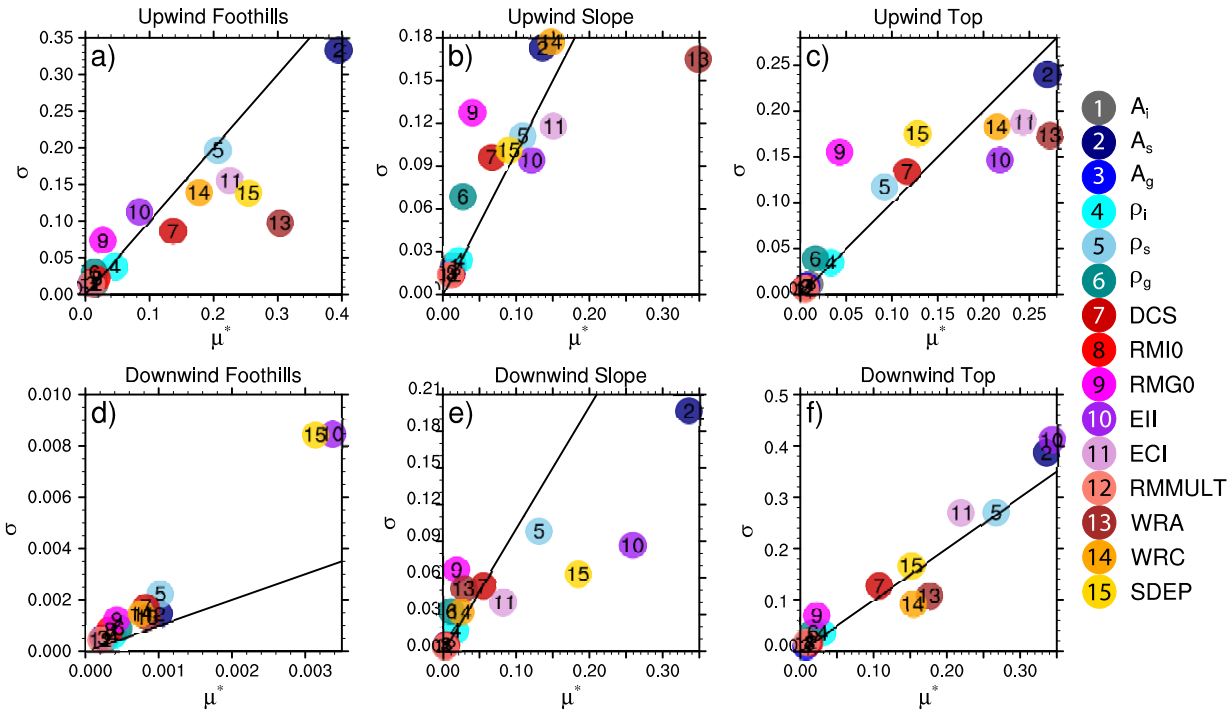

Figure 3.14 Same as Figure 3.3, except for experiment MP_COLD.

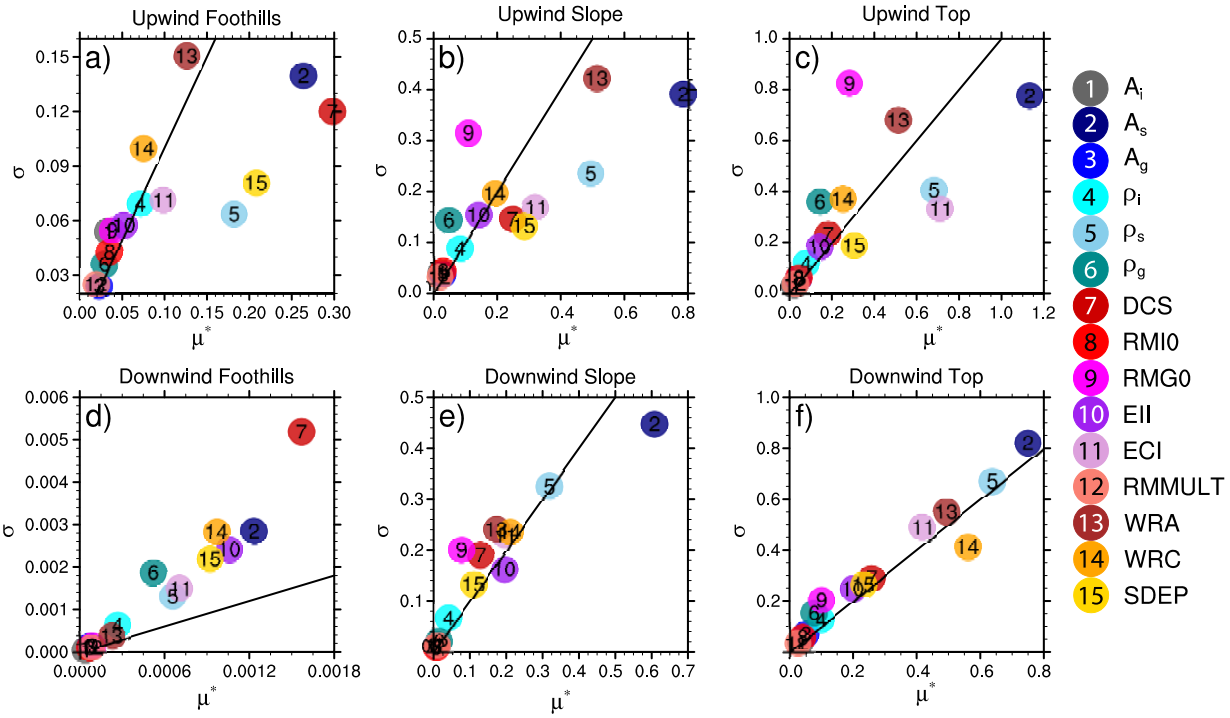

Figure 3.15 Same as Figure 3.3, except for experiment MP_WARM.

Fractional sensitivities for PREC show that A_s leads to FS values >30% regardless of the temperature regime. MP_COLD has more parameters with FS values >20% compared to MP_WARM; these include ice-ice (EII) and ice-cloud water (ECI) collection efficiency, rain accretion (WRA), cloud water autoconversion (WRC), and snow deposition (SDEP) (Figure 3.16a,b). Liquid precipitation is sensitive to A_s and ρ_s in both temperature regimes, meaning that most of the liquid precipitation may be a result of snow melting compared to warm-rain processes (Figure 3.16c,d). For frozen precipitation, MP_COLD has fractional sensitivities > 30% for A_s, EII, and WRA, while ρ_s and ECI are responsible for FS >30% in MP_WARM (Figure 3.16c,d), emphasizing the influence of mixed phase processes in a warmer environment.

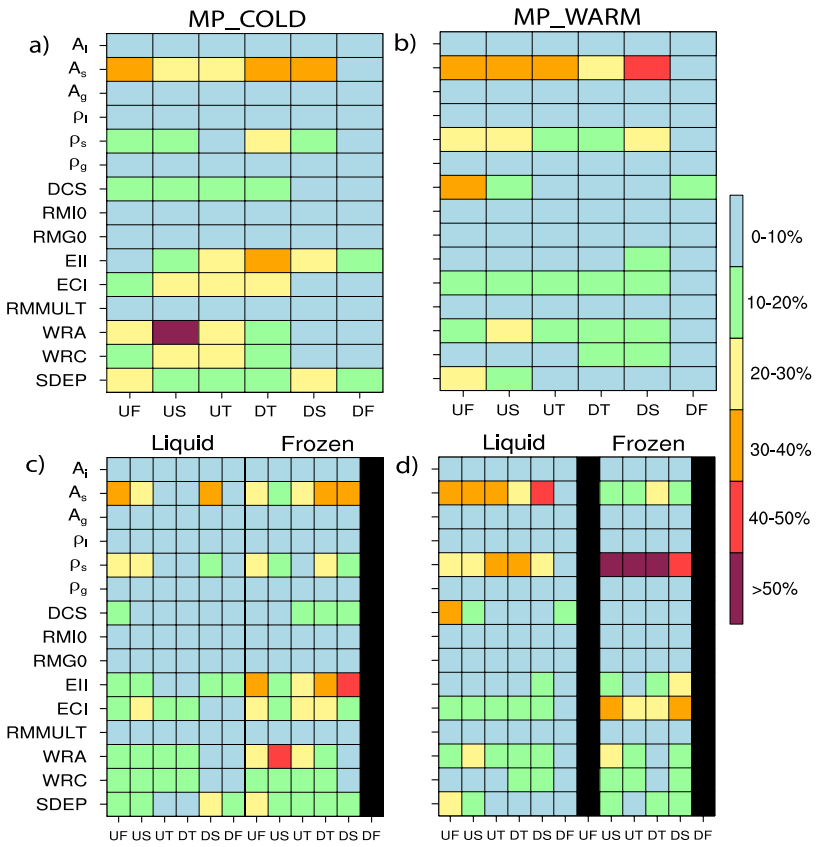

Figure 3.16 Same as Figure 3.12, but for experiments MP_COLD (left panels) and MP_WARM (right panels) for top panels.

3.3.4 Microphysical Parameterization Tests

In this section, we compare variations in PREC caused by microphysical parameter perturbations within a single scheme using MOAT (MultiParam) to those resulting from an ensemble of four different schemes (MultiPhys). The standard deviations shown in Figure 3.17 for the single scheme test are calculated from the PREC values produced by all 320 simulations using MOAT, while the standard deviations for the MultiPhys experiments are calculated from the PREC values from the four-member ensemble with different schemes; all of which are

calculated for the five environments: control, colder temperature, warmer temperature, slower wind speed, faster wind speed. Results from these tests show standard deviations for parameter perturbations in a single scheme produce variations in PREC with a similar order of magnitude to those caused by choosing an entirely different scheme (Figure 3.17). We also see a strong spatial nonlinearity of precipitation sensitivities, i.e., standard deviations vary with location over the mountain. For the MultiPhys experiments, the standard deviations are largest over DT for warm, fast, and slow environments, while the peak standard deviations occur over UT for the control and cold environments (Figure 3.17).

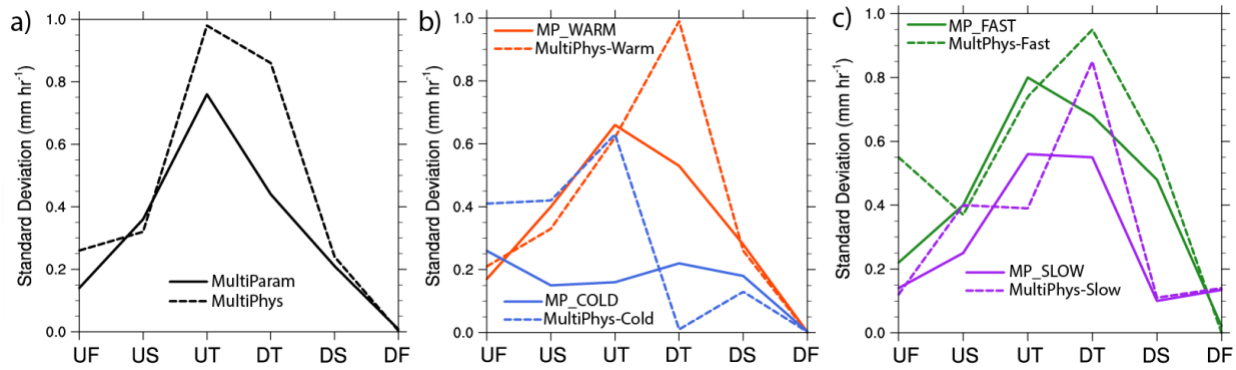

Figure 3.17 Precipitation rate standard deviation (mm hr^{-1}) temporally averaged (hours 6-20) and spatially averaged (6 regions) for the (a) control environment (black), (b) warmer (orange) and colder (blue) environments, and (c) slower (purple) and faster (green) wind speed environments. Solid lines represent results from multiple microphysical parameter perturbations using a single scheme with MOAT. Dashed lines represent the MultiPhys experiment. See Table 3.2 for a description of the simulations.

3.4 Summary and Conclusions

CM1 was used to perform idealized 2D simulations of moist, nearly neutral flow over a bell-shaped mountain. The model configurations and initial sounding were similar to that used in M18, except a 2 km mountain height is used here. Experiments perturbing multiple

microphysical parameters (MultiParam) were compared to experiments where both microphysical and environmental parameters were simultaneously perturbed (MP_ENV). The objective of these simulations was to explore orographic precipitation sensitivities to microphysical and environmental parameter perturbations using the Morris one-at-a-time (MOAT) method, which simultaneously perturbs a large number of parameters at low computational cost. This is in contrast to nearly all previous parameter sensitivity studies that varied parameters individually while holding all other parameter values fixed. Four different environments were also tested to determine how the multi-parameter MOAT results change in colder (MP_COLD), warmer (MP_WARM), slower wind speed (MP_SLOW), and faster wind speed (MP_FAST) environments. MOAT was applied for the first time to the study of orographic precipitation sensitivity, providing unique insight on the most influential parameters to precipitation and their interaction with other parameters. Finally, we compared the PREC variability caused by perturbations to microphysical parameters within the Morrison scheme to the variability found in a four-member ensemble using entirely different microphysics schemes (MultiPhys).

The most influential parameters on orographic precipitation were A_s, ρ_s, ECI, and WRA, especially over the upwind slope and top. These are the same parameters having the largest influence on PREC in the one-at-a-time parameter perturbations tests in M18. In addition to causing a large change in PREC, A_s had a large range of elementary effects, which demonstrated its strong interaction with other parameters. Furthermore, A_s had a larger effect on precipitation efficiency compared to total condensation rate, emphasizing its direct effects on snow fallspeed

and subsequent condensate advection. The location over which each parameter is influential depended on the processes active in that region. For example, WRA was most influential over the upwind foothills and slope as these locations contained large amounts of supercooled water and a deep melting layer. A_s and WRA were found to contribute 30-50% of the total PREC variation in the MultiParam simulations.

M18 showed that large changes in the environment influence the total amount of condensate produced, thereby affecting the influence a particular microphysics parameter can have on PREC. Our focus was on understanding relative sources of model uncertainty, and as such, the environmental parameter perturbations tested were small (informed by estimates of typical observational uncertainty). Even so, these perturbations were influential to <COND> and resulted in a relative decrease of microphysical parameters' influence on PREC. The most influential environmental parameters to PREC were RH, θ_{sfc}, and U, resulting in large PREC changes over the upwind foothills and slope, and downwind top, mainly due to effects on <COND> through updraft development and lee wave formation. Interestingly, out of the four most influential parameters found in MultiParam, A_s and WRA remained influential to PREC in MP_ENV, with A_s perturbations leading to nearly the same (98% as large) PREC variability over the upwind top as that caused by RH perturbations. This suggests that improved representation and observational constraint of the fallspeed of snow particles would be useful. Results from this study show strong spatial variability in the parameters' influence, as well as demonstrating that both microphysical and environmental parameters are important to orographic precipitation uncertainty.

Different temperature and wind speed regimes were tested, and although these other environments impacted the amount of available condensate and location of peak precipitation, A_s remained the most important microphysical parameter in all four environmental experiments. In the wind speed regime tests, more microphysical parameters had a fractional sensitivity >20% in MP_SLOW compared to MP_FAST, which may be due to stronger dynamical forcing and different mountain wave regime in the latter. The temperature regime tests showed large changes to the location and amount of liquid versus frozen precipitation. This is because the freezing level decreased in MP_COLD, leading to liquid precipitation falling mainly over the upwind slope. The spatial change in dominant precipitation processes resulted in the microphysical parameters' influence on PREC to also vary spatially. MP_WARM results showed that snow aloft was important for liquid precipitation production, while mixed phase processes were important for frozen precipitation.

This study tested many of the user-prescribed parameters within the Morrison scheme, but there remain various thresholds and processes within the scheme that could be tested with MOAT in the future. A caveat of the MOAT method is that results may change depending on the range of uncertainty used. Parameter sensitivities would need to be re-tested if a specific parameter's uncertainty range were to be narrowed, but results would be dependent on whether that parameter interacts with the others, i.e, if that parameter has no influence on other parameters, then changing its uncertainty range will not cause much change in the results.

Chapter 4. Multivariate Sensitivity Analysis of Orographic Precipitation Using a Markov Chain Monte Carlo Algorithm (Morales et al. 2019, In prep.)

4.1 Introduction

Moist, nearly neutral flow forced to rise through orographic lift commonly produces heavy precipitation during non-convective events (Roe 2005; Houze 2012; Zagrodnik et al. 2018). For this study, we focus on moist neutral flow associated with atmospheric rivers (ARs), which are synoptic features that transport large amounts of moisture from the tropics to higher latitudes (Ralph et al. 2018). Atmospheric rivers are responsible for 95% of the meridional water vapor flux around the globe and are critical to the global water cycle (Zhu and Newell 1998). For example, ARs produce up to 50% of the annual precipitation for California, often from a couple of storms yielding large amounts of snowfall in the northern Sierra Nevadas (Dettinger et al. 2011). Orographic precipitation from ARs can end droughts (Dettinger 2013), but can also lead to severe flooding and landslides causing damage to infrastructure and loss of life (Ralph et al. 2006; Porter et al. 2011; Florsheim and Dettinger 2007)

Because neutrally stratified flow exerts little to no resistance to the vertical displacement caused by encountering a mountain, condensation over the upwind slopes mainly depends on the speed of the upslope component of the flow and the moisture content available (Roe et al. 2005; Houze et al. 2012). Observational studies have shown high correlations between these upstream environment characteristics and orographic precipitation rates (Pandey et al. 1999; Neiman et al. 2002; Ralph et al. 2013; Lin et al. 2013; Purnell and Kirshbaum 2018). Neiman et al. (2002)

found that 58% to 88% of the variance in surface rain rates over the coastal mountains of California could be explained by the upslope flow speed measured near the coast. Similarly, Ralph et al. (2013) found 74% of the rainfall variance can be accounted for through a linear relationship with upslope integrated water vapor flux or IWV, which combines observations of moisture content and wind speed. When upslope flow is not the dominant forcing for precipitation development, additional mechanisms such as the "seeder-feeder" process can enhance orographic precipitation (Neiman et al. 2002; Purnell and Kirshbaum 2018).

Although these past studies have shown that the upstream environmental conditions are important to determining if precipitation will occur, the details of precipitation amount, type, and location become more complicated as we account for the complex relationships between environmental and microphysical parameters. For cooler ARs during winter, stronger upslope wind speeds can compensate for reduced precipitable water amounts (Ralph et al. 2013). The horizontal advection of snow can also be affected by environmental parameters such as surface temperature and horizontal wind speed, i.e., a lower freezing level favors more frozen condensate to spill over into the lee, especially with an increased wind speed (Colle 2004; Kunz and Kottmeier 2006; Mott et al. 2014; Wang et al. 2017). The microphysical melting distance, the depth below cloud base over which frozen precipitation can melt before it reaches the surface, increases with increasing surface temperature in idealized simulations of orographic precipitation and can impact precipitation type (Minder et al. 2011) and the dominant microphysical processes, i.e., warm-rain or ice processes (Colle 2004; Miglietta and Rotunno 2006; Morales et al. 2018 (hereafter M18)).

A study by Lin et al. (2013) comparing observations of multiple wintertime storms over the West Coast of the U.S. to model forecasts showed a systematic overprediction of orographic precipitation and ice water content aloft during events when the freezing level existed below the average mountain height. This positive model bias is thought to be related to the representation of ice processes within bulk microphysics schemes and thermodynamic/dynamics processes that can affect frozen hydrometeor development (Lin et al. 2013). Microphysics parameterizations represent precipitation and cloud processes that cannot be directly resolved by numerical weather prediction (NWP) models. Various parameters exist within these schemes that are known to naturally vary in space and time yet are typically set at some constant value, i.e., graupel particle density. These parameters also have an inherent uncertainty arising from limited measuring and observation capabilities, as well as lacking a physical equivalent in nature, i.e., thresholds for converting cloud water to rain. Multiple studies have shown that the value of these parameters can influence surface orographic precipitation and liquid and ice water content (Colle and Zeng 2004b; Colle et al. 2005; Miglietta and Rotunno 2006; Jankov et al. 2007, 2009; Liu et al. 2011; M18). For example, decreasing the snow particle fallspeed can shift the peak precipitation rates to the downwind side of the mountain, as the snow is horizontally transported away from its source region; a similar process occurs when the degree of riming is changed (Hobbs et al. 1973; Colle and Mass 2000; Lin and Colle 2009, 2011; Morrison et al. 2015; M18). Microphysical processes, such as the collection of cloud droplets by rain, can influence the location of precipitation and also affect the thermodynamics of the system through changes to cloud water (M18).

Most of these studies perform orographic precipitation sensitivity analysis by perturbing one parameter at a time while keeping the rest constant (e.g., Colle 2004; Colle and Zeng 2004a, b; Miglietta and Rotunno 2006; Kirshbaum and Smith 2008; M18). These are termed "one-at-a-time" methods (OAT), which are invaluable to our understanding of the physical (or nonphysical) effects of parameter perturbations to precipitation but neglect the possibility of nonlinear parameter interactions. An OAT study by M18 showed that not only can the microphysical parameter value influence orographic precipitation, the sensitivities can change with different upstream environments. For example, perturbations to microphysical parameters linked to snow fallspeed affected precipitation location, but for a lower wind speed environment, weaker responses were observed due to reduced amounts of available condensate caused by weaker updrafts (M18). In general, environmental parameters are largely responsible for the total amount of available condensate for microphysical parameters and processes to act on, in addition to determining which microphysical processes (warm-rain or ice processes) will dominate specific mountain regions (M18). Accounting for changes in other parameters of interest can influence the precipitation sensitivity to an individual parameter.

To properly account for every possible combination of parameters would require M^N simulations, where N represents the number of parameters and M represents the number of discrete values to test. This "brute force" method quickly becomes computationally expensive, and sifting through the results could become unmanageable, especially for a large number of parameters. To combat part of this issue, Morales et al. (2019; hereafter M19) applied the Morris one-at-a-time (MOAT) method, a screening method that calculates elementary effects

(Campolongo et al. 2007) to determine parameters whose perturbation led to large changes in precipitation. MOAT is efficient for a large number of parameters, and provided a straight-forward and statistically robust way of determining which parameters resulted in the largest changes to orographic precipitation. This parameter subset contains: snow fallspeed coefficient (A_s), ice-cloud water collection efficiency (ECI), rain accretion (WRA), relative humidity (RH), horizontal wind speed (U), and surface potential temperature (θ_{sfc}). The microphysical parameters were also found to be influential by OAT methods in M18.

Results from M19 showed strong nonlinear responses to changes in A_s, meaning that the impact of A_s on precipitation depends on the value of other parameters; a simple analysis was performed and M19 found a negative correlation with ECI. Although MOAT was useful to reduce the number of parameters of interest, the method could not provide detailed information on parameter (co)variability. For example, A_s and ECI may co-vary, but is their relationship linear or is there a more complex response? M19 showed that other parameters could have relationships, but what are they? The past studies described here have shown mitigating factors can play a role in this type of orographic precipitation system, e.g., stronger upslope wind speeds can compensate for reduced moisture amounts (Ralph et al. 2013). Which parameters can compensate for the effects of others, leading to an overall null effect on precipitation? For the most influential parameter subset found in M19 there exist a range of physically realistic values, but do all these values have the same probability of producing a specific precipitation amount or distribution? Examining every parameter combination within the N-dimensional parameter space would be incredibly costly. M18 and M19 both examined the sensitivity of orographic

precipitation to changes in microphysics and the upstream environment, however, in addition to understanding the key controls on precipitation, it is also useful to understand which combinations of model parameters and environment can lead to a particular outcome; e.g., heavy precipitation on the upwind slope. This requires a different sort of experiment, one in which we seek combinations of parameters that produce a given precipitation distribution. Since not all combinations are likely to result in the desired outcome, a method is required that can sample the entire parameter space, while identifying specific combinations of control variables that produce the precipitation distribution of interest.

A 2015 study by Tushaus et al. showed the potential for application of Bayesian inference methods to explore multivariate sensitivity in an orographic precipitation system. Tushaus et al. (2015) used an idealized model framework focusing on upslope precipitation from liquid-only processes to understand precipitation sensitivity to environmental and mountain shape parameters. Their results found non-linear responses for different parameters and "tipping points" where the wave dynamics drastically changed across a sharp gradient in the parameter space, thus providing a poor fit to the desired simulated precipitation rates for small changes in horizontal wind speed. The particular method used in Tushaus et al. (2015) is a Markov chain Monte Carlo (MCMC) algorithm (Posselt 2013), where Monte Carlo represents random sampling of values within the parameter space and Markov chain represents a series of proposed values (a chain) the next of which only depends on the current value within the parameter space. MCMC has been used as a sensitivity analysis tool for the study of tropical and deep moist convection, particle dispersion in the boundary layer, climate sensitivity, and coastal hurricane

variations (Pang et al. 2001; Elsner et al. 2004; Avila and Raza 2005; Tomassini and Reichert 2007; Delle Monache et al. 2008; Posselt and Vukicevic 2010; Santos et al. 2016; Posselt 2016), as well as used to explore error characteristics of cloud satellite retrievals and determine the effectiveness of radar and satellite observations to data assimilation, and parameter estimation, to name a few (Posselt et al. 2008; Posselt and Bishop 2012; Van Lier-Walqui et al. 2012). Although MCMC has been a prolific tool in atmospheric science over the past two decades, Tushaus et al. (2015) is the only study we know to apply MCMC to the study of orographic precipitation sensitivity analysis.

As opposed to brute force methods previously described, a Bayesian framework provides effective and efficient exploration of the N-dimensional parameter space and combines prior information with model data to produce a joint *posterior* probability distribution of the input parameters and observations (Posselt and Vukicevic 2010). The maximum (mode) of this distribution will provide the "optimal" value estimate for a specific observation or model output, but the real perk of MCMC is the probability density functions mapped for each parameter, which provide information on inter-parameter correlations and can be sampled from to improve ensemble forecasts. MCMC can also provide guidance on the effectiveness of including certain observations in data assimilation efforts, as well as determining the range of uncertainty needed for individual observations.

The present study extends the Bayesian sensitivity analysis on orographic precipitation performed by Tushaus et al. (2015) by adding more complexity and realism to the model and

initial sounding, i.e., including ice processes and using more realistic wind speed and relative humidity profiles (M18 and M19). We use MCMC to explore the following science questions:

1. Which parameter combinations yield a given orographic precipitation spatial distribution and do any covariances exist between parameters?
2. Given that the MCMC algorithm only uses total precipitation to constrain the result, does there exist a subset of simulations where more of the total precipitation falls as snow/graupel compared to rain?

We hypothesize that there will be more than one combination of parameters that can produce a similar precipitation distribution, as M19 found high non-linearity for microphysical and environmental parameters with a strong effect on precipitation amount. Non-linearities can arise from non-unique solutions, i.e., similar precipitation rates produced by different values of a specific parameter, or can arise from interactions with other parameters, i.e., the effect of parameter X on precipitation can vary given the value of parameter Y. For example, M19 found a negative correlation between the snow fallspeed coefficient (A_s) and ice-cloud water collection efficiency (ECI), meaning that the precipitation sensitivity of A_s could possibly change depending on the value ECI. Additionally, environmental experiments have shown that wind speed changes can impact the horizontal transport of precipitation (Colle 2004; Kunz and Kottmeier 2006; Mott et al. 2014; Wang et al. 2017; M18; M19). Therefore, we hypothesize that

there may exist values of horizontal wind speed that could compensate for changes in A_s to produce a similar precipitation at the surface.

Previous studies have shown that microphysical parameter sensitivity can change depending on the environment, due to spatial changes in dominant microphysical processes and changes in dynamical forcing strength and mountain wave regimes (Colle and Zeng 2004b; Miglietta and Rotunno 2006; M18; M19). Since the MCMC algorithm is only constrained by the total precipitation rate, it is hypothesized that different environmental combinations could arise where most of the precipitation is frozen versus liquid, or vice versa. Additionally, M19 showed parameters' influence on precipitation can change depending on the region over the mountain. For example, it was found that perturbations to A_s could produce precipitation changes of similar magnitude to perturbing relative humidity over the upwind slope of the mountain, but nowhere else (M19). Therefore, it is hypothesized that differences in parameter sensitivities will be found over different regions on the mountain.

4.2 Methodology

4.2.1 Model Configuration

Cloud Model 1 (CM1; Bryan and Fritsch 2012) version 17 is used with a model configuration following M19, but because the Markov chain Monte Carlo (MCMC) method requires hundreds of thousands of simulations, changes had to be made to the total run time and time step. Tests showed that results from M19 were similar when temporally and spatially averaged from hours 6-20 and hours 6-16 (not shown). Additional tests concluded that MCMC

results using an averaging period from hours 6-9 produced similar results to those from hours 6-16 (not shown). Therefore, the total run time was set to 9 hours using a time step of 6 seconds. These changes reduced computational expense and wall-clock time. For a full summary of the model configuration, see Chapter 3, Section 2 (M19). A quasi two-dimensional (2D) domain of 1600 km length is used, where the inner 1200 km domain has a horizontal grid spacing of 2 km and the 50 grid points on either side have horizontal grid spacing stretched up to 6 km. The vertical depth of the model is 18 km, where the vertical grid spacing below 9 km is 0.25 km, increasing to 0.5 km between 9 km and 10.5 km, and remaining constant at 0.5 km from 10.5 km to the model top. Open radiative lateral boundaries are applied, as well as a no-slip bottom boundary condition. Coriolis acceleration and parameterizations for radiation, land-surface, and boundary layer are neglected to simplify the system and focus the study on the impact of microphysical processes to precipitation, thermodynamics, and dynamics. The Morrison microphysics scheme version 3.4 (Morrison et al. 2005; 2009) is used with the rimed ice species set to graupel.

A Gaussian mountain profile is used with a mountain height of 2 km and a half-width of 40 km. These values have been used in past studies to idealize the Sierra Nevada and Cascade Mountains as 2D infinite ridges (Colle and Zeng 2004a, b). The initial sounding idealizes the observational sounding from an atmospheric river event on 13 Nov 2015 during the Olympic Mountain Experiment (OLYMPEX, Houze et al. 2017) using a simple 1-2-1 smoothing filter. Similar to M19, the idealized upstream sounding is characterized as moist, nearly neutral with a tropospheric moist Brunt-Vaisala Frequency N_m^2 of $4x10^{-5}$ s^{-2} and a surface potential temperature

of 286 K. The stratospheric N_m^2 of $5x10^{-4}$ s^{-2} is set above the tropopause height (approximately 12 km). The relative humidity (RH) profile is constant at 95% from the surface to 4.5 km, then linearly decreases to RH=20% at a height of 16 km where it remains constant until the model top is reached. The horizontal wind speed (U) profile starts at 14 m s^{-1} at the surface, linearly increasing to 42 m s^{-1} at a height of 12 km and remaining constant at 42 m s^{-1} until the model top is reached.

4.2.2 Microphysical and Environmental Parameters

Results from our previous studies (M18 and M19) have shown that one-at-a-time and multivariate perturbations to microphysical parameters, such as snow fallspeed coefficient (A_s), ice-cloud water collection efficiency (ECI), and the rain accretion process (WRA) cause the largest relative changes to orographic precipitation in a moist, nearly neutral environment. The most influential environmental parameters to orographic precipitation were relative humidity (RH), horizontal wind speed (U), and surface potential temperature (θ_{sfc}). Thus, it is appropriate for the present study to focus our experiments on understanding the combinations of parameters within this subset (Table 4.1) that can produce the total precipitation rate distribution from the control simulation described in Section 2.1. Although snow particle density was also found to be influential to orographic precipitation in M19, the present study neglects this parameter as its precipitation response has been shown to be unphysical (M18). Table 4.1 shows the range of values used for the six parameters and the default values for the control simulation used to produce the synthetic precipitation observations that constrain the MCMC algorithm. The

MCMC analysis is performed using hourly precipitation rates temporally averaged from hours 6-9 and spatially averaged over six regions on the mountain (Figure 4.2c).

The range for A_s is increased to include faster falling snow particles, while the ranges for ECI and WRA remain the same as those used in M18 and M19. Note, the units for A_s are $m^{(1-b)}s^{-1}$ due to the nature of the power law that represents the snow fallspeed equation, $V_s=A_sD^{Bs}$, where D is the snow particle diameter in meters. The range of values for θ_{sfc} and U were increased to include a variety of different environments, as the MCMC method will determine the environments best suited to produce the prescribed precipitation distribution and intensity and we do not want to restrict the algorithm to a narrow range of options. The surface horizontal wind speed spans environments with slow wind speeds (10 m s^{-1}) to fast wind speeds (20 m s^{-1}), while the surface potential temperatures span from 280 K to 293 K, acting as a proxy for freezing level height, i.e., an increase in surface temperature will increase the freezing level and vice versa. The range of values for RH encompasses low-level values of RH between 80% and 99%, keeping the low-levels moist, but unsaturated until parcels are lifted by the mountain. These environments have been observed using dropsondes and satellite observations over the western coast of North America (Ralph et al. 2005; Neiman et al. 2008).

Table 4.1 List of microphysical and environmental parameters, ranges, and control values.

Parameter description	**Units**	**Control**	**Min**	**Max**
Snow fallspeed coefficient (A_s)	$m^{(1-b)}\ s^{-1}$	11.72	5.86	23.44
Ice-cloud water collection efficiency (ECI)	--	0.7	0.3	1.0

Rain accretion multiplicative factor (WRA)	--	1	0.5	2.0
Relative humidity profile additive factor (RH)	%	RH(z)	RH(z) - 10%	RH(z) + 10%
Surface potential temperature (θ_{sfc})	K	286	280	293
U-wind speed profile additive factor (U)	m s^{-1}	U(z)	U(z) - 4 m s^{-1}	U(z) + 6 m s^{-1}

4.2.3 Experimental Design and Markov chain Monte Carlo (MCMC) Method

The goals of our Bayesian inference experiments are to 1) determine all the possible parameter value sets $\boldsymbol{x}$ that produce a given total precipitation rate spatial distribution and intensity $\boldsymbol{y}$, and 2) understand the sensitivity of orographic precipitation to changes in the microphysical and environmental parameters. The large dataset of simulations produced by MCMC can then be mined to determine if any of the possible environments able to produce $\boldsymbol{y}$ could have produced a larger fraction of frozen precipitation. A six-element vector $\boldsymbol{x}$ = [$\mathbf{A_s}$**, ECI, WRA, RH,** $\boldsymbol{\theta_{sfc}}$**, U**] represents the parameters described in Table 4.1, each with a uniform prior probability distribution where each value within the given range are equally likely to occur. A control CM1 simulation run with the default parameter values (Table 4.1) produces the "synthetic observations" of total precipitation rates (mm hr^{-1}) over six regions on the mountain (Figure 4.2c): upwind foothills (UF), slope (DS), and top (DT), and downwind foothills (DF), slope (DS), and top (DT). These *synthetic observations* are represented by the six-element vector $\boldsymbol{y}$ **= [**$\mathbf{P_{UF}}$**,** $\mathbf{P_{US}}$**,** $\mathbf{P_{UT}}$**,** $\mathbf{P_{DT}}$**,** $\mathbf{P_{DS}}$**,** $\mathbf{P_{DF}}$**]** described by a Gaussian probability distribution centered around the control precipitation values with standard deviations for each region shown in Table

4.2. The standard deviation, or observational error, informs the algorithm how far it can stray from the truth and still accept the proposed parameters as being a good fit. These standard deviation values where calculated from the ensemble of simulations where microphysical and environmental parameters were perturbed used the Morris one-at-a-time screening method in Morales et al. (2019). There is more flexibility allowed in the MCMC algorithm over the two mountain top regions, while the upwind foothills and downwind regions have less flexibility. A caveat of the MCMC methods is that results can be sensitive to the choice of standard deviation (Tushaus et al. 2015).

Table 4.2 Temporally and spatially averaged total precipitation rates (mm hr^{-1}) for the control simulation and the standard deviations (mm hr^{-1}) used in the Gaussian likelihood distribution.

	UF	**US**	**UT**	**DT**	**DS**	**DF**
Total Precipitation Rate	1.55	3.41	4.89	5.45	0.372	4.25E-6
Standard Deviation	0.4	0.6	0.8	0.8	0.2	0.02

Markov chain Monte Carlo (MCMC) methods perform repeated random sampling of the multi-dimensional parameter space to map the joint probability density function (PDF) of model parameters **x** and observations or model output **y** using Bayes' theorem:

$$P(\boldsymbol{x}|\boldsymbol{y}) = \frac{P(\boldsymbol{y}|\boldsymbol{x})\,P(\boldsymbol{x})}{P(\boldsymbol{y})}, \qquad (4.1)$$

where the *posterior* distribution $P(\boldsymbol{x}|\boldsymbol{y})$ is estimated from the conditional probability density $P(\boldsymbol{y}|\boldsymbol{x})$, representing the *likelihood* parameters $\boldsymbol{x}$ are the true parameters leading to $\boldsymbol{y}$, and the

prior probability distribution of the parameter values $\boldsymbol{x}$. The likelihood also represents the uncertainty in the observations or model output $\boldsymbol{y}$ given a set of input parameters $\boldsymbol{x}$. The prior represents the initial knowledge of (including uncertainty in) our input parameters. The posterior represents the updated probability distribution of the input parameters after we incorporate information from the observational or model data, which is the conditional distribution of $\boldsymbol{x}$ given $\mathbf{y}$. To summarize, MCMC methods can approximate the value or distribution of values for a parameter of interest by randomly sampling values from a probability space by updating the *a priori* parameter probability distribution given additional information from observations or models. Details on the theory behind MCMC can be found in Posselt (2013) and references therein.

In practice, the MCMC algorithm performs a "random walk" across the multi-dimensional parameter space to find regions where input values have a high probability of producing our synthetic observations. Figure 4.1 illustrates the steps performed in a single iteration of the MCMC algorithm, and we note that the procedure in Fig. 4.1 is repeated for hundreds of thousands of successive iterations.

Step 1: For each iteration of the algorithm, a proposed set of parameters $\hat{\boldsymbol{x}}$ is generated from a proposal distribution $q(\boldsymbol{x_i}, \hat{\boldsymbol{x}})$ centered around the current estimate of the parameter values $\boldsymbol{x_i}$, i.e., the current location within the parameter space. The variance of this proposal distribution is tuned over a number of iterations at the start of each Markov chain to assure the algorithm is efficiently sampling the parameter space, while also sampling smaller regions of

high probability (Tushaus et al. 2015). This is called the adaptive *burn-in* period and the parameter sets sampled during this period are neglected from the analysis.

Step 2: The proposal set $\widehat{\boldsymbol{x}}$ is then used to run the forward model $\widehat{\boldsymbol{y}} = f(\widehat{\boldsymbol{x}})$, i.e., CM1 with the configurations described in Section 1.

Step 3: The resulting model output (i.e., simulated precipitation rates) are compared to the synthetic observations or "truth" (i.e., precipitation rates produced by control simulation) by calculating an acceptance ratio ρ, which is described as the following equation for a uniform prior (Posselt et al. 2008):

$$\rho = \frac{P(\boldsymbol{y}|\widehat{\boldsymbol{x}})}{P(\boldsymbol{y}|\boldsymbol{x_i})} \tag{4.2}$$

Step 4: If the proposed parameter set $\widehat{\boldsymbol{x}}$ provides a better or similar fit to the desired precipitation distribution compared to the current parameter set $\boldsymbol{x_i}$ ($\rho > 1$), then the proposed set $\widehat{\boldsymbol{x}}$ is accepted and saved as a sample $\boldsymbol{x_{i+1}} = \widehat{\boldsymbol{x}}$ of the joint PDF $P(\boldsymbol{x}|\boldsymbol{y})$ (Fig. 1). This means that the precipitation rates produced by the proposed set of parameters are within the given standard deviation or observational error. If the proposed set $\widehat{\boldsymbol{x}}$ does not provide a better fit to the precipitation distribution ($\rho < 1$), a test number is randomly chosen from uniform (0,1) and compared to the value of ρ. If the acceptance ratio is greater than the random number, the parameter set is accepted as a sample of the joint PDF (this is called *probabilistic acceptance*). For this study, the algorithm also performs a *delayed reject* (Posselt et al. 2017), whereby additional parameter sets can be proposed from the initially rejected set (i.e., two additional proposals are allowed). This provides the algorithm opportunities to sample the space in smaller

steps to find possible pockets of higher probability near low probability regions. If the proposed parameter set is rejected, an additional copy of the current parameter set is saved $\boldsymbol{x_{i+1} = x_i}$ and a new proposal is generated, continuing the MCMC processes until the prescribed number of model iterations are completed. Details on this version of the MCMC algorithm can be found in Posselt (2016) and Posselt et al. (2017).

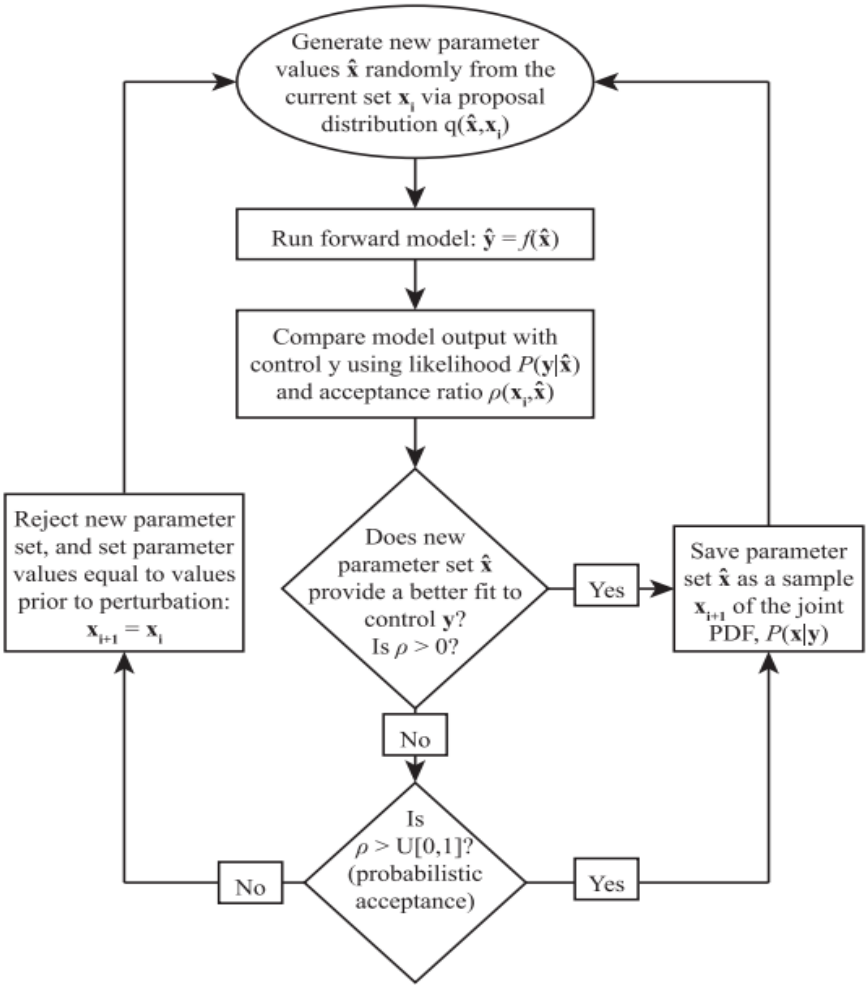

Figure 4.1 Flowchart illustrating the Markov chain Monte Carlo process. (from Tushaus et al. 2015).

Multiple Markov chains were run simultaneously to allow for more efficient sampling of the parameter space, with each chain initialized at a different randomly generated starting point. Ten chains were used with approximately 20,000 iterations each. After iterations associated with the burn-in period were removed, a total of 199,290 samples remained for analysis. This number of iterations was determined to be sufficient for the current analysis.

4.3 Results

4.3.1 Control Simulation

The control CM1 simulation temporally-averaged from hours 6-9 is characterized by the development of a deep mixed-phase cloud upwind of the mountain peak where snow, graupel, and rain develop (Figure 4.2a). As the flow descends the mountain it adiabatically warms, producing a cloud-free region over the downwind top and slope (Figure 4.2a). Trapped lee waves develop downwind, with vertical velocities strong enough to form ice clouds aloft and narrow mixed-phase clouds over the upwind foothills, but no precipitation (Figure 4.2a,b). Peak total precipitation rates occur over the downwind top, which is different from the results in M19; this is primarily because the analysis period is shortened to hours 6-9, while M19 extends the period to hour 20, allowing for sufficient time to develop more graupel and snow to cause a upwind top peak in total precipitation. The total precipitation rates produced during this period are used as the synthetic observations that constrain the MCMC algorithm, as described in Section 2 (Table 4.2). Separating total precipitation into its liquid-only and frozen precipitation components shows a double peak in rain over US and DT, and frozen precipitation over UT and DT (Figure

4.2b). The liquid precipitation in the UF region is formed through warm-rain processes, e.g., collision-coalescence, while the rain over US and UT forms through a combination of warm- and cold-rain processes, as the deep melting layer in this region allows for complete melting of snow and graupel. The secondary rain peak over DT originates from snow melting (Figure 4.2b).

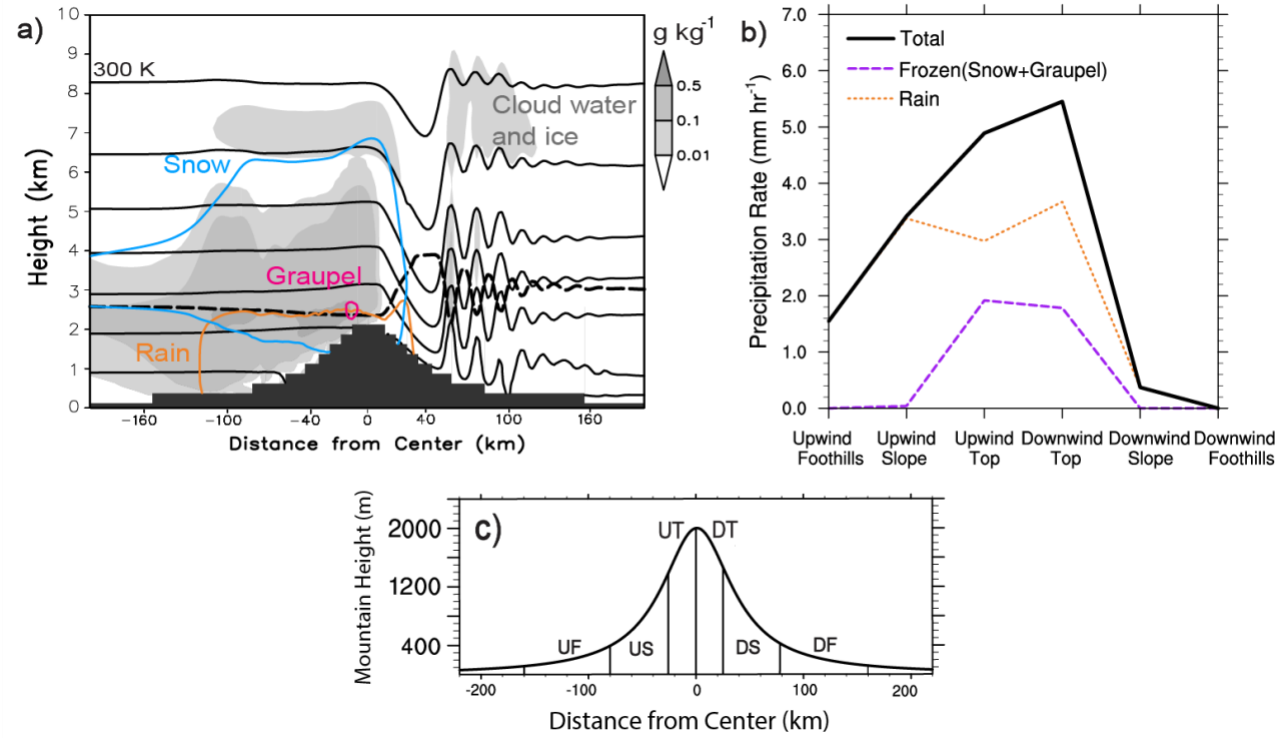

Figure 4.2 (a) Vertical cross-section showing temporally-averaged (hours 6-9) isentropes starting at 270 K at increments of 5 K (black contours), freezing level (thick dashed black line) cloud water and ice mixing ratios (shaded contours, g/kg), and 0.05 g/kg mixing ratio contours for snow (cyan), graupel (magenta), and rain (orange) for the control simulation over a portion of the domain. (b) Temporally and spatially averaged precipitation rate (mm/hr) of frozen precipitation (dashed purple line), liquid-only precipitation (dotted orange line), and total (frozen+liquid) precipitation (solid black line), over the six regions in the mountain shown in (c) the mountain height (m) profile: upwind foothills (UF), slope (US), top (UT), and downwind foothills (DF), slope (DS), and top (DT).

4.3.2 MCMC-based Analysis

The joint posterior PDF $P(\boldsymbol{x}|\boldsymbol{y})$ describing the combination of parameters $\boldsymbol{x}$ that produced a good fit to the synthetic precipitation observations $\boldsymbol{y}$ is calculated from multiplying the prior and the likelihoods computed from the MCMC algorithm. To more easily interpret the results of the 6-dimensional joint PDF, a two-dimensional (2D) marginal PDF for each pair of parameters are presented (Figure 4.3). Because the 2D marginal PDFs integrate over the remaining four parameters, the true value of the parameter pair may lie outside of any high probability regions, i.e., the higher probability region for two parameters may depend on the value of the others. In the 2D marginal PDFs, brighter colors represent regions of higher probability, i.e., the combination of parameter values produces a good fit to the observations, and darker colors represent regions of lower probability, i.e, the parameter values produce a poor fit to the observations.

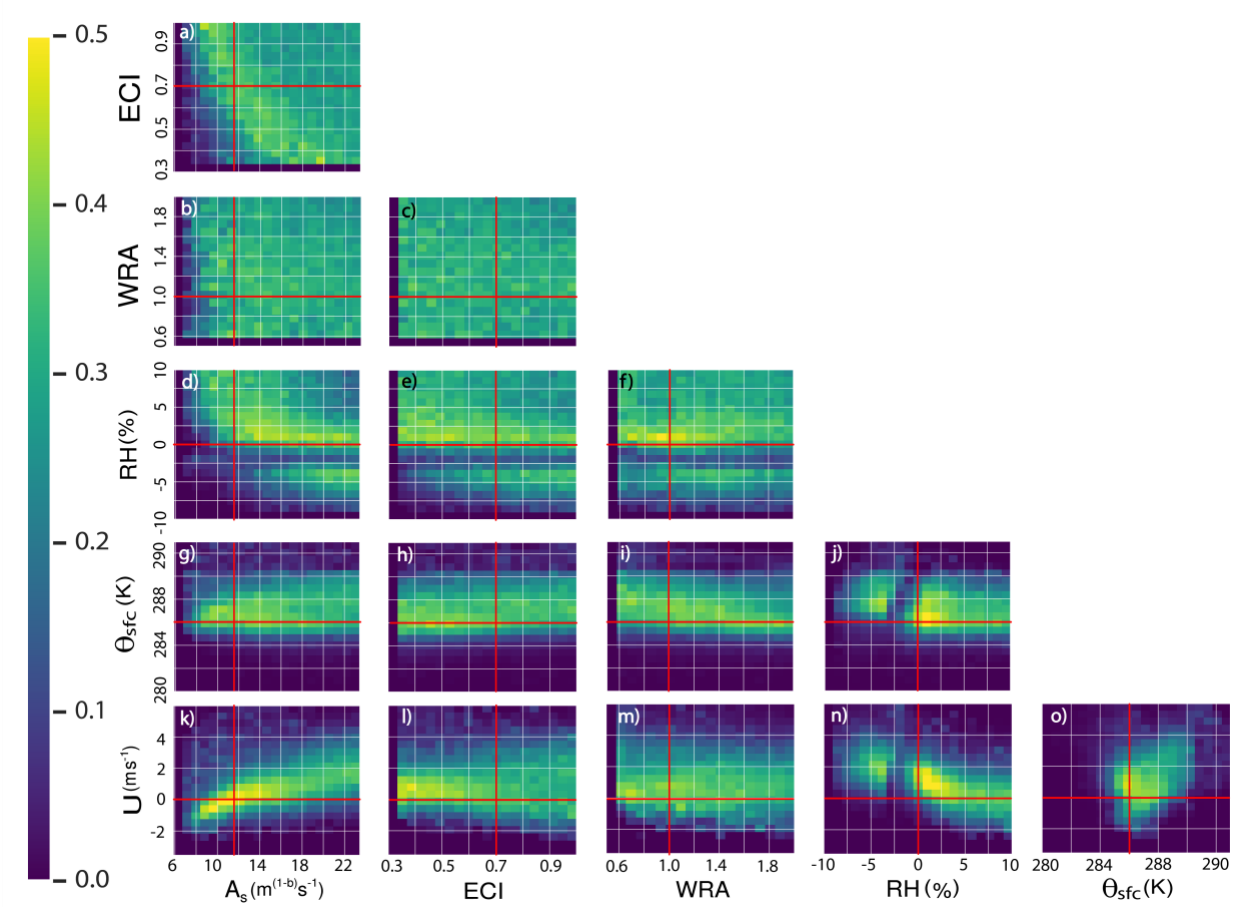

Figure 4.3 Posterior two-dimensional marginal PDFs for each pair of parameters from the MCMC experiment. In each panel, brighter and warmer colors represent regions of relatively higher probability density whereas darker and cooler colors represent regions of relatively lower probability density. The red lines show the locations of the parameter truth values (see Table 4.2).

The 2D marginal PDF of ECI and A_s supports the results found in M19 and show an inverse relationship, where A_s must increase if ECI is decreased to reproduce the control precipitation (Figure 4.3a). This relationship is expected, and is a good test of the MCMC algorithm, as these two parameters are found together in equations describing the accretion of supercooled cloud droplets onto snow and/or graupel and the conversion of rimed snow to

graupel within the Morrison scheme. In addition to confirming the inverse relationship, the 2D marginal PDF shows three distinct regions: a low-probability region for small values of A_s, a higher probability region (inverse relationship), and a moderate probability region where large values of A_s and ECI produce an acceptable, but not great match to the control precipitation values. The smaller values of A_s produce snow that falls too slow leading to an incorrect match to the synthetic observations, as the snow will be horizontally advected away from the upwind slope and either precipitate downwind or be advected far enough to experience sublimation or melting and subsequent evaporation, thus never reaching the surface.

In contrast, rain accretion (WRA) which represents the processes of rain drops removing cloud droplets through collision-coalescence has no clear relationship with ECI or A_s. This result is expected, as WRA is not directly linked to ECI or A_s through any processes in the Morrison scheme. Although WRA is allowed to occur both above and below freezing, the 2D marginal PDFs shows that any value of ECI or A_s (except very small A_s values) in combination with WRA can reproduce the control precipitation distribution. Thus, there is little precipitation sensitivity to WRA, which was also found in M18 and M19, the cause being a compensating effect between changes to precipitation efficiency and total condensation rates near the cloud base.

Results show a strong sensitivity to the value of surface potential temperature and horizontal wind speeds, illustrated by narrow regions of relative high temperature and wind speed probability, where values outside of these regions provide a poor fit to the synthetic observations (Figure 4.3g-o). The 2D marginal PDF for θ_{sfc} versus U shows a localized high probability region between 285 K and 289 K and surface wind speeds from approx. 11 m s^{-1} to

17 m s^{-1} (Figure 4.3o). It seems that most values for the microphysical parameters (A_s, ECI, and WRA) could be a good fit to the synthetic observations, as long as the θ_{sfc} and U values lie within their respective narrow regions (Figure 4.3g-i,l-m). Within the narrow U range, lower values of ECI produce a much better fit to the synthetic observations (Figure 4.3l). The clearest covariance between parameters and strongest sensitivity is shown in the 2D marginal PDF of A_s and U (Figure 4.3k). These two parameters show a positive relationship associated with horizontal transport of snow, i.e., if A_s is increased and snow falls faster, U will need to increase so that the precipitation falls over the appropriate region in order to maintain a good fit to the synthetic observations. Figure 4.3k shows that for A_s values close to the truth U values cannot deviate by more than 1 m s^{-1} or the precipitation distribution will be incorrect.

Relative humidity results show a narrow region of lower probability creating a secondary maximum between surface RH values of 91.5% and 87.5% (Figure 4.3d-f, and Figure 4.3j,n). This secondary high probability region is found when mapped against all other parameters. To further investigate the source of this lower probability, 2D marginal PDFs are presented for the six individual regions over the mountain. Instead of using the likelihood added up for all regions, the likelihoods for each region on the mountain are multiplied with the priors to produce the location-specific joint posterior PDFs. Comparing all regions, the upwind foothills is the only region that prominently shows the low probability region for RH compared with all other parameters (Figure 4.4d-f,j,n). A possible positive slope in the 2D marginal PDF for θ_{sfc} and RH appears (Figure 4.4j), while a possible negative slope appears for RH versus U (Figure 4.4n). This analysis isolates the source of the secondary maximum to precipitation effects over UF, but

analysis comparing temporally-averaged vertical cross-sections for different values of RH do not show any substantial differences in the wave patterns, flow, or cloud distributions (not shown) that could explain the feature.

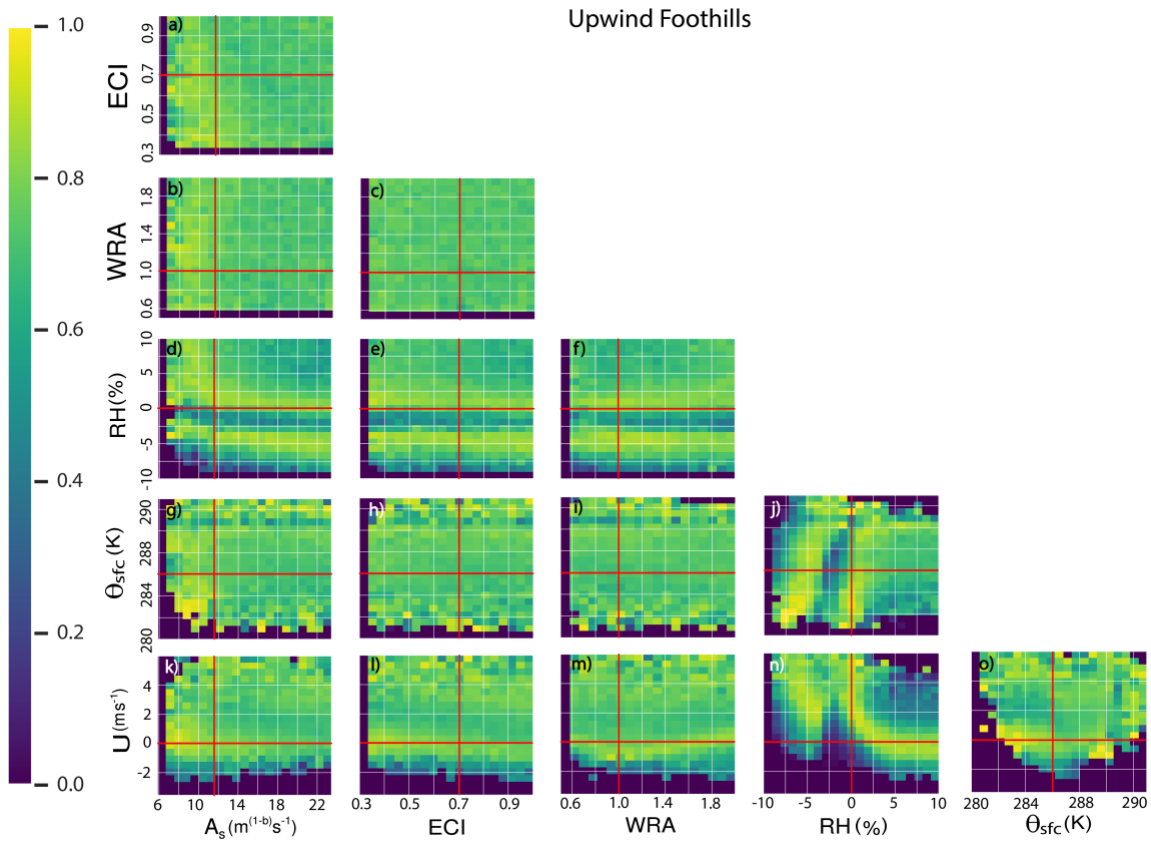

Figure 4.4 Same as Figure 4.3 but for the upwind foothills (UF) region.

In general, there is not much of a sensitivity to parameter values over the upwind slope or upwind top regions (Figure 4.5 and Figure 4.6), except for the inverse relationship between ECI and A_s. This relationship is most apparent in these regions as mixed-phase clouds exist above US and UT and most of the snow is produced here (Figure 4.2), but the three regions described

earlier do not appear in each region. The region of poor fit to the synthetic observations for smaller values of A_s exists in the 2D marginal PDF for DT (Figure 4.7).

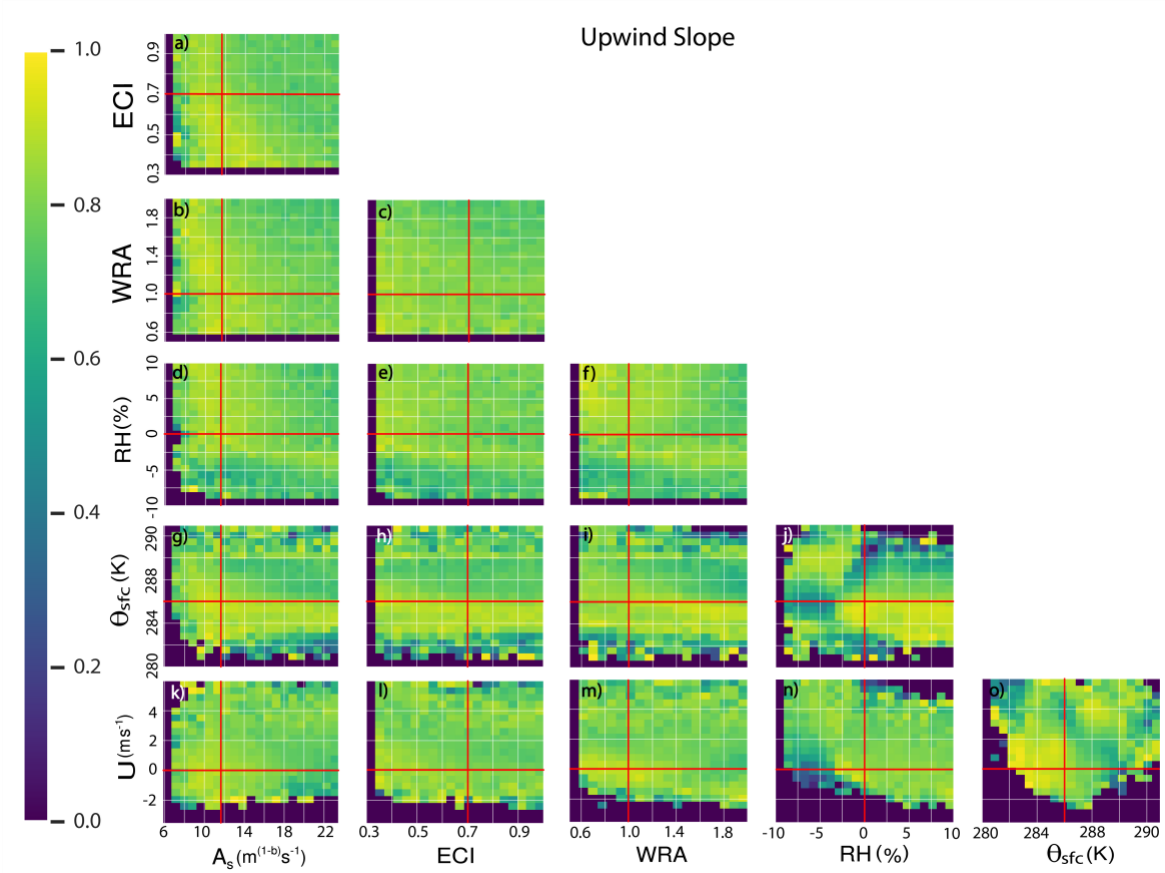

Figure 4.5 Same as Figure 4.3, but for the upwind slope (US) region.

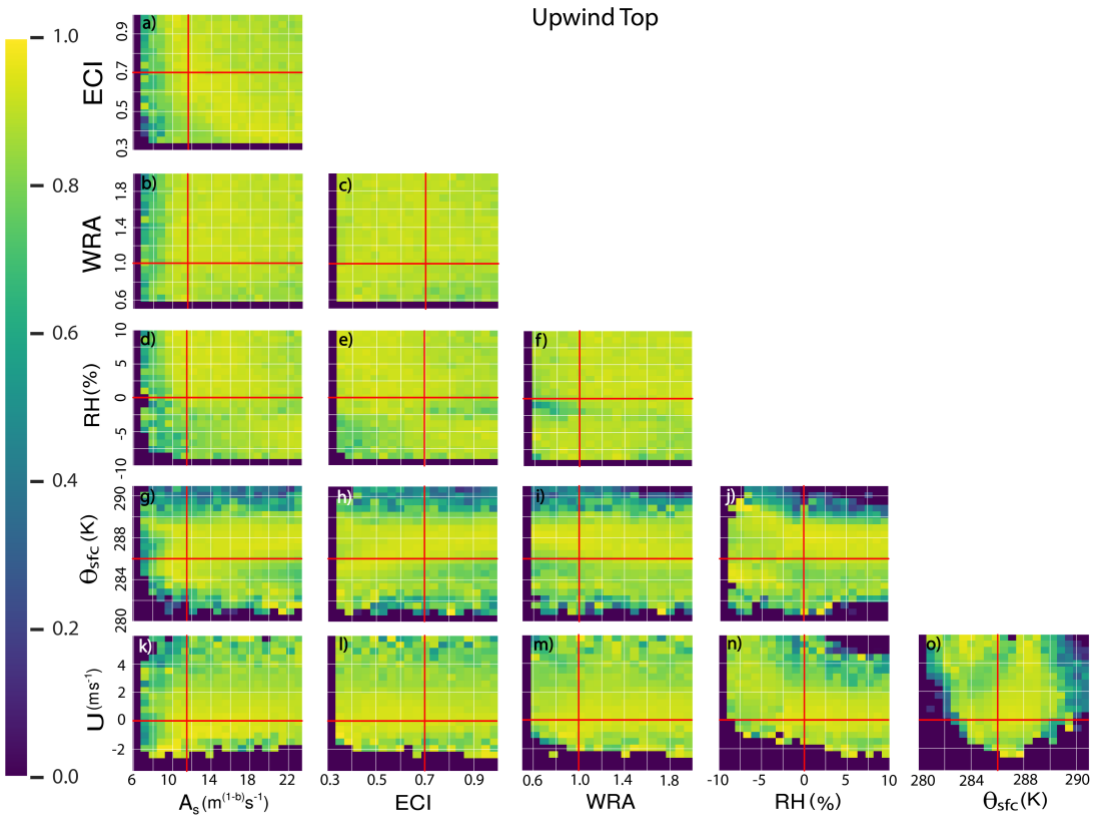

Figure 4.6 Same as Figure 4.3, but for the upwind top (UT) region.

The 2D marginal PDFs for downwind top and slope show that phase change is important to properly capturing the total precipitation distribution. Over the downwind top, there is a strong sensitivity to the value of θ_{sfc} and the positive relationship between U and A_s begins to appear (Figure 4.7). There also seems to be a better fit to RH values greater than or equal to the default value, regardless of the value of the microphysical parameters (Figure 4.7e-f). A strong sensitivity over US to wind speed values is very clear, especially when mapping U with A_s, ECI, WRA, and RH (Figure 4.8k-n). There is a strong, linear relationship between U and A_s for smaller values of A_s, which then asymptotes to a narrow range of values for U at higher A_s

values (Figure 4.8k). Physically, this relationship represents precipitation over the downwind slope being more sensitive to wind speed for large values of A_s (faster snowfall), but for slower wind speeds the value of A_s can mitigate the effects of changing U. Finally, the downwind foothills region shows most parameter combinations produce a good fit to the control precipitation distribution (Figure 4.9). This is because the precipitation uncertainty (standard deviation of likelihood distribution) for this region is relatively large compared to the total precipitation this location receives (Table 4.2).

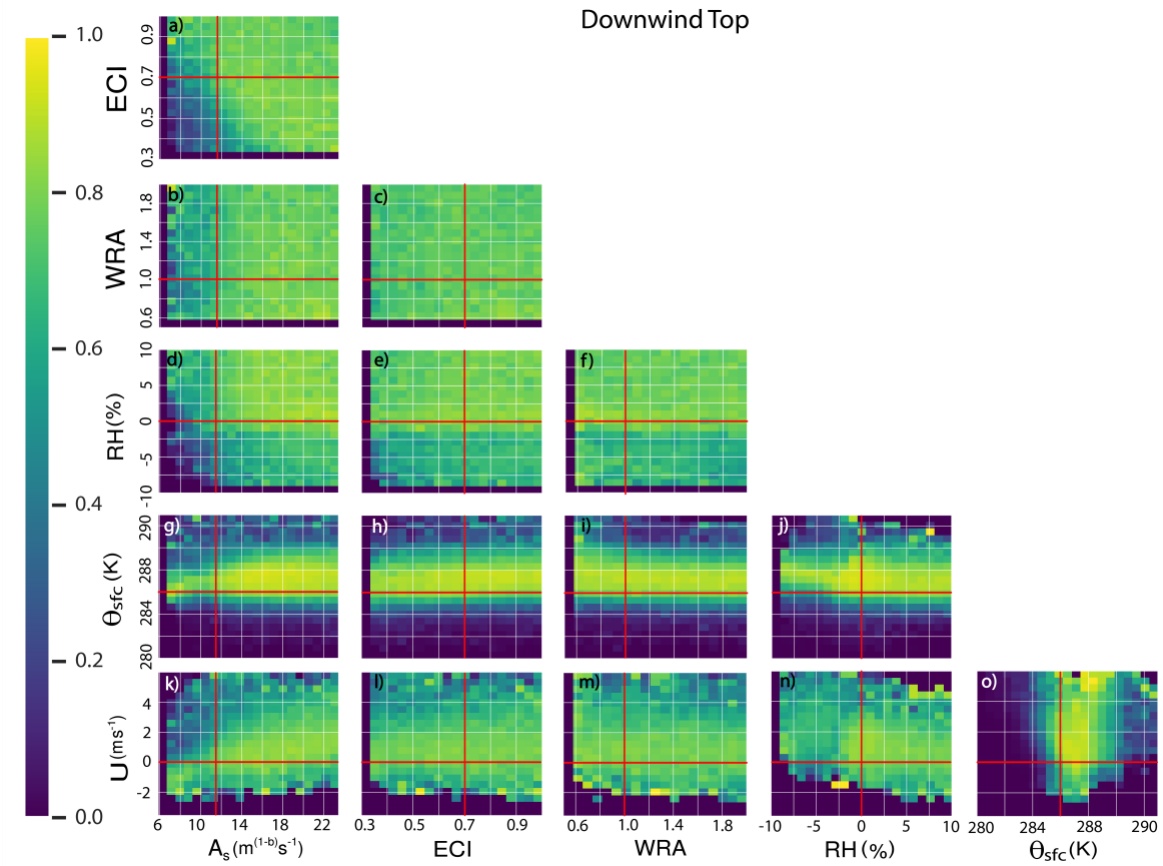

Figure 4.7 Same as Figure 4.3, but for the downwind top (DT) region.

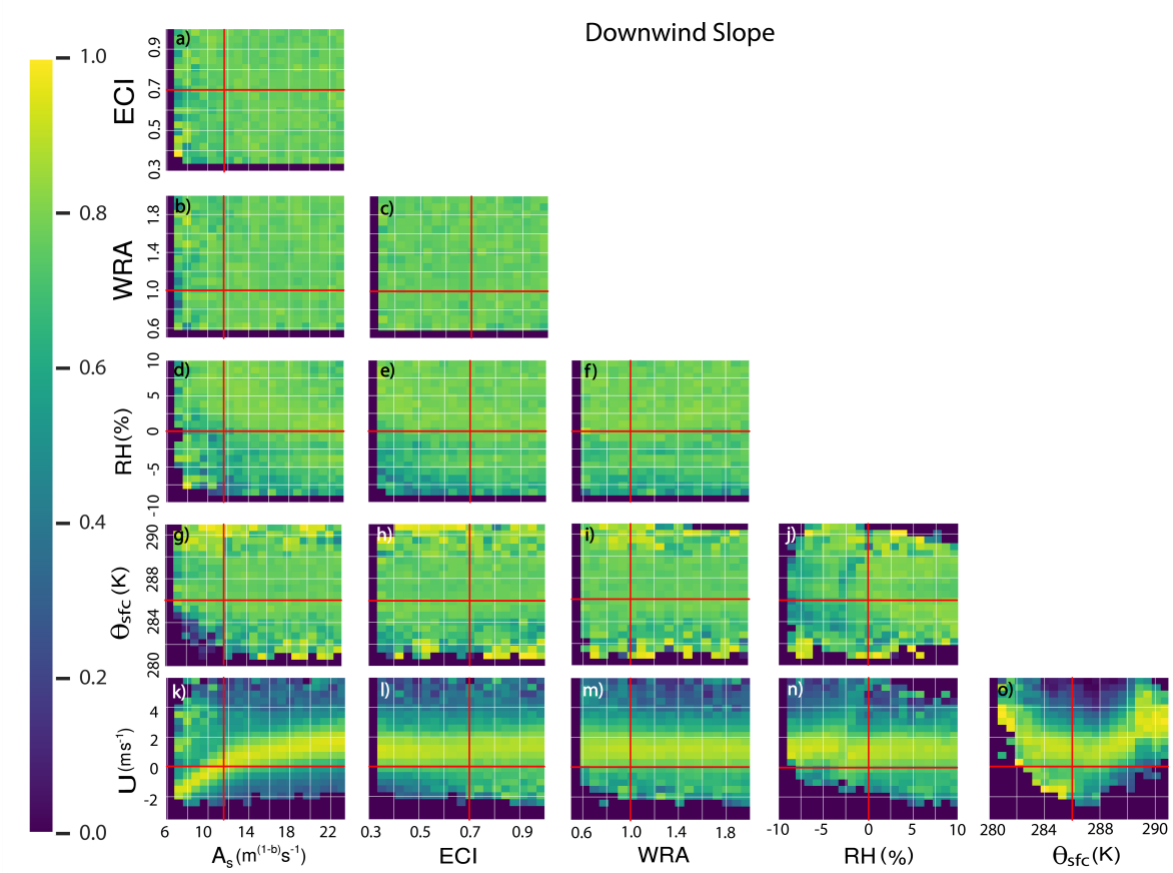

Figure 4.8 Same as Figure 4.3, but for the downwind slope (DS) region.

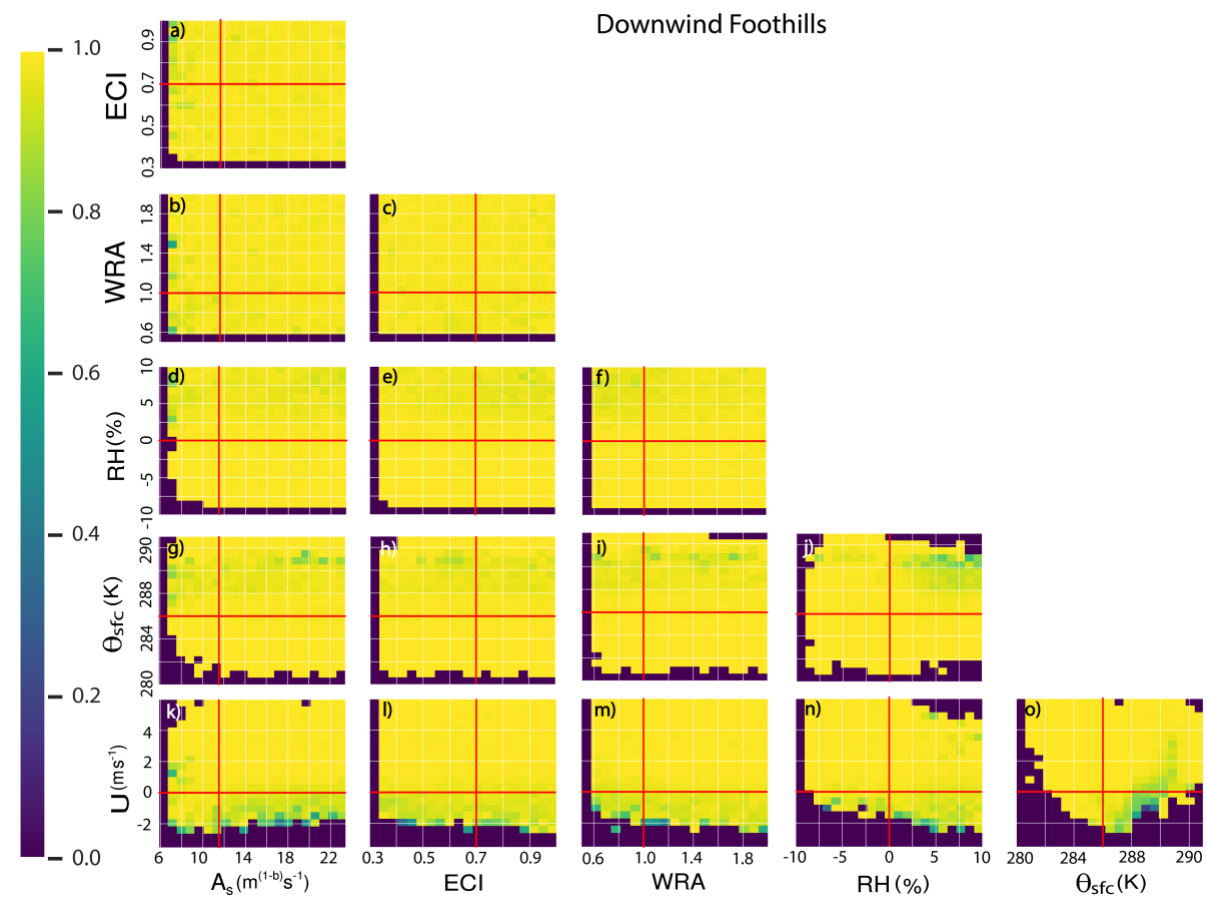

Figure 4.9 Same as Figure 4.3, but for the downwind foothills (DF) region.

Overall, MCMC results showed that for orographic precipitation from an atmospheric river environment, there does not exist a single unique set of parameter values that produce precipitation rates consistent with the control simulation. Increasing wind speed values are compensated by increasing A_s values, acting to balance the speed at which the snow falls and how fast the snow is advected horizontally. An increase in A_s is compensated by a decrease in ECI, especially for smaller values of A_s. The elongated high probability features for θ_{sfc} and the three microphysical parameters demonstrates that the precipitation rates will remain constant as

long as θ_{sfc} remains within the narrow 4 K window (Figure 4.3g-i). Strong non-linearity is found for RH results, where a very narrow range of values exist over which the probability drops substantially, and precipitation rates are no longer similar to those from the control simulation (Figure 4.3d-f). This "tipping point" is found in RH results regardless of the parameter it is compared to. Given the combination of the RH nonlinearity and the narrow range of high probability values for θ_{sfc} and U, there exists two high probability regions (Figure 4.3o). Additionally, the combination of U and θ_{sfc} shows a "bull's eye" region of high probability implying that precipitation rates will be consistent with the control only within these parameter value combinations.

Although parameter combinations were found using MCMC that were a good fit to the control precipitation rates, these same parameter values may not be a good fit if applied to a more realistic case. For example, if a three-dimensional (3D) test case was constructed and the high probability parameter sets found here were applied, the precipitation may not be reproduced due to additional flow dynamics that arise with 3D flow. The results presented here are limited to 2D idealized flow over a bell-shaped mountain using the Morrison scheme. The parameter sets found in this study may not produce the same precipitation distribution of interested if a different microphysics scheme is used, or if a different model is applied, such as the Weather Research and Forecasting model. Changes in the standard deviation values for the precipitation rates may also impact the results, as found in Tushaus et al. (2015).

Additionally, if precipitation type is used to constrain the algorithm, not just the amount of total precipitation, the resulting parameter sets may change. Therefore, the next logical step is

to understand how MCMC partitions precipitation type given that only the total precipitation amount impacts the parameter combinations.

4.4 Summary and Future Work

Orographic precipitation from atmospheric rivers is a valuable source of freshwater to communities worldwide, in addition to being potentially hazardous to life and property when flooding or landslides occur. The goals of this study were to 1) determine which combinations of microphysical and environmental parameters could yield heavy precipitation rates over the upwind slope and mountain top with similar intensities to those from a control CM1 simulation of moist, nearly neutral flow over a bell-shaped mountain and 2) identify any parameter relationships and sensitivities. To answer our science questions, idealized CM1 simulations of moist, nearly neutral flow over a bell-shaped mountain in conjunction with a Markov chain Monte Carlo (MCMC) algorithm were applied. MCMC allowed efficient and thorough exploration of the parameter space, focusing on regions with higher probabilities and avoiding regions with lower probabilities. The resulting joint posterior probability density function (PDF) was used to identify parameter co-variabilities between six microphysical and environmental parameters: snow fallspeed coefficient, ice-cloud water collection efficiency, rain accretion, horizontal wind speed, relative humidity, and surface potential temperature.

Previous methods, such as the one-at-a-time (OAT) and Morris OAT (MOAT) methods (Chapters 2 and 3), primarily used a “forward” model to determine how orographic precipitation can change given perturbations to microphysical and environmental parameters. OAT and

MOAT provide information on *which* parameters are important, i.e., result in a large change in precipitation, and not much information on parameter relationships. Additionally, the focus is on discrete parameter ranges with no probabilistic information. MCMC methods can approximate the value or distribution of values for a parameter of interest by updating the *a priori* parameter probability distribution given additional information from the model output. This approach is the basis of data assimilation and is often used to improve weather forecasts using observational data from satellites and radar.

Compared to the other regions over the mountain, the upwind slope and top appeared to have the least sensitivity to most of the parameters. This means that most parameter combinations within the discrete range of possible values can produce simulated total precipitation rates similar to those produced by the control simulation. Because moist air will always be transported perpendicular to the mountain slope, the upwind slope and top will experience condensation and sufficient time to develop precipitation that can reach these two regions.

In general, the MCMC results showed a strong sensitivity to horizontal wind speed and surface potential temperature, depicted by a narrow region of parameter values that yielded a good fit to the synthetic precipitation observations. Potential temperature was found to be most sensitive over the downwind top region, where changes to the freezing level could impact the precipitation type which could influence the particle fallspeed. Over the downwind slopes, the precipitation is very sensitive to wind speed, since the snow that develops upwind can be transported to the lee side and bring precipitation to an otherwise dry region. Additionally, a

positive relationship between wind speed and the snow fallspeed coefficient was found, emphasizing the close relationships between upstream environmental conditions and precipitation over the mountain.

The inverse relationship previously found in M19 was corroborated in the 2D marginal PDF for ice-cloud water collection efficiency (ECI) and snow fallspeed coefficient (A_s). This pair of parameters is found in equations describing the conversion of rimed snow to graupel and describing the collection of supercooled water by snow/graupel within the Morrison scheme. 2D marginal PDFs for relative humidity (RH) showed a consistent secondary maximum for RH values less than the default value, which was identified to originate over the upwind foothills region. As of writing there is no physical reason to explain this feature in the probability distribution, thus further analysis is required.

4.4.1 Next Steps

The most eye-catching, and most challenging to explain, result was the secondary maximum found in all 2D marginal PDFs with RH (Figure 4.3d-f,j,n). The analysis performed thus far has identified the upwind foothills of being the location where this sensitivity to RH occurs (Figure 4.4 d-f,j,n), but the reason behind it is unclear. The next step to understanding this peculiar feature in the 2D marginal PDFs will be to produce histograms of the other parameter values. We hypothesize that the values of the remaining 5 parameters may be important to determining the source of the probability minimum. This seems plausible, as M19 found RH to produce non-linear responses when multivariate perturbations were performed.

As described in Section 2, the MCMC algorithm is only aware of the total precipitation rates over the six regions on the mountain produced by the control simulation. Given those restrictions and the prior probability distribution for the parameters, the algorithm is allowed to produce any combination of frozen vs liquid precipitation as long as the total precipitation is close to the observations. Therefore, there *may* be instances where the CM1 model generated more or less frozen precipitation relative to the total precipitation, i.e., more precipitation reached the surface as snow/graupel compared to rain. To explore this hypothesis, the accepted parameter sets found using MCMC will be applied to the forward model (CM1) to produce a large ensemble of simulations. Two ensemble subsets are created: a subset where the frozen precipitation rates are greater than 50% of the total precipitation rates over the upwind and downwind top (FRZ), and a subset where the frozen precipitation rates are less than or equal to 50% of the total precipitation rates (LIQ). The UT and DT regions are chosen because they have the largest amount of frozen precipitation relative to the other regions. The frozen precipitation rates are 39% and 33% of the total precipitation over UT and DT in the control simulation, respectively. The simulations will then be analyzed to understand 1) if there actually exist simulations where more frozen precipitation is produced and 2) how the cloud development and environmental flow changed to produce more or less frozen precipitation. These additional experiments will be performed for the manuscript to be submitted.

Chapter 5. Conclusions and Future Work

5.1 Motivation

Over the past decade, extensive research has been performed to improve our understanding of atmospheric rivers (ARs) with the aim of improving precipitation forecasts and better quantifying precipitation uncertainty. Most ARs are beneficial to mountain regions, especially in the West Coast of the U.S., where up to half of the annual precipitation is produced by landfalling ARs (Dettinger et al. 2011). The snowpack produced at high elevations stores freshwater that then melts in the springtime and feeds rivers and reservoirs. Additionally, the rain at lower elevations can reduce or eliminate drought conditions across the agriculturally dense regions of California (Dettinger 2013; Swain et al. 2014; Eldardiry et al. 2019). However, extreme or consecutive AR events can lead to flooding, landslides, avalanches, and damage to local infrastructure (Ralph et al. 2019; White et al. 2019). These severe socio-economic impacts motivate continued research to understand the controls on precipitation from ARs interacting with mountains.

Numerical weather prediction (NWP) models include microphysical parameterizations (MPs) that represent the small-scale behavior associated with the development of clouds and precipitation and their feedbacks on the atmosphere, which cannot be resolved directly by the model. Although many sources of uncertainty exist within NWP models, the research focus for this dissertation is on microphysics, as it is closely tied to precipitation in models and can be systematically varied. As MPs have become more complex, the number of "tunable" parameters representing particle characteristics, conversion thresholds, and processes has increased. These

parameters have values which contain inherent uncertainty and natural variability yet tend to be held constant within MPs. Changes in these parameters can affect cloud development and precipitation. For example, reducing the speed at which a snow particle falls can shift maximum snowfall from the windward to lee side of a mountain (Colle and Mass 2000). Orographic precipitation sensitivities to microphysical parameter perturbations can vary for different temperature and wind speed profiles, due to different processes being activated (i.e., warm rain versus ice), and changes to the total available condensate (Colle and Zeng 2004; Miglietta and Rotunno 2006). These previous sensitivity analysis studies were limited in their exploration of the parameter space, as they did not allow for any possible parameter covariation nor systematically explore the parameter ranges. Although Tushaus et al. (2015) explored the parameter space with the use of Bayesian inference, increasing our understanding of relationships between the environment and mountain shape parameters, they did not include the effects of ice processes and used a highly simplified moisture and wind profile. The research presented here builds on past work by including ice microphysical processes and parameters, allowing for far more realistic variability in the initial wind and thermodynamic profile, and applying statistical methods to allow the simultaneous perturbation of microphysical and environmental parameters and the inclusion of parameter uncertainty.

Exploring the microphysical parameters and processes in conjunction with variations in environmental conditions will provide further information on the controls on the amount, location, and type of orographic precipitation. This dissertation greatly expands our knowledge of the controls on mountain precipitation by combining high fidelity experimental frameworks

with robust statistical sensitivity tools that have infrequently been applied to weather and climate fields.

5.2 Objectives and Methodology

Chapter 2 explores the sensitivity of precipitation to perturbations in 15 parameters associated with warm-rain and ice processes, as well as conversion thresholds and hydrometeor characteristics, such as particle density and fallspeed. The microphysical sensitivities found in this study are then tested against different environments to understand the relationships between the upstream environment and the microphysical parameters. Chapter 3 further explores these microphysical parameters and includes environmental parameters to be perturbed simultaneously to determine which parameters are most influential to orographic precipitation. This study briefly explores the influence of these parameter perturbations to the production of frozen (snow and graupel) and liquid precipitation. Additional questions are explored with this study, associated with comparing the precipitation variability generated by only perturbing parameters within a single scheme to the variability from using different microphysical schemes. Chapter 4 uses the subset of most influential parameters to precipitation to answer the inverse question: given a distribution of precipitation rates over the mountain, which combinations of parameters could have produced these precipitation rates? The covariances between parameters and further analysis of the parameter sensitivities found in the previous studies is explored. A more in depth look into the microphysical and environmental parameter impacts on precipitation type is planned for the final manuscript to be submitted for peer review.

To answer the questions proposed in each study, we use an idealized model framework with the cloud-resolving CM1 model to run numerous two-dimensional experiments of moist, nearly neutral flow over a bell-shaped mountain. This type of atmospheric stability is characteristic of an atmospheric river, resulting in heavy precipitation over the upwind slopes and mountain peaks. Idealization provides an experimental environment focused on understanding the effects of model parameter and environmental parameter changes to precipitation through effects on the microphysical and thermodynamic-kinematic processes, i.e., processes such as cloud-radiation interactions, land surface effects, and boundary layer influences are neglected. The mountain is idealized as a bell-shaped or Gaussian mountain with mountain shape parameters representative of the Olympic Mountains (Chapter 2) and the Sierra Nevada and Cascade Mountains (Chapter 3 and 4). The upwind sounding used to initialize the model and continuously feed the upstream environment is guided by a sounding taken during an AR event on 13 Nov 2015 observed during the Olympic Mountains Experiment (OLYMPEX). Using observations in the development of this idealized sounding provides additional complexity to the system, e.g., relative humidity and wind speed varies with height, that is not often found in sensitivity studies on orographic precipitation. To study the microphysical processes in the orographic system, we use the Morrison microphysics scheme with the rimed ice species set to graupel.

The methods used in this dissertation increase in complexity to build up our understanding of the physical relationships between parameters, as well as explore the core science question from different perspectives. Chapter 2 uses the commonly-used "one-at-a-time"

(OAT) method, by which one parameter is perturbed for some discrete number of values within a realistic range while keeping the rest of the parameters constant. This method allows for a detailed understanding of how parameters physically (or unphysically) affected the surface precipitation over the mountain. The relative ease of this method allowed us to explore the effect of different environments on microphysical sensitivities and allowing for a manageable number of simulations to analyze. Because this method only perturbs one parameter at a time, it is limited in providing information on possible interactions between parameters. Simultaneously perturbing all parameters would be computationally expensive, thus we employed the Morris one-at-a-time (MOAT) method in Chapter 3. The research presented in Chapter 3 is the first of its kind to apply the MOAT method to the study of orographic precipitation. MOAT provided a statistically-robust way of determining *which* perturbed parameters led to the largest changes in surface precipitation. In addition, the multivariate perturbation capabilities of MOAT provided insight on the nonlinearity of these influential parameters. Finally, the parameter subset found in Chapter 4 was used with Bayesian inference method to answer a completely different set of questions. The Markov chain Monte Carlo (MCMC) algorithm performed a random walk around the 6-dimensional parameter space, effectively avoiding regions of lower probability and frequenting regions of higher probability, resulting in a joint parameter probability distribution that combines prior parameter information with model data. MCMC randomly samples values from the parameter space, avoiding areas with lower probability and frequenting areas of relatively higher probability, where the next proposed set of values only depends on the current location within the parameter space. This Bayesian framework has been applied to orographic

precipitation before (Tushaus et al. 2015), but the study presented in Chapter 4 uses a more realistic representation of the orographic precipitation system, including ice processes, and changes to both microphysics and environmental parameters.

In general, the different methods address similar questions associated with the sensitivity of orographic precipitation to microphysical and environmental parameter perturbations. The results from using OAT in Chapter 2 created the base knowledge of how these parameters physically affected the precipitation in the microphysics scheme, while using MOAT in Chapter 3 provided a more robust analysis supporting the "more influential parameter" set found in Chapter 2. Applying MOAT allowed the statistically-robust screening of parameters that were not resulting in significant changes to precipitation, thus providing a smaller subset of parameters to be analyzed with the more complex MCMC method. The methods used in Chapter 2 and 3 use a *forward* model approach, exploring all possible parameter values and analyzing how the choice of parameter value impacts the precipitation outcome. The MCMC method applied in Chapter 4 performs an *inverse* model approach, where a specific precipitation outcome is chosen and the parameter values that could have yielded that outcome are explored. There is no discrete set of values for the parameters, instead the MCMC method uses probability distributions for each parameter to quantify the uncertainty in the parameter values.

5.3 Major Conclusions

The major conclusions found from the three studies presented in this dissertation emphasized that, to first order, the upstream moisture content and upslope flow speeds determine the total amount of condensate that will develop over a mountain. These conditions are affected

by changes to relative humidity, temperature, and horizontal wind speed, which were shown to impact updraft speeds upwind, impact precipitable water amounts, wave dynamics downwind, and horizontal transport of condensate. The total amount of precipitation falling over a mountain is more sensitive to perturbations in environmental conditions than to microphysical parameter perturbations. Nevertheless, microphysical parameters, i.e., snow fallspeed coefficient, can result in changes to precipitation of similar magnitude to changes in relative humidity, but only over the upwind slope. This emphasizes that although the environmental conditions are mainly responsible for the initial development of condensate, both microphysical and environmental parameters can be as important to orographic precipitation uncertainty.

Second order effects would be associated with changes to the freezing level, i.e., changes to the anchor surface potential temperature of the sounding. These temperature changes impact the dominant precipitation processes (warm- versus cold-rain), which can influence precipitation type, and indirectly affect the location where precipitation reaches the surface, i.e., different precipitation types will have different fallspeeds which can be transported by wind speeds differently. Overall, the most influential *environmental* parameters on precipitation rate were relative humidity (RH), horizontal wind speed (U), and surface potential temperature (θ_{sfc}). Some microphysics processes (e.g., rain accretion) influenced total condensation rates, thus illustrating the two-way connection between microphysics and thermodynamics-dynamics.

Once condensate formed in the model, the microphysics was then able to affect precipitation. For example, snow fallspeed coefficient cannot have an effect on snow if no snow forms in the first place. Perturbations to the microphysical parameters affected location of peak

precipitation rates. Parameters that directly or indirectly impact snow fallspeed induce a large sensitivity on the location of orographic precipitation. Perturbations to processes that affect the conversion of cloud water to precipitation resulted in different sensitivities to cloud development, orographic precipitation, and thermodynamics-dynamics, depending on where the cloud water is affected in the vertical. Overall, the most influential *microphysical* parameters to total precipitation were snow fallspeed coefficient (A_s), ice-cloud water collection efficiency (ECI), and rain accretion (WRA).

Strong relationships between microphysics and environmental conditions were found. Temperature regime tests showed a spatial variability of microphysical parameter sensitivities, due to changes to dominant precipitation process. For example, a lower freezing level would shift warm-rain processes farther upwind. Fewer microphysical parameters influenced precipitation in a faster wind speed environment due to a stronger dynamical forcing and different mountain-wave regime in a faster wind speed environment compared to a slower wind speed. A slower wind speed environment has similar mechanisms driving the microphysical sensitivities, but the precipitation responses to microphysics were weaker compared to the control environment. This was because weaker upslope flow resulted in weaker updrafts, which led to less available condensate for the microphysics parameters to act upon. Although microphysical parameter sensitivities changed with environment, A_s remained one of the most influential microphysics parameters regardless of environment. A_s was shown to have an inverse relationship with ECI, as both of these parameters are found in riming processes within the Morrison scheme. A positive relationship between A_s and U was found, as wind speeds would

need to increase in order to compensate for faster snowfall to yield the same precipitation rates; this relationship was strongest over the downwind slope. Additionally, different precipitation types can be influenced by different microphysical processes and parameters. More research is needed on this topic and will be continued from the research presented in Chapter 4.

Finally, variations in precipitation rates caused by perturbations to microphysical parameters within the Morrison scheme were similar in magnitude to the variation found in a four-member ensemble using different microphysics schemes.

Comparing the use of three different methodologies to answer the overarching question of how cloud processes and environmental conditions affect orographic precipitation from an atmospheric river, we can see that each method provides different information and there is no one perfect method to understand the parameter sensitivity in this system. OAT methods are most commonly used, as they are easy to apply, and the results provide information on the physical processes responsible for the changes in precipitation given the systematic parameter perturbations. Depending on how many parameters are tested and the number of parameters that are perturbed, the amount of data is a lot more manageable when compared to the use of MOAT and MCMC. The main limitation in using OAT to understand parameter sensitivities is that perturbations are performed with respect to constant values of the other parameters of interest. Given the results shown here, it is recommended that OAT methods be applied to future parameter sensitivity analysis before using more complex methods because the additional complexity can increase the amount of data produced, thus making it difficult to truly grasp the physical processes at play in the model. OAT perturbations will always have a place in

sensitivity analysis methods, but one must be careful to not overstate the results as they do not allow for possible nonlinear parameter interactions. Although the results presented in Chapter 3 showed that MOAT found a similar set of parameters to be the most influential to orographic precipitation compared to using OAT in Chapter 2, the results from using MOAT provided additional information on how parameters' impacts on precipitation can change given the values of other parameters. Although not described in Chapter 2, the results from MOAT can be further mined to understand how parameters affect precipitation, for example, do parameter perturbations lead to mostly increases/decreases in precipitation rates (monotonic changes) or can an increase and/or decrease in precipitation occur (nonmonotonic changes)? There is space for interesting and unique analysis to be performed using the standard deviation and mean of the distribution of elementary effects. In statistics, MOAT is considered a qualitative sensitivity analysis method, as it can screen out parameters that do not cause much change to a desired model output but cannot provide information on which parameter combinations work together to result in the largest change in precipitation. Most of the statistical literature recommends MOAT be used in conjunction with more complex methods, such as variance-based sensitivity analysis or MCMC.

Results from Chapter 3 showed that the snow fallspeed coefficient experienced nonlinear parameter interactions, but it was the use of MCMC in Chapter 4 that robustly showed which parameters had a relationship with the snow fallspeed coefficient and what kind of relationship it was (e.g., positive or inverse). Additionally, MCMC methods are inherently different from OAT and MOAT since MCMC focuses on a specific model outcome and determines the possible

parameter values that could have produced it (inverse modeling), as opposed to focusing on *all* possible parameter values and seeing how they impact the model outcome (forward modeling). MCMC provides further information on parameter relationships that OAT and MOAT could not provide, as well as providing probabilistic information that could be used to sample from in an ensemble forecast setting or applied to inform data assimilation efforts (e.g., which parameters can lead to the largest changes in precipitation and what observations do we need to better quantify their uncertainty?) Additionally, MCMC produces a map of the joint PDF using Bayes' theorem, and thus, can update the previously held belief of which parameter values can yield a specific model outcome given new information from model output (or observations), which is exactly what data assimilation does to improve a model forecast.

5.4 Future Work

Given the research performed in this dissertation, and the time available to complete said work, there remain various science questions to be explored and different directions that this research could be taken in. The following is a short list of ideas for future work. Some are more fleshed out than others, but all are important and interesting science questions that should be investigated.

5.4.1 Increased Model Complexity

The studies presented here focused on idealized modeling using a two-dimensional configuration, neglecting various additional physics parameterizations that may affect the system. One obvious next step would be to perform idealized studies on a three-dimensional

domain. This additional dimension would allow for testing of different flow regimes and stabilities, such as blocked flow deflected parallel to the mountain ridge or having flow travel around gaps in the terrain or an isolated mountain (such as the Olympic Mountains or mountainous islands). The level of realism could be incrementally added by having the upstream sounding be realistic and then the terrain, or vice versa.

Although mountain slope and wind direction are important controlling factors to orographic precipitation, this dissertation assumes the winds are perpendicular to the mountain slope and that for the time-scale for a given event, the mountain shape does not change. Therefore, there is opportunity to continue research using these methods to understand the effect of wind direction and mountain slope. This would be especially important for consecutive ARs that may change direction or shift in latitude, thus possibly encountering different mountain slopes. This research could aid in quantifying precipitation uncertainty given the forecast uncertainty in the location of AR landfall.

5.4.2 Case Studies and Ensemble Forecasting

Real cases of AR events could be modeled using the Weather Research and Forecasting (WRF) model. The knowledge gained from these idealized studies can be applied to real cases to determine if incorporating uncertainty/variability in the microphysical and environmental parameters is beneficial to the resulting surface precipitation. A more forecast-oriented point of view could be taken with real cases, especially if multiple observations exist to compare the model output and determine any biases. Which parameters help improve the precipitation forecast? Given results from Chapter 4, observations could be used to constrain some of the

parameters, while others will need to be constrained by proxy observations. Determining which types of observations could be combined to provide information on different parameter and process uncertainties (e.g., rain accretion and ice-cloud water collection efficiency) could be its own research project.

Current forecasting methods do not account for variability in many of the microphysical parameters, meaning forecasts may be misrepresenting the range of natural variability or may be biased in their representation of precipitation processes. To represent uncertainty from MPs, ensembles commonly use a multi-physics approach where different schemes are chosen for each ensemble member to increase the spread of uncertainty. Although multi-physics ensembles can increase ensemble spread, interpreting the results can be a challenge due to the nonlinearity of the NWP model. Results from Chapter 3 (Morales et al. 2019) demonstrated that for an idealized simulation of orographic precipitation over a two-dimensional mountain, randomly varying prescribed parameters within a single MP (multi-parameter approach) produced a standard variation of precipitation rate of similar magnitude to that from a multi-physics ensemble for different environments. Multi-parameter ensembles can allow for better interpretation of model results because these parameters are directly linked to processes or condensate characteristics within the model. Directly perturbing microphysical processes and parameters better represents the uncertainty, as different MPs tend to share common assumptions and formulations, making their behavior not entirely independent.

5.4.3 Stochastic Parameterization (and Ensemble Forecasting Continued)

Although multi-parameter ensembles include direct impacts on microphysical processes, they do not allow for spatial and temporal variations that may naturally occur. Stochastic parameterizations can add an additional level of realism to an ensemble by varying parameters spatially and temporally. Recent studies show these ensemble approaches can result in increased ensemble spread (Jankov et al. 2017, 2019), but more research needs to be done before these methods are applied operationally. We recommend future studies explore the application of stochastic parameterization to microphysical processes for orographic precipitation.

The methods used in Jankov et al. (2019) can be adapted to an orographic precipitation system using the most influential parameters from Chapter 2 and the joint parameter probability distributions from Chapter 3. An ensemble could be created using the multi-physics approach as a control to compare with the SPP approach. Ensembles are typically generated by choosing different combinations of radiation, boundary layer, land surface, and microphysics schemes. Thus, results from the SPP method can be compared to the "control" multi-physics ensemble and determine if SPP can increase ensemble spread and improve the quantification of forecast uncertainty in orographic precipitation. Forecast skill can be determined through analysis of forecast bias, spread-error relationship, and various skill scores.

5.4.4 Testing Additional Bulk Microphysical Schemes

The Thompson-Eidhammer (2014) aerosol-aware scheme is used operationally and allows for perturbations to cloud condensation and ice nuclei in addition to microphysical parameters and processes. A list of parameters associated with warm-rain, ice, and mixed-phase

processes, parameter characteristics, conversion thresholds, and aerosol parameters can be determined and used with MOAT to screen out the most important parameters, and use MCMC to determine details of parameter relationships. Uncertainty ranges for some of these parameters could be obtained from observations during the CalWater projects (Fan et al. 2014; Ralph et al. 2016; Neiman et al. 2016), which explored the influence of natural and anthropogenic aerosols on orographic precipitation during AR events.

5.4.5 Cloud-Radiative Properties

Although the results presented here focused on orographic precipitation, parameters such as WRA, ECI, and A_s also showed effects on the liquid and ice water paths (Morales et al. 2018). While cloud radiative effects are beyond the scope of this study, we suggest that future work should explore the impact of microphysical parameter perturbations on cloud optical properties and radiative transfer. The effects of radiation could be included to determine how perturbations to microphysical and environmental parameters influence outgoing longwave radiation. Additionally, parameters associated with radiation could be included to explore the impact of radiation parameterization on cloud development over mountains, for both non-convective (moist neutral or stable flows) and convective (unstable flow, diurnal effects) events.

5.4.6 Convective Orographic Events

Although moist, nearly neutral flow was the focus of this dissertation, other types of stability can be explored, such as convective instabilities from unstable flow near cold fronts or diurnally-forced orographic precipitation. The 2018 field campaign studying convective

initiation over topography in Argentina, the Remote Sensing of Electrification, Lightning, And Mesoscale/Microscale Processes with Adaptive Ground Observations (RELAMPAGO), took numerous measurements using ground observations, soundings, and radars. Data from this campaign could be used to determine a case study to which similar methods used in this dissertation could be applied. Idealized studies would be beneficial for an initial understanding of these complex storms that form in Argentina.

5.4.7 Effective Environments for Cloud Seeding

Given the capabilities of the MOAT method, and the resurgence of scientific interest in the effectiveness of anthropogenic cloud seeding, research could be proposed to investigate what type of environmental conditions are most suited for effective cloud seeding. Observations from a recent field project, the Seeded and Natural Orographic Wintertime Clouds: The Idaho Experiment (SNOWIE; Tessendorf et al. 2019) studying precipitation development during winter storms in Idaho and the influence of silver iodide on cloud seeding efforts could be used to determine case studies and compare observations to model output.

5.4.8 Climate Change Effects

In a warmer climate, how will the environmental conditions change for ARs? Will the low-level jet be faster or slower? Will there be more precipitable water available? Will the low-level air be warmer, if so, how will this change the freezing level? A study by Minder et al. (2011) showed there could be a compensating effect of warming temperatures to the deflection of the snow line towards the mountain. As the atmospheric profile becomes warmer, the melting

layer depth increases and the cooling effect from this phase change can lead to a "dipping" of the snow line and freezing level towards the mountain, resulting in cooler temperatures where the snow line deflects downward.

With a warming climate, will the large-scale circulations change such that more AR events make landfall over the West Coast during winter? What about summer ARs? Would the AR events be stronger, i.e., contain more integrated water vapor or occur for a longer period of time? Would there be a shift in location/orientation of the AR with topography? Would there be more consecutive ARs?

Hydrometeorological studies have shown a warmer climate will change the source of streamflow from snow to mostly rain (Harrell et al. 2018). How will a warmer climate affect the microphysical processes occurring in orographic clouds? Will the "seeder-feeder" (upper-level ice cloud "seeds" low-level orographic cloud through snowfall, thus enhance precipitation upwind) mechanism be reduced or enhanced? How will that impact the surface precipitation and timing of the peak stream discharge? How will that affect the available snowpack?

5.5 Applications

The orographic precipitation sensitivities to microphysical parameter perturbations found in Chapter 2 have implications to forecasting and water and hazard management. Our results show microphysical parameter perturbations have a strong influence on *where* precipitation falls, thus influencing which water basins may receive precipitation over a mountainous region. Evaluation of parameter sensitivity is important for ensemble forecasting and data assimilation, as generation of ensembles increasingly relies on perturbations to model physics as well as initial

conditions (Berner et al. 2017). It is generally not computationally feasible to perturb every parameter in the full set of model parameterization schemes, thus using the small subset of parameters found in Chapter 3 could be applied.

The MultiPhys experiment in Chapter 3 showed that variations in precipitation rates caused by perturbations to microphysical parameters within the Morrison scheme was similar in magnitude to the variation found in a four-member ensemble using different microphysics schemes. A common method to account for uncertainty in the representation of microphysics in numerical weather prediction is to create ensembles where each member uses a different combination of physics schemes, including microphysics (e.g., Eckel and Mass 2005; Xue et al. 2009; Schwartz et al. 2010; Clark et al. 2011; Johnson and Wang 2012, 2013). The results presented herein hint that similar variability can be achieved by varying parameters within a single scheme for orographic precipitation cases, particularly when the choice of most influential parameters to vary is informed by statistical analysis as in our study using the MOAT method. Multi-parameter ensembles are potentially advantageous because physical interpretation of differences among ensemble members is straightforward, unlike for multi-physics scheme ensembles in which numerous processes and parameters are represented differently among schemes. Observational studies have shown a systematic overprediction of orographic precipitation during cold wintertime storms, i.e., storms whose freezing level exists below the average mountain height (Lin et al. 2013). This positive model bias is thought to be related to the representation of ice processes within bulk microphysics schemes and thermodynamic/dynamic processes that can affect these processes (Lin et al. 2013). Thus, including microphysical

parameters in ensemble forecasting through stochastic parameterization may lead to an improvement in these model biases.

The joint posterior probability distributions produced by MCMC were used to understand relationships between parameters, precipitation sensitivity to changes in parameters, and uniqueness of model solutions. This information can be applied to ensemble forecasting to help determine which parameters should be included and perturbed in the ensemble. Understanding any parameter co-variabilities is important for model development and forecasting. ARs occur worldwide, and thus, results from this study can have global applications to orographic precipitation. Additionally, moist neutral flow conditions are not restricted to AR events; these atmospheric conditions can be found within the inner regions of a hurricane (Houze 2010), which often make landfall near mountainous regions in the southeastern US and over mountainous islands in the Caribbean.

The methods applied here (MOAT and MCMC) can be used to explore the sensitivity of liquid, ice, and supercooled water path, and outgoing longwave/shortwave radiation to changes in microphysics, aerosol, and environmental conditions in a statistically robust and computationally efficient manner. Results can then be applied to climate studies of cloud-radiative transfer, and aircraft icing and solar energy prediction. The parameter sensitivity analysis performed in this dissertation can also help future field campaigns focus on observing key processes to better constrain their uncertainty and improve our understanding.

Appendix. Cloud Number Concentration Tests

Cloud number concentrations represent the number of cloud water droplets that will develop within a cubic centimeter of air. In the Morrison scheme, as well as many other bulk schemes that do not include aerosols, changes to the cloud number concentration (N_c) are a proxy for changes to cloud condensation nuclei (CCN). It assumed that the value for N_c represents the number of "activated" CCN in a cubic centimeter of air once saturation is reached, through cooling or an increase of moisture content. A study by Saleeby et al. (2009) suggested that increased concentrations of aerosols acting as CCN could lead to a suppressing effect, i.e., less precipitation, and a delaying effect, precipitation initiation is delayed in time, on precipitation. Therefore, it is hypothesized that increased number concentrations for cloud droplets will lead to smaller cloud droplets, which will require more time to grow large enough to precipitate. Lower values of number concentrations will cause larger cloud droplets to form, as more water vapor will be available to condense on fewer cloud droplets, leading to faster rain initiation.

CM1 model simulations were performed using the control upstream sounding and mountain geometry used in Chapter 3 (M19). The simulation was run for 20 hours and results focus on temporal averages from hours 6-20, when the system is quasi-stable, and the cloud and precipitation development and wind flow are generally constant. The results were analyzed for six regions on the bell-shaped mountain, three upwind and three downwind (see Chapter 2). The goal of these experiments was to explore the sensitivity of orographic precipitation from a moist

neutral environment to changes in N_c. This work was first performed by Christine Soh, a summer intern in the Pre-College Internship Program at NCAR in 2015 but used a different upstream environment. Five values of N_c were tested: 50 cm^{-3}, 200 cm^{-3}, 400 cm^{-3}, 550 cm^{-3}, and 750 cm^{-3}. This range of values represent clean maritime air on the low end to relatively clean continental air on the high end (Rogers and Yau 1989), i.e. a truly polluted air mass could be upwards of 2000 cm^{-3} and was not tested. The number of cloud water droplets available can influence warm-rain processes, such as autoconversion (cloud self-collection converted to rain) and rain accretion (cloud water collection by rain drops), and ice processes, such as riming (collection of supercooled droplets by ice) and the Wegner-Bergeron-Findeisen process. The value used in the microphysical and environmental parameter sensitivity studies in Chapters 2, 3, and 4 was 200 cm^{-3} (default value), thus this value will be treated as the control and its results will be compared to those for the other four N_c values.

Hovmöller diagrams for the control simulation using N_c=200 cm^{-3} show an initial maximum where snow, rain, and graupel develop simultaneously (Figure A.1). After the initial maximum, the highest total precipitation rates occur over the upwind top and downwind top, with liquid precipitation seemingly forming through warm-rain processes upwind, and melting of frozen precipitation over the downwind top region (Figure A.1a,b). The frozen precipitation is continuous and approximately centered over the mountain peak (Figure A.1c).

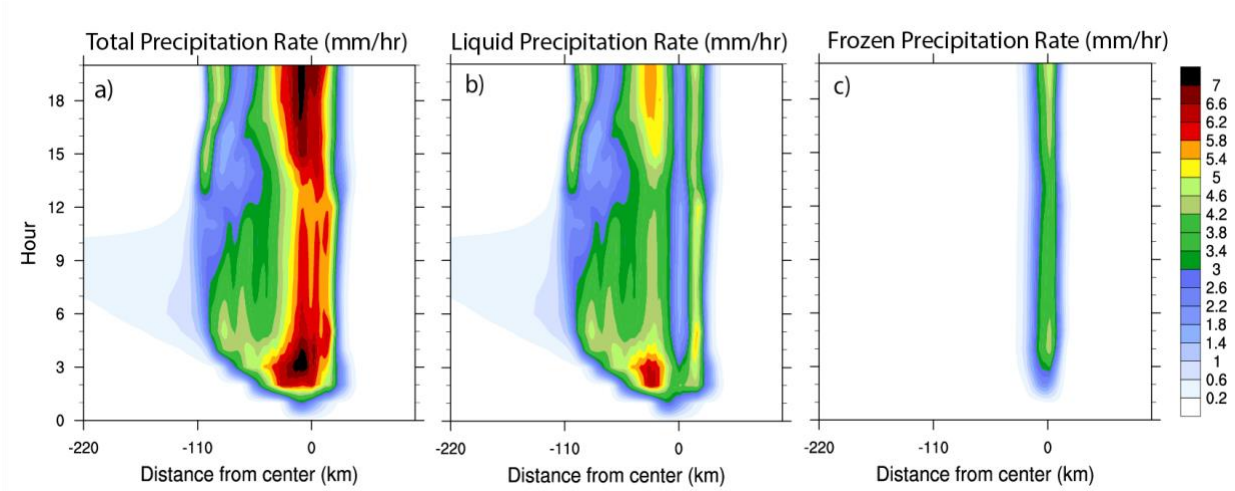

Figure A.1 Hovmöller diagrams of (a) total (liquid+frozen), (b) liquid, and (c) frozen precipitation rates (mm/hr) for the control simulation using a cloud number concentration of 200 cm^{-3}.

Comparing the total precipitation rates for the control simulation to the experiments with different values of N_c show that for the lowest N_c value an increase in precipitation rates occurs early in the simulation and a positive bias is found farther upwind compared to the control (Figure A.2a). For about the first half of the simulation, results between the control and N_c = 400 cm^{-3} are not too different, but later into the simulation the differences increase and the total precipitation shifts toward the upwind slope (Figure A.2b). Results for N_c = 550 cm^{-3} and 750 cm^{-3} show similar differences in total precipitation rate compared to the control (Figure A.2c,d). In general, as the number concentration of cloud water droplets is increased, precipitation formation is seemingly delayed and a lot less precipitation occurs over the upwind foothills.

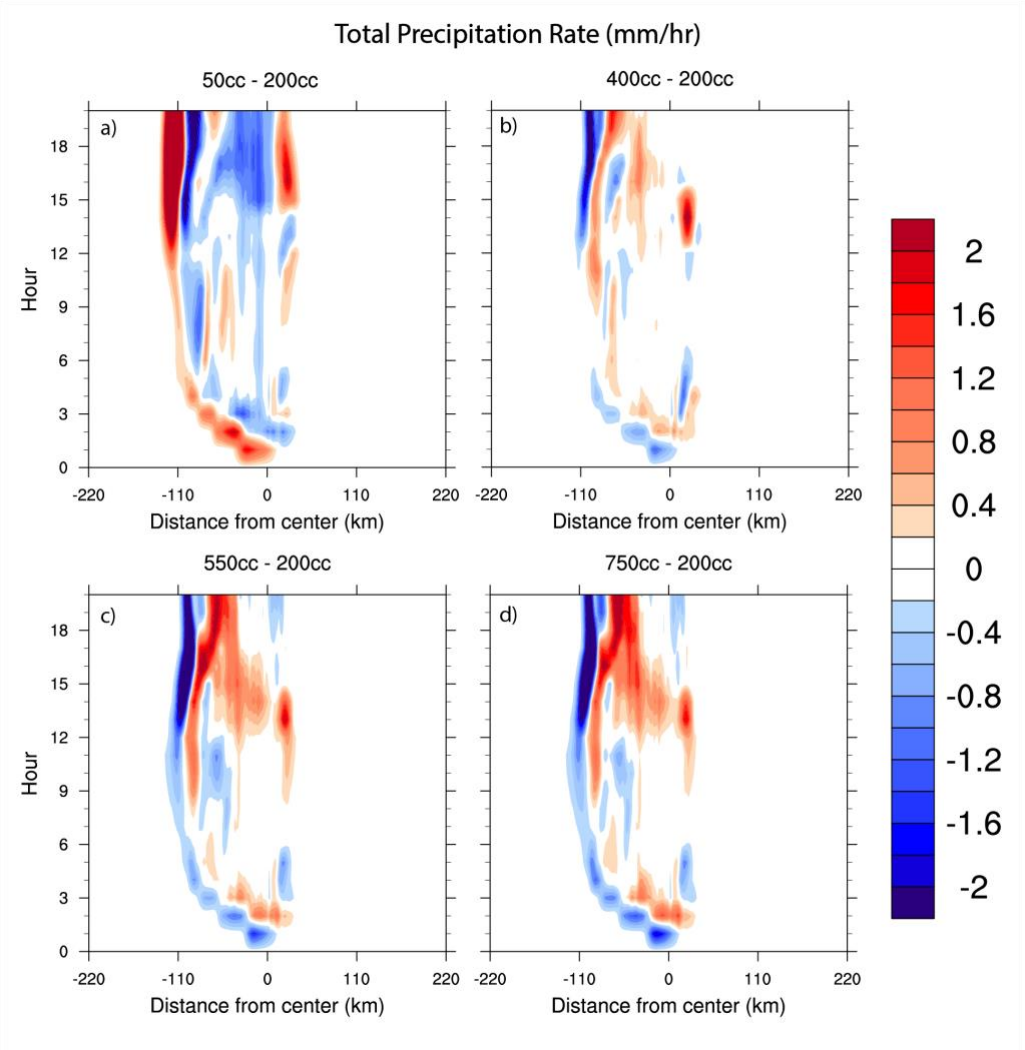

Figure A.2 Hovmöller diagrams of differences in total precipitation rate (mm hr^{-1}) between (a) 50 cm^{-3}, (b) 400 cm^{-3}, (c) 550 cm^{-3}, and (d) 750 cm^{-3} and the control (200 cm^{-3}).

Focusing on frozen precipitation rates, which include snow and graupel reaching the surface, shows small differences (max ~1.2 mm hr^{-1}) between the control and the N_c experiments (Figure A.3). For the small value of N_c less frozen precipitation occurs over the upwind top, with more frozen precipitation developing after hour 15 over the downwind top region (Figure A.3a). As for the larger values of N_c, there exist three time periods with differences in frozen

precipitation: hours 1-5, hours 12-15, and hours 18-20 (Figure A.3b,c,d). The second period has a wider spatial extent and relatively larger frozen precipitation differences.

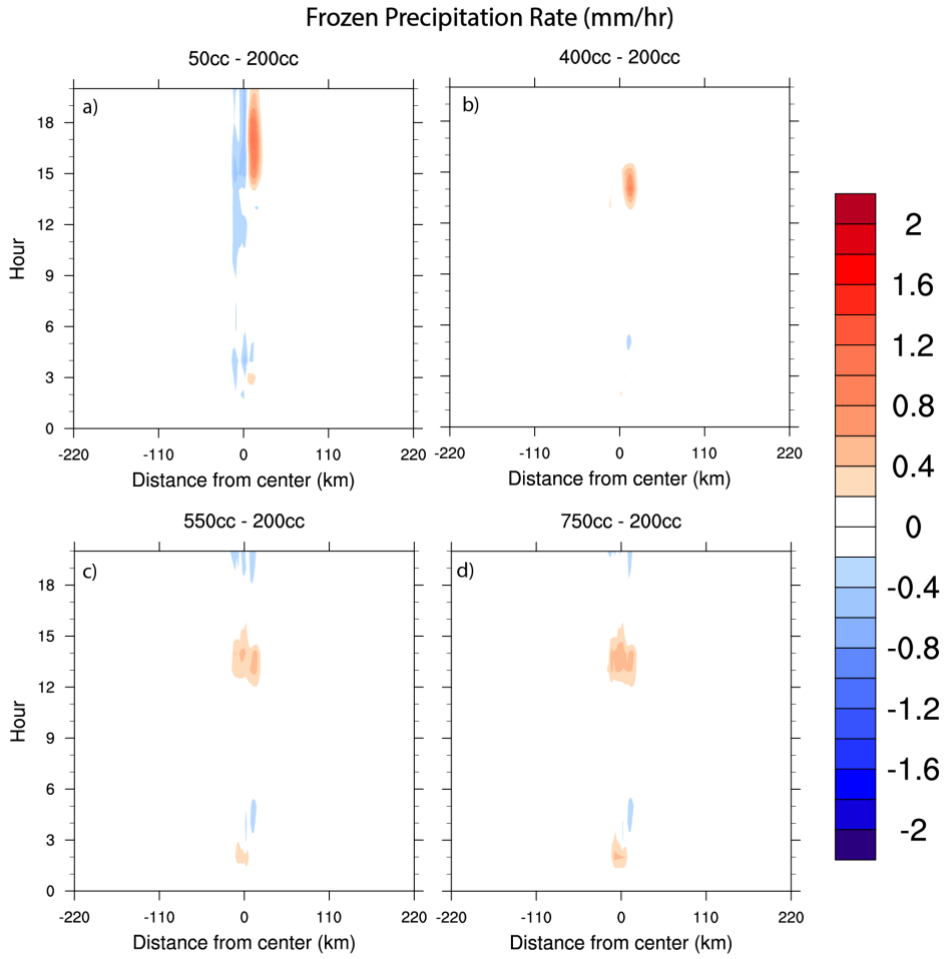

Figure A.3 Same as Figure A.2, except for frozen precipitation rates (mm hr^{-1}).

Spatially averaging the total precipitation rates over the six locations on the mountain show that for all simulations the peak precipitation rates occur on the upwind top (Figure A.4a). Over the upwind foothills the small N_c experiment has the larger precipitation rates, demonstrating that this experiment develops total precipitation earlier. This may be because

larger cloud droplets develop, which can grow faster through collision-coalescence within the warm region (above freezing) of the cloud. Over the upwind top, the small N_c experiment had much less total precipitation rates compared to the other N_c experiments. Over the downwind regions there are less differences between the experiments, mainly because there is either less precipitation produced there (downwind slope and foothills). In general, the four larger N_c experiments produce similar total precipitation amounts, with a larger spread between the experiments over the upwind slope (Figure A.4a).

Analyzing the frozen and liquid precipitation rates separately, the results show a larger spread in the precipitation rates over the upwind slope and top for liquid precipitation than frozen precipitation (Figure A.4b). These results are not surprising, as changing the cloud droplet amounts should directly impact the development of liquid precipitation. The ranges of N_c tested do not show a substantial change to the frozen precipitation, except for the lowest N_c value of 50 cm^{-3} (Figure A.4c).

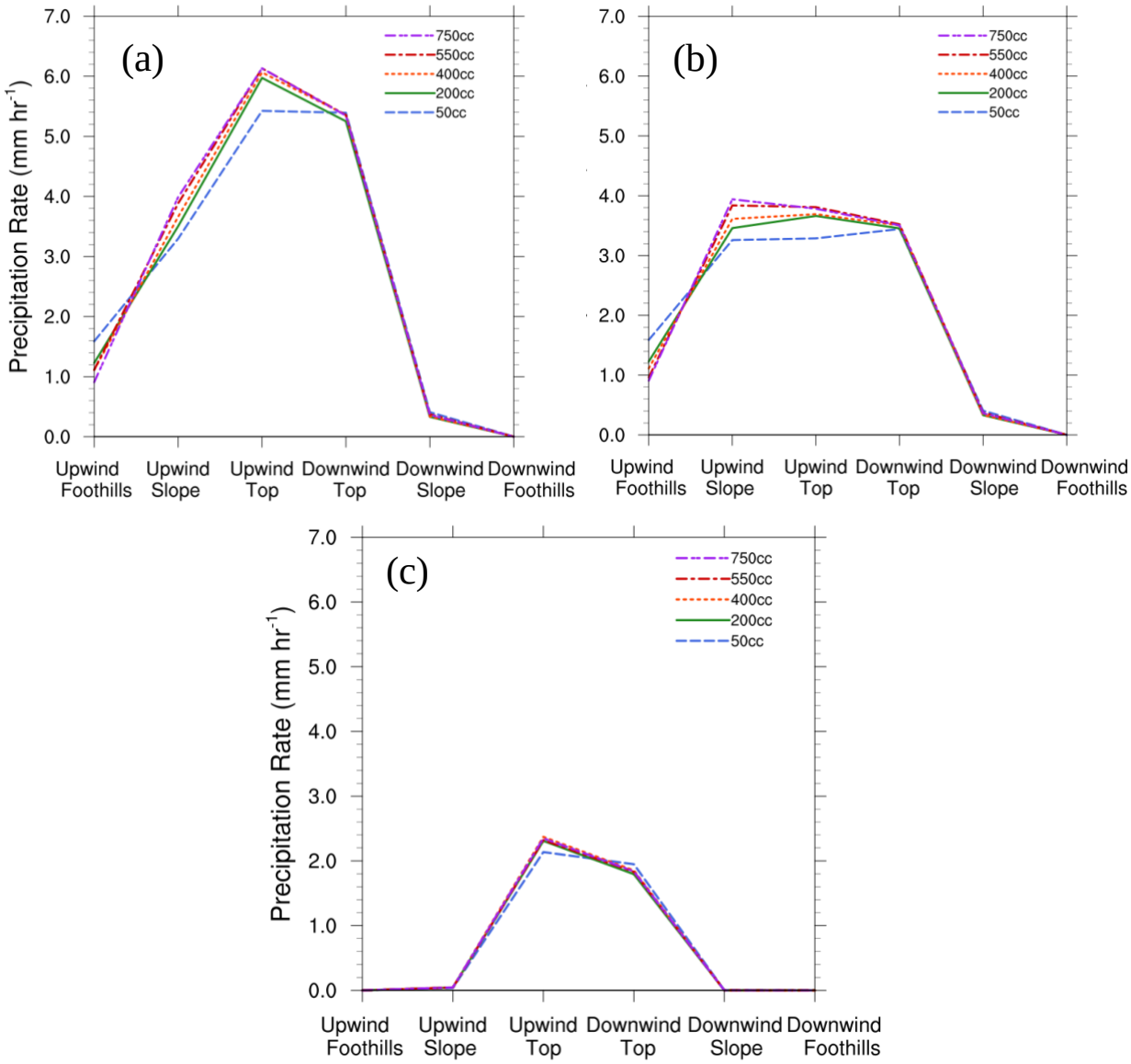

Figure A.4 Precipitation rate (mm hr^{-1}) temporally-averaged over hours 6-20 and spatially-averaged over six regions over the mountain for (a) total precipitation, (b) liquid precipitation, and (c) frozen precipitation. Each line represents a different value of cloud water number concentration: 750 cm^{-3} (purple, dash-dot-dot line), 550 cm^{-3} (red, dash-dot line), 400 cm^{-3} (orange, dotted line), 200 cm^{-3} (green, solid line), and 50 cm^{-3} (blue, dashed line).

The results from the different N_c or CCN ensemble (DiffCCN) are compared to those from Chapter 3 (Morales et al. 2019), i.e., precipitation changes due to microphysical and

environmental parameter (MP_ENV) and microphysics-only (MultiParam) perturbations using the MOAT method, to determine if perturbations to CCN result in relatively similar changes to orographic precipitation. Overall, CCN perturbations over the range explored in this study impact the mean value of precipitation rates, especially over the mountain top, more than perturbations in microphysics or microphysics and environment (Figure A.5a). The addition of environmental parameters actually the average precipitation rate values over US, UT, and DT, compared to only perturbing the microphysical parameters (Figure A.5a). Although the precipitation rates are larger on average, the standard deviation of the DiffCCN ensemble is much smaller compared to that of MP_ENV and MultiParam, especially over UT, DT, and DS (Figure A.5b). The addition of environmental parameters is shown to actually increase the standard deviation in the ensemble, with the largest differences occurring over UF and DT (Figure A.5b). Given these locations and the results from Chapter 3 and 4, it is hypothesized that these changes are due to horizontal wind speed perturbations.

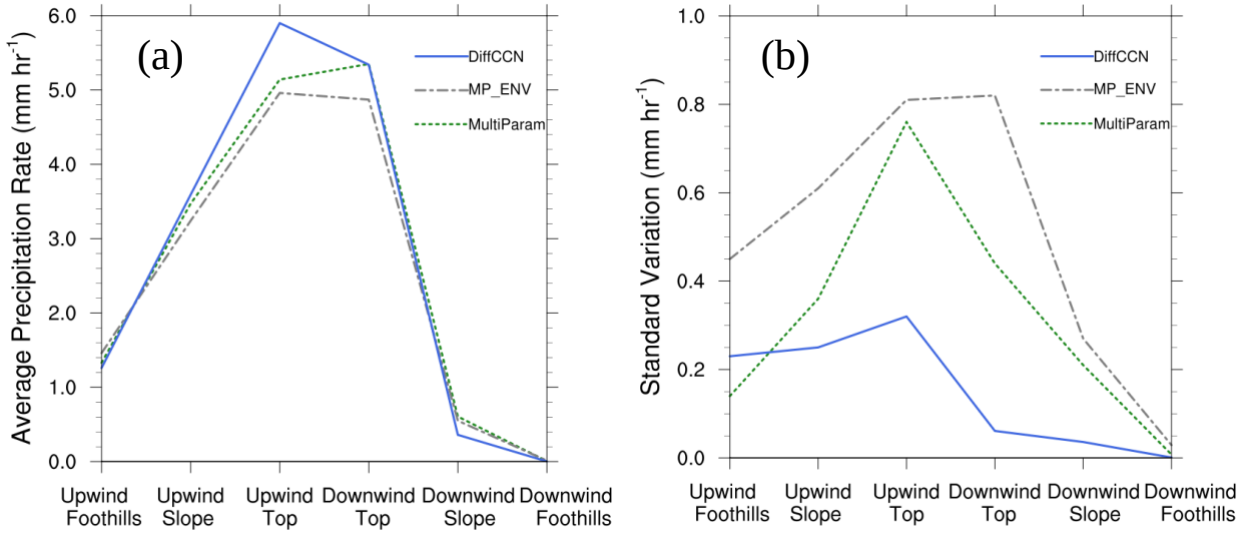

Figure A.5 (a) Average precipitation rates and (b) standard deviation values for the CCN ensemble (DiffCCN, solid blue line), MP_ENV ensemble from Chapter 3 (dot-dashed gray line), and MultiParam ensemble from Chapter 3 (dotted green line) over the six mountain regions.

To summarize, changing the number concentration of cloud droplets showed a delay in the precipitation initiation as N_c values were increased. Changes to N_c affected liquid precipitation at the surface more so than frozen precipitation. Since both warm-rain and ice-processes can lead to liquid precipitation, more analysis is needed to understand the influence of N_c to the formation of snow and graupel. Perturbations to the N_c values can result in larger average changes to the liquid precipitation over the mountain top, but the precipitation values are generally similar between ensemble members in DiffCCN (smaller standard deviation of ensemble).

It would be useful to explore any differences in microphysical process rates in the vertical, to determine where exactly these N_c effects are most important. A more thorough

analysis of frozen precipitation processes would help to better explore the possible connection between CCN and riming. An examination of the vertical cross-sections for each simulation would be useful to further understand the precipitation results. These results also motivate the testing of higher N_c values, as well as testing of the Thompson-Eidhammer (2014) aerosol-aware scheme – this scheme would allow for the testing of the impact of the ice nuclei concentration to orographic precipitation.

References

American Meteorological Society, cited 2012: Hail. Glossary of Meteorology. [Available online at http://glossary.ametsoc.org/wiki/Hail]

American Meteorological Society, cited 2019: Atmospheric river. Glossary of Meteorology. [Available online at http://glossary.ametsoc.org/wiki/Atmospheric_river]

Anders, A. M., G. H. Roe, B. Hallet, D. R. Montgomery, N. J. Finnegan, and J. Putkonen, 2006: Spatial patterns of precipitation and topography in the Himalaya *in* Willett, S. D., N. Hovius, M. T. Brandon, and D. Fisher, eds., Tectonics, Climate, and Landscape Evolution: Geological Society of America Special Paper 398, 39-53.

Avila, R., and S. S. Raza, 2005: Dispersion of particles released into a neutral planetary boundary layer using a Markov chain-Monte Carlo model. *Journal of Applied Meteorology*, **44**, 1106-1115.

Berner, J., and Coauthors, 2017: Stochastic parameterization: Toward a new view of weather and climate models. *Bull. Amer. Meteor. Soc.*, **98**, 565-588.

Bergeron, T., 1935: On the physics of cloud and precipitation. Proc. 5th Assembly U.G.G.I. Lisbon. Vol. 2, p. 156.

Bergeron, T., 1965: On the low level redistribution of atmospheric water caused by orography. *Supp. Proc. Int. Conf. Cloud Phys.*, 96-100.

Bryan, G. H., and J. M. Fritsch, 2002: A benchmark simulation for moist nonhydrostatic numerical models. *Mon. Wea. Rev.*, **130,** 2917-2928.

Caine, N., 1980: The rainfall intensity: Duration controls on shallow landslides and debris flows. *Geogr. Ann. Ser.*, **A 62**, 23-27.

Campolongo, F., J. Cariboni, and A. Saltelli, 2007: An effective screening design for sensitivity analysis of large models. *Environmental Modelling and Software*, **22**, 1509-1518.

Castellano, N. E., E. E. Avila, and C. P. R. Saunders, 2004: Theoretical model of the Bergeron-Findeisen mechanism of ice crystal growth in clouds. Atmospheric Environment, **38**, 6751-6761.

Clark, A. J., and Coauthors, 2011: Probabilistic precipitation forecast skill as a function of ensemble size and spatial scale in a convection-allowing ensemble. *Mon. Wea. Rev*., **139**, 1410-1418.

Colle, B. A., and C. F. Mass, 2000: The 5-9 February 1996 flooding event over the Pacific Northwest: Sensitivity studies and evaluation of the MM5 precipitation forecasts. *Mon. Wea. Rev.*, **128**, 593-617.

Colle, B. A., 2004: Sensitivity of orographic precipitation to changing ambient conditions and terrain geometries: An idealized modeling perspective. *J. Atmos. Sci.*, **61**, 588-606.

Colle., B. A., and Y. Zeng, 2004a: Bulk microphysical sensitivities within the MM5 for orographic precipitation. Part I: The Sierra 1986 event. *Mon. Wea. Rev*., **132**, 2780-2801.

Colle., B. A., and Y. Zeng, 2004b: Bulk microphysical sensitivities within the MM5 for orographic precipitation. Part II: Impact of barrier width and freezing level. *Mon. Wea. Rev*., **132**, 2802-2815.

Colle, B. A., M. F. Garvert, J. B. Wolfe, C. F. Mass, and C. P. Woods, 2005: The 13-14 December 2001 IMPROVE-2 Event. Part III: Simulated microphysical budgets and sensitivity studies. *J. Atmos. Sci*., **62**, 3535-3558.

Conway, H., and C. F. Raymond, 1993: Snow stability during rain. *J. Glacial.*, **39**, 635-642.

Covey, C., D. D. Lucas, J. Tannahill, X. Garaizar, 2013: Efficient screening of climate model sensitivity to a large number of perturbed input parameters. *J. Adv. Model. Earth Syst*., **5**, 598-610.

Curry, C. L., S. U. Islam, F. W. Zwiers, and S. J. Déry, 2019: Atmospheric rivers increase future flood risk in Western Canada's largest Pacific River. *Geophys. Res. Lett*., **46**.

Daly, C., M. Halbleib, J. I. Smith, W. P. Gibson, M. K. Doggett, G. H. Taylor, J. Curtis, and P. P. Pasteris, 2008: Physiographically sensitive mapping of climatological temperature and precipitation across the conterminous United States. *Int. J. Climatol.*, **28**, 2031-2064.

Delle Monache, L., and CoAuthors, 2008: Bayesian inference and Markov chain Monte Carlo sampling to reconstruct a contaminant source on a continental scale. *Journal of Applied Meteorology and Climatology*, **47**, 2600-2613.

Dettinger, M., K. Redmond, and D. Cayan, 2004: Winter orographic precipitation ratios in the Sierra Nevada -- Large-scale atmospheric circulations and hydrologic consequences. *J. Hydromet*., **5**, 1102-1116.

Dettinger, M. D., F. M. Ralph, T. Das, P. J. Neiman, and D. R. Cayan, 2011: Atmospheric rivers, floods and the water resources of California. *Water*, **3**, 445-478.

Dettinger, M. D., and B. L. Ingram, 2013: The coming megafloods. *Scientific American*, January 2013, 64-71.

Doyle, J. D., and Coauthors, 2000: An intercomparison of model-predicted wave breaking for the 11 January 1972 Boulder windstorm. *Mon. Wea. Rev.*, **128**, 901-914.

Durran, D. R., and J. B. Klemp, 1982: On the effects of moisture on the Brunt-Väisälä frequency. *J. Atmos. Sci*., **39**, 2152-2158.

Durran, D. R., 1990: *Atmospheric Processes over Complex Terrain. Meteor. Monogr.*, Amer. Meteor. Soc., No. 45, 394 pp.

Eckel, F. A., and C. F. Mass, 2005: Aspects of effective mesoscale, short-range ensemble forecasting. *Wea. Forecasting*, **20**, 328-350.

Eldardiry, H., A. Mahmood, X. Chen, F. Hossain, B. Nijssen, and D. P. Lettenmaier, 2019: Atmospheric river-induced precipitation and snowpack during the Western United States cold season. *J. Hydrometeorology*, **20**, 613-630.

Elsner, J. B., X. Niu, and T. H. Jagger, 2004: Detecting shifts in hurricane rates using a Markov chain Monte Carlo approach. *Journal of Climate*, **17**, 2652-2666.

Fan, J., and CoAuthors, 2014: Aerosol impacts on California winter clouds and precipitation during CalWater 2011: local pollution versus long-range transported dust. *Atmos. Chem. Phys.*, **14**, 81-101.

Findeisen, W., 1938: Die kolloidmeteorologischen Vorgänge bei der Niederschlagsbildung (Colloidal meteorological processes in the formation of precipitation). Met. Z.. 55. p. 121.

Florsheim, J. L., and M. D. Dettinger, 2007: Climate and floods still govern California levee breaks. *Geophys. Res. Lett.*, **34**, L22403.

Frei, C. and Schär, C., 1998: A precipitation climatology of the Alps from high-resolution rain-gauge observations. *Int. J. Climatol.*, **18**, 873-900.

Gilmore, M. S., J. M. Straka, and E. N. Rasmussen, 2004a: Precipitation and evolution sensitivity in simulated deep convective storms: Comparisons between liquid-only and simple ice and liquid phase microphysics. *Mon. Wea. Rev.*, **132**, 1897-1916.

Gilmore, M. S., J. M. Straka, and E. N. Rasmussen, 2004b: Precipitation uncertainty due to variations in precipitation particle parameters within a simple microphysics scheme. *Mon. Wea. Rev.*, **132**, 2610-2627.

Gochis, D., and Coauthors, 2015: The Great Colorado Flood of September 2013. *Bull. Amer. Meteor. Soc*., **96**, 1461-1487.

Gorodetskaya, I. V., M. Tsukernik, K. Claes, M. F. Ralph, W. D. Neff, and N. P. M. Van Lipzig, 2014: The role of atmospheric rivers in anomalous snow accumulation in East Antarctica, *Geophy. Res. Lett.*, **41**, 6199-6106.
Guan, B., N. P. Molotch, D. E. Waliser, E. J. Fetzer, and P. J. Neiman, 2010: Extreme snowfall events linked to atmospheric rivers and surface air temperature via satellite measurements. *Geophys. Res. Lett.*, **37**, L20401.

Guan, B., N. P. Molotch, D. E. Waliser, E. J. Fetzer, and P. J. Neimen, 2013: The 2010/2011 snow season in California's Sierra Nevada: Role of atmospheric rivers and modes of large-scale variability. *Water Resour. Res*., **49**, 6731-6743.

Guan B., and D. E. Waliser, 2015: Detection of atmospheric rivers: Evaluation and application of an algorithm for global studies. *J. Geophys. Res. Atmos.*, **120**, 12,514-12,535.

Guerra, L., and CoAuthors, 2016: Climate change evidence from the end of the Little Ice Age to the current warm period registered by Melincué Lake (Northern Pampas, Argentina). *Quaternary International,* 1-15.

Hagos, S., L. R. Leung, Q. Yang, C. Zhao, and J. Lu, 2015: Resolution and dynamical core dependence of atmospheric river frequency in global model simulations. *J. Climate*, **28**, 2764-2776.

Harrington, J. Y., K. Sulia, and H. Morrison, 2013: A method for adaptive habit prediction on bulk microphysical models. Part I: Theoretical development. *J. Atmos. Sci.*, **70**, 349-364.

Harrell, J., A. Wood, and M. Clark, 2018: Predicting streamflow and snowpack sensitivities to climate change in the Pacific Northwest's Green River Basin. Significant Opportunities for Atmospheric Research and Science (SOARS) program. Available at: https://opensky.ucar.edu/islandora/object/manuscripts%3A980

Hobbs, P. V., R. C. Easter, and A. B. Fraser, 1973: A theoretical study of the flow of air and fallout of solid precipitation over mountainous terrain: Pat II: Microphysics. *J. Atmos. Sci.*, **30**, 813-823.

Houze, R. A., Jr., 2010: Clouds in Tropical Cyclones. *Mon. Wea. Rev.*, **138**, 293-344.

Houze, R. A., Jr., 2012: Orographic effects on precipitation clouds. *Rev. Geophys*., **50**, RG1001.

Houze, R. A., Jr., and Coauthors, 2017: The Olympic Mountains Experiment (OLYMPEX). *Bull. Amer. Meteor. Soc.*, **98**, 2167-2188.

Jankov, I., P. J. Schultz, C. J. Anderson, and S. E. Koch, 2007: The impact of different physical parameterizations and their interactions on cold season QPF in the American River Basin. *J. Hydrometeor.*, **8**, 1141- 1151.

Jankov, I., J.-W. Bao, P. J. Neiman, P. J. Schultz, H. Yuan, and A. B. White, 2009: Evaluation and comparison of microphysical algorithms in ARW-WRF model simulations of atmospheric river events affecting the California coast. *J. Hydrometeor.*, **10**, 847-870.

Jankov, I., J. Berner, J. Beck, H. Jiang, J. B. Olson, G. Grell, T. G. Smirnova, S. G. Benjamin, and J. M. Brown, 2017: A performance comparison between Multiphysics and stochastic approaches within a North American RAP Ensemble. *Mon. Wea. Rev.*, **145**, 1161-1179.

Jankov, I., J. Beck, J. Wolff, M. Harrold, J. B. Olson, T. Smirnova, C. Alexander, and J. Berner, 2019: Stochastically perturbed parameterizations in an HRRR-Based ensemble. *Mon. Wea. Rev.*, **147**, 153-173.

Jensen, A. A., J. Y. Harrington, and H. Morrison, 2018: Impacts of ice particle shape and density evolution on the distribution of orographic precipitation. *J. Atmos. Sci.*, **75**(9), 3095-3114.

Jiang, W., and R. B. Smith, 2003: Cloud timescales and orographic precipitation. *J. Atmos. Sci.*, **60**, 1543-1559.

Johnson, A., and X. Wang, 2012: Verification and calibration of neighborhood and object-based probabilistic precipitation forecasts from a multi-model convection-allowing ensemble. *Mon. Wea. Rev.*, **140**, 3054-3077.

Johnson, A., and X. Wang, 2013: Object-based evaluation of a storm scale ensemble during the 2009 NOAA Hazardous Weather Testbed Spring Experiment. *Mon. Wea. Rev.*, **141**, 1079-1098.

Kamae, Y., W. Mei, and S.-P. Xie, 2017: Climatological relationship between warm season atmospheric rivers and heavy rainfall over East Asia. *Journal of the Meteorological Society of Japan*, **95**(6), 411-431.

Kim, J., D. E. Waliser, P. J. Neiman, B. Guan, J.-M. Ryoo, and G. A. Wick, 2013: Effects of atmospheric river landfalls on the cold season precipitation in California. *Clim. Dyn.*, **40**, 465-474.

King, D. M., and B. J. C. Perera, 2013: Morris method of sensitivity analysis applied to assess the importance of input variabes on urban water supply yield – A case study. *Journal of Hydrology*, **477**, 17-32.

Kingsmill, D. E., P. J. Neiman, and A. B. White, 2016: Microphysics regime impacts on the relationship between orographic rain and orographic forcing in the coastal mountains of Northern California. *J. Hydrometeorology*, **17**, 2905-2922.

Kirshbaum, D., and R. B. Smith, 2008: Temperature and moist-stability effects on midlatitude orographic precipitation. *Q. J. R. Meteorol. Soc.*, **134**, 1183-1199.

Kunz, M., and C. Kottmeier, 2006: Orographic enhancement of precipitation over low mountain ranges. Part I: Model formulation and idealized simulations. *J. Appl. Meteo. Climatol.*, **45**, 1025-1040.

Kunz., M., and S. Wassermann, 2011: Moist dynamics and orographic precipitation related to ambient conditions. *Meteorol. Z.*, **20**, 199-215.

Lang, T. J., and A. P. Barros, 2004: Winter storms in the central Himalayas. *Journal of the Meteorological Society of Japan*, **82**(3), 829-844.

Lavers, D. A., R. P. Allan, G. Villarini, B. Lloyd-Hughes, D. J. Brayshaw, and A. J. Wade, 2013: Future changes in atmospheric rivers and their implications for winter flooding in Britain. *Environ. Res. Lett.*, **8**, 034010.

Leung L. R, and Y. Qian, 2009. Atmospheric rivers induced heavy precipitation and flooding in the Western U.S. simulated by the WRF regional climate model. *Geophys. Res. Lett.*, **36**, L03820.

Lin, Y.-L., S. Chiao, T.-A. Wang, M. L. Kaplan, and R. P. Weglarz, 2001: Some common ingredients for heavy orographic rainfall. *Weather Forecasting*, **16**, 633- 660.

Lin. Y., and B. A. Colle, 2009: The 4-5 December 2001 IMPROVE-2 Event: Observed microphysics and comparisons with the Weather Research and Forecasting model. *Mon. Wea. Rev.*, **137**, 1372-1392.

Lin, Y., and B. A. Colle, 2011: A new bulk microphysical scheme that includes riming intensity and temperature-dependent ice characteristics. *Mon. Wea. Rev.*, **139**, 1013-1035.

Lin, Y., B. A. Colle, and S. E. Yuter, 2013: Impact of moisture flux and freezing level on simulated orographic precipitation errors over the Pacific Northwest. *J. Hydrometeor*., **14**, 140-152.

Liu, C., K. Ikeda, G. Thompson, R. Rasmussen, and J. Dudhia, 2011: High-resolution simulations of wintertime precipitation in the Colorado headwaters region: Sensitivity to physics parameterizations. *Mon. Wea. Rev.*, **139**, 3533-3553.

Lundquist, J., J. R. Minder, P. J. Neiman, and E. Sukovich, 2010: Relationships between barrier jet heights, orographic precipitation gradients, and streamflow in the northern Sierra Nevada. *J. Hydromet.*, **11**, 1141-1156.

Maddox, R. A., L. R. Hoxit, C. F. Chappell, and F. Caracena, 1978: Comparison of meteorological aspects of the Big Thompson and Rapid City flash floods. *Mon. Wea. Rev.*, **106**, 375-389.

Mansell, E. R., 2010: On sedimentation and advection in multimoment bulk microphysics. *J. Atmos. Sci*., **67**, 3084-3094.

Mansell, E. R., C. L. Ziegler, and E. C. Bruning, 2010: Simulated electrification of a small thunderstorm with two-moment bulk microphysics. *J. Atmos. Sci.*, **67**, 171-194.

Marwitz, J. D., 1987: Deep orographic storms over the Sierra Nevada, Part I: Thermodynamic and kinematic structure. *J. Atmos. Sci.*, **44**, 159-173.

Mattingly, K. S., T. L. Mote, and X. Fettweis, 2018: Atmospheric river impacts on Greenland ice sheet surface mass balance. *J. Geophys. Res. Atm*., **123**, 8538-8560.

Medina, S., B. F. Smull, R. A. Houze Jr., and M. Steiner, 2005: Cross-barrier flow during orographic precipitation events: Results from MAP and IMPROVE. *J. Atmos. Sci*., **62**, 3580-3597.

Meyer-Christoffer, A., A. Becker, P. Finger, U. Schneider, and M. Ziese, 2018: GPCC Climatology Version 2018 at 0.25º: Monthly Land-Surface Precipitation Climatology for Every Month and the Total Year from Rain-Gauges built on GTS-based and Historical Data.

Miglietta, M. M., and R. Rotunno, 2005: Simulations of moist nearly neutral flow over a ridge. *J. Atmos. Sci.*, **62**, 1410-1427.

Miglietta, M. M., and R. Rotunno, 2006: Further results on moist nearly neutral flow over a ridge. *J. Atmos. Sci.*, **63**, 2881-2897.

Minder, J. R., D. R. Durran, G. H. Roe, and A. M. Anders, 2008: The climatology of small-scale orographic precipitation over the Olympic Mountains: Patterns and processes. *Q. J. R. Meteorol. Soc.*, **134**, 817 – 839.

Minder, J. R., D. R. Durran, and G. H. Roe, 2011: Mesoscale controls on the mountainside snow line. *J. Atmos. Sci.*, **68**, 2107-2127.

Morales, A., R. S. Schumacher, S. M. Kreidenweis, 2015: Mesoscale vortex development during extreme precipitation: Colorado, September 2013. *Mon. Wea. Rev.*, **143**, 4943-4962.

Morales, A., H. Morrison, and D. J. Posselt, 2018: Orographic precipitation response to microphysical parameter perturbations for idealized moist nearly neutral flow. *J. Atmos. Sci*., **75**, 1933-1953.

Morales, A., D. J. Posselt, H. Morrison, and F. He, 2019: Assessing the influence of microphysical and environmental parameter perturbations on orographic precipitation. *J. Atmos. Sci.*, **76**(5), 1373-1395.

Morales, A., D. J. Posselt, and H. Morrison, 2019: Multivariate sensitivity analysis of orographic precipitation using a Markov chain Monte Carlo algorithm. *In prep.*

Moran, D., 2018: Do you how upslope affects the weather? Accessed May 12, 2019. [Available online https://blog.weatherops.com/do-you-know-how-upslope-flow-affects-the-weather]

Morris, M. D., 1991: Factorial sampling plans for preliminary computational experiments. *Technometrics*, **33**(2), 161-174.

Morrison, H., J. A. Curry, and V. I. Khvorostyanov, 2005: A new double-moment microphysics parameterization for application in cloud and climate models. Part I: Description. *J. Atmos. Sci.*, **62**, 1665-1677.

Morrison, H., G. Thompson, and V. Tatarskii, 2009: Impact of cloud microphysics on the development of trailing stratiform precipitation in a simulated squall line: Comparison of one- and two-moment schemes. *Mon. Wea. Rev.*, **137**, 991-1007.

Morrison, H., J. A. Milbrandt, G. H. Bryan, K. Ikeda, S. A. Tessendorf, and G. Thompson, 2015: Parameterization of cloud microphysics based on the prediction of bulk ice particle properties. Part II: Case study comparisons with observations and other schemes. *J. Atmos. Sci*., **72**, 312-339.

Morrison, H., and J. A. Milbrandt, 2015: Parameterization of cloud microphysics based on the prediction of bulk ice particle properties. Part I: Scheme description and idealized tests. *J. Atmos. Sci.*, **72**, 287-311.

Morrison, H., A. Morales, C. Villanueva-Birriel, 2015: Concurrent sensitivities of an idealized deep convective storm to parameterization of microphysics, horizontal grid resolution, and environmental static stability. Mon. Wea. Rev., 143, 2082-2104.

Mote, P.W., A.F. Hamlet, M. Clark, and D.P. Lettenmaier, 2005: Declining mountain snowpack in western North America. *Bull. Amer. Meteor. Soc.,* **86**, 39-49.

Mott, R., D. Scipion, M. Schneebeli, N. Dawes, A. Berne, and M. Lehning, 2014: Orographic effects on snow deposition patterns in mountainous terrain. *J. Geophys. Res. Atmos.*, **119**, 1419-1439.

NASA: *Monsoon Mystery.* Earth Observatory. Published May 31, 2007. Accessed May 13, 2019. https://earthobservatory.nasa.gov/features/AmazonLAI/amazon_lai3.php

Neff, W., 2018: Atmospheric rivers melt Greenland. *Nature Climate Change*, **8**, 857-858.

Neiman, P. J., F. M. Ralph, A. B. White, D. E. Kingsmill, and P. O. G. Persson, 2001: The statistical relationship between upslope flow and rainfall in California's coastal mountains: Observations during CALJET. *Mon. Wea. Rev.*, **130**, 1468-1492.

Neiman, P. J., F. M. Ralph, G. A. Wick, J. D. Lundquist, and M. D. Dettinger, 2008: Meteorological characteristics and overland precipitation impacts of atmospheric rivers affecting the west coast of North America based on eight years of SSM/I satellite observations. *J. Hydrology*, **9**, 22-47.

Neiman, P. J., F.M. Ralph, G.A. Wick, Y.-H. Kuo, T.-K. Wee, Z. Ma, G.H. Taylor, and M.D. Dettinger, 2008b: Diagnosis of an intense atmospheric river impacting the Pacific Northwest:

Storm summary and offshore vertical structure observed with COSMIC satellite retrievals. *Mon. Wea. Rev.*, **136**, 4398-4420.

Nieman, P. J., L. J. Schick, F. M. Ralph, M. Hughes, and G. A. Wick, 2011: Flooding in western Washington: The connection to atmospheric rivers. *J. Hydrometeor*., **12**, 1337-1358.

Nieman, P. J., and CoAuthors, 2016: An airborne and ground-based study of a long-lived and intense atmospheric river with mesoscale frontal waves impacting California during CalWater-2014. *Mon. Wea. Rev.*, **144**, 1115-1144.

Pandey, G. R., D. R. Cayan, and K. P. Georgakakos, 1999: Precipitation structure in the Sierra Nevada of California during winter. *J. Geophys. Res.*, **104** (D10), 12,019-12,030.

Pang, W-K, J. J. Forster, and M. D. Troutt, 2001: Estimation of wind speed distribution using Markov chain Monte Carlo Techniques. *Journal of Applied Meteorology*, **40**, 1476-1484.

Porter, K., and CoAuthors, 2011: Overview of the ARkStorm scenario. U.S. Geological Survey Open-File Report 2010-1312, 183 p. and appendixes.

Posselt, D. J., T. S. L'Ecuyer, and G. L. Stephens, 2008: Exploring the Error Characteristics of Thin Ice Cloud Property Retrievals Using a Markov Chain Monte Carlo Algorithm. *J. Geophys. Res.*, **113**, D24206.

Posselt, D. J., and T. Vukicevic, 2010: Robust Characterization of Model Physics Uncertainty for Simulations of Deep Moist Convection. *Mon. Wea. Rev*., **138**, 1513–1535.

Posselt, D. J., and C. H. Bishop, 2012: Nonlinear parameter estimation: Comparison of an Ensemble Kalman Smoother with a Markov chain Monte Carlo algorithm. *Mon. Wea. Rev.*, **140**, 1957-1974.

Posselt, D. J., 2013: Markov chain Monte Carlo Methods: Theory and Applications. *Data Assimilation for Atmospheric, Oceanic and Hydrologic Applications*, 2nd Ed. S. K. Park and L. Xu, Eds., Springer, pp 59–87.

Posselt, D. J., 2016: A Bayesian Examination of Deep Convective Squall Line Sensitivity to Changes in Cloud Microphysical Parameters. *J. Atmos. Sci.*, **73**, 637–665.

Posselt, D. J., J. Kessler, and G. G. Mace, 2017: Bayesian retrievals of vertically resolved cloud particle size distribution properties. *J. Appl. Meteor. Clim*., **56**, 745-765.

Pruppacher, H. R., and J. D. Klett, 2010: *Microphysics of clouds and precipitation.* Springer, 954 pp.

Purdy, J. C., G. L. Austin, A. W. Seed, and I. D. Cluckie, 2005: Radar evidence of orographic enhancement due to the seeder feeder mechanism. *Meteorol. Appl.*, **12**, 199-206.

Purnell, D. J., and D. J. Kirshbaum, 2018: Synoptic control over orographic precipitation distributions during the Olympics Mountains Experiment (OLYMPEX). *Mon. Wea. Rev.*, **146**, 1023-1044.

Qiao, X., S. Wang, and J. Min, 2018: The impact of a stochastically perturbing microphysics scheme on an idealized supercell storm. *Mon. Wea. Rev.*, **146**, 95-118.

Ralph, F. M., P. J. Neiman, and G. A. Wick, 2004: Satellite and CALJET aircraft observations of atmospheric rivers over the eastern North Pacific Ocean during the winter of 1997/98. *Mon. Wea. Rev.*, **132**, 1721-1745.

Ralph, F. M., P. J. Neiman, and R. Rotunno, 2005: Dropsonde Observations in Low-Level Jets over the Northeastern Pacific Ocean from CALJET-1998 and PACJET-2001: Mean Vertical-Profile and Atmospheric-River Characteristics. *Mon. Wea. Rev.*, **133**, 889-910.

Ralph, F. M., P. J. Neiman, G. A. Wick, S. I. Gutman, M. D. Dettinger, D. R. Cayan, and A. B. White, 2006: Flooding on California's Russian River: Role of atmospheric rivers. *Geophys. Res. Lett.*, **33**, L13801.

Ralph, F. M., P. J. Neiman, G. N. Kiladis, K. Weickman, and D. W. Reynolds, 2011: A multi-scale observational case study of a Pacific atmospheric river exhibiting tropical-extratropical connections and a mesoscale frontal wave. *Mon. Wea. Rev.*, **139**, 1169-1189.

Ralph, F. M., and M. D. Dettinger, 2011: Storms, floods, and the science of atmospheric rivers. *EOS, Transactions*, Amer. Geophys. Union, **92**, 265-266.

Ralph, F. M., and M. D. Dettinger, 2012: Historical and national perspectives on extreme West Coast precipitation associated with atmospheric rivers during December 2010. *Bull. Amer. Meteor. Soc.*, **93**, 783-790.

Ralph, F. M., T. Coleman, P. J. Neiman, R. J. Zamora, and M. D. Dettinger, 2013: Observed impacts of duration and seasonality of atmospheric-river landfalls on soil moisture and runoff in coastal northern California. *J. Hydrology*, **14**, 443-459.

Ralph, F. M., and Co-authors, 2016: CalWater field studies designed to quantify the roles of atmospheric rivers and aerosols modulating U.S. West Coast precipitation in a changing climate. *Bull. Amer. Meteor. Soc.*, 1209-1228.

Ralph, F. M., and Co-authors, 2017: Dropsonde observations of total integrated water vapor transport within North Pacific Atmospheric Rivers. *J. Hydrometeorol*., **18**, 2577-2596.

Ralph, F. M., J. J. Rutz, J. M. Cordeira, M. Dettinger, M. Anderson, D. Reynolds, L. J. Schick, and C. Smallcomb, 2019: A scale to characterize the strength and impacts of atmospheric rivers. *Bull. Amer. Meteor. Soc.*, 269-289.

Robichaud, A. J., and G. L. Austin, 1988: On the modelling of warm orographuic rain by the seeder-feeder mechanism. *Q. J. R. Meteorol. Soc*., **114**, 967-988.

Roe, G. H., 2005: Orographic precipitation. *Annu. Rev. Earth Planet. Sci*., **33,** 645-671.

Rogers, R. R., and M. K. Yau, 1989: *A short course in cloud physics.* Pergamon Press, 290 pp.

Rutz, J. J., W. J. Steenburgh, and F. M. Ralph, 2014: Climatological characteristics of atmospheric rivers and their inland penetration over the western United States. *Mon. Wea. Rev*., **142**, 905-921.

Saltelli, A., and Co-authors, 2008: *Global Sensitivity Analysis. The Primer*. John Wiley & Sons Ltd, 305 pp.

Santos, M., P. S. Lucio, and A. C. Gomes, 2016: Stochastic simulation for the precipitation frequency over some Brazilian cities through the Metropolis-Hastings algorithm. *Meteorol. Appl.*, **2**3, 420-424.

Sawyer, J. S., 1956: The physical and dynamical problems of orographic rain. *Weather*, **11**, 375-381.

Schwartz, C. S., and Coauthors, 2010: Toward improved convection-allowed ensembles: Model physics sensitivities and optimizing probabilistic guidance with small ensemble membership. *Wea. Forecasting*, **25**, 263-280.

Shin, M.-J., J. H.A. Guillaume, B. F.W. Croke, and A. J. Jakeman, 2013: Addressing ten questions about conceptual rainfall-runoff models with global sensitivity analyses in R. *Journal of Hydrology*, **503**, 135-152.

Smith, R. B., 1979: The influence of mountains on the atmosphere. *Advances in Geophysics*, Vol. 21, Academic Press, 87-230.

Smith, R. B., 2006: Progress on the theory of orographic precipitation. *GSA Spec. Pap*., **398**, 1-16.

Song, C., J. Zhang, C. Zhan, Y. Xuan, M. Ye, and C. Xu, 2015: Global sensitivity analysis in hydrological modeling: Review of concepts, methods, theoretical framework, and applications. *Journal of Hydrology*, **523**, 739-757.

Stensrud, D. J., 2007: *Parameterization schemes: keys to understanding numerical weather prediction models*. Cambridge University Press, 459 pp.

Stoelinga, M. T., and Coauthors, 2003: Improvement of microphysical parameterization through observational verification experiment. *Bull. Amer. Meteor. Soc.*, **84**, 1807-1826.

Stoelinga, M. T., R. E. Stewart, G. Thompson and J. M. Thériault, 2013: Microphysical processes within winter orographic cloud and precipitation systems. *Mountain Weather Research and Forecasting*. F. Chow, S. De Wekker, and B. Snyder, Ed., Springer, 345-408.

Stohl, A., C. Forster, and H. Sodemann, 2008: Remote sources of water vapor forming precipitation on the Norwegian west coast at 60°N – A tale of hurricanes and atmospheric rivers. *J. Geophys. Res.*, **113**, D05102.

Tessendorf, S. A., and CoAuthors, 2019: A transformational approach to winter orographic weather modification research: The SNOWIE Project. *Bull. Amer. Meteor. Soc.*, **100**, 71-92.

Thompson, G., P. R. Field, R. M. Rasmussen, and W. D. Hall, 2008: explicit forecasts of winter precipitation using an improved bulk microphysics scheme. Part II: Implementation of a new snow parameterization. *Mon. Wea. Rev.*, **136**, 5095-5115.

Thompson, F., and T. Eidhammer, 2014: A study of aerosol impacts on clouds and precipitation development in a large winter cyclone. *J. Atmos. Sci*., **71**, 3636-3658.

Tomassini, L., and P. Reichert, 2007: Robust Bayesian uncertainty analysis of climate system properties using Markov chain Monte Carlo methods. *Journal of Climate*, **20**, 1239-1254.

Tushaus, S. A., D. J. Posselt, M. M. Miglietta, R. Rotunno, and L. Delle Monache, 2015: Bayesian exploration of multivariate orographic precipitation sensitivity for moist stable and neutral flows. *Mon. Wea. Rev.*, **143**, 4459-4475.

van Lier-Walqui, M., T. Vukicevic, and D. J. Posselt, 2012: Quantification of Cloud Microphysical Parameterization Uncertainty using Radar Reflectivity, *Mon. Wea. Rev.*, **140**, 3442-3466.

Viale, M., and M. N. Nuñez, 2011: Climatology of winter orographic precipitation over the subtropical central Andes and associated synoptic and regional characteristics. *J. Hydrometeor.*, **12**, 481-507.

Viale, M., R. Valenzuela, R. D. Garreaud, and F. M. Ralph, 2018: Impacts of atmospheric rivers on precipitation in Southern South America. *J. Hydrometeorology*, **19**, 1671-1687.

Viviroli, D., and R. Weingartner, 2002: The significance of mountains as sources of the world's fresh water. *GAIA*, **11**(3), 182-186.

Viviroli, D., and R. Weingartner, 2004: The hydrological significance of mountains: from regional to global scale. *Hydrology and Earth System Sciences*, **8**(6), 1016-1029.

Viviroli, D., H. H. Dürr, B. Messerli, M. Meybeck, and R. Weingartner, 2007: Mountains of the world, water towers for humanity: Typology, mapping, and global significance. *Water. Resour. Res.*, **43**, W07447.

Viviroli, D., R. Weingartner, and B. Messerli, 2003: Assessing the hydrological significance of the world's mountains. *Mountain Research and Development*, **23**(1), 32-40.

Waliser, D., and B. Guan, 2017: Extreme winds and precipitation during landfall of atmospheric rivers. *Nature Geoscience*, **10**, 179-184.

Wallace, J. M., and P. V. Hobbs, 2006: *Atmospheric science: an introductory survey.* Elsevier Academic Press. 350 pp.

Wang, Z., and N. Huang, 2017: Numerical simulation of the falling snow deposition over complex terrain. *J. Geophys. Res. Atmos.*, **122**, 980-1000.

Wegener, A., 1911: Thermodynamik der Atmosphäre. Barth, Leipzig.

White, A., B. Moore, D. Gottas, and P. J. Neiman, 2019: Winter storm conditions leading to excessive runoff above California's Oroville Dam during January and February 2017. *Bull. Amer. Meteor. Soc.*, 55-69.

Wratt, D. S., M. J. Revell, M. R. Sinclair, W. R. Gray, R. D. Henderson, and A. M. Chater, 2000: Relationships between air mass properties and mesoscale rainfall in New Zealand's Southern Alps. *Atmospheric Research*, **52**, 261-282.

Xue, and Coauthors, 2009: CAPS realtime multi-model convection-allowing ensemble and 1-km convection-resolving forecasts for the NOAA Hazardous Weather Testbed 2009 Spring Experiment. 23rd Conf. on Weather Analysis and Forecasting/19th Conf. on Numerical Weather Prediction, Omaha, NE, Amer. Meteor. Soc., 16A.2.

Yang, J., F. Castelli, and Y. Chen, 2014: Multiobjective sensitivity analysis and optimization of distributed hydrologic model MOBIDIC. *Hydrol. Earth Syst. Sci*., **18**, 4104-4112.

Zagrodnik, J. P., L. McMurdie, and R. A. Houze, Jr., 2018: Stratiform precipitation processes in cyclones passing over a coastal mountain ridge. *J. Atmos. Sci.*, **75**, 983-1004.

Zarzycki, C. M., and P. A. Ullrich, 2017: Assessing sensitivities in algorithmic detection of tropical cyclones in climate data. *Geophys. Res. Lett*., **44**, 1141-1149.

Ziegler, C. L., 1985: Retrieval of thermal and microphysical variables in observed convective storms. Part 1: Model development and preliminary testing. *J. Atmos. Sci*., **42**, 1487-1509.

Zhang, T., L. Li, Y. Lin, W. Xue, F. Xie, H. Xu, and X. Huang, 2015: An automatic and effective parameter optimization method for model tuning. *Geosci. Model Dev.*, **8**, 3579-3591.

Zhou, Y., H. Kim, and B. Guan, 2018: Life cycle of atmospheric rivers: Identification and climatological characteristics. *J. Geophys. Res. Atmos.*, **123**, 12,715-12,725.

Zhu, Y., and R. E. Newell, 1998: A proposed algorithm for moisture fluxes from atmospheric rivers. *Mon. Wea. Rev.*, **126**, 725-735.